11. Optical Properties

At present, optical measurement methods are the most powerful tools for basic and applied research and inspection of the characteristic properties of a variety of materials, especially following the development of lasers and computers. Optical measurement methods are widely used for optical spectroscopy including linear and nonlinear optics and magneto-optics, conventional and unconventional optical microscopy, fiber optics for passive and active devices, optical recording for CD/DVD and MO disks, and various kinds of optical sensing.

In this chapter, as an introduction to the following sections, the concept and fundamentals of optical spectroscopy are described in Sect. 11.1, including optical measurement tools such as light sources, detectors and spectrometers, and standard optical measurement methods such as reflection, absorption, luminescence, scattering, etc. A short summary of laser instruments is also included. In Sect. 11.2 the microspectroscopic methods that have recently become quite useful for nano-science and nano-technology are described, including single-dot/molecule spectroscopy, near-field optical spectroscopy and cathodoluminescence spectroscopy using scanning electron microscopes. In Sect. 11.3 magneto-optics such as Faraday rotation is introduced and the superlattice of semi-magnetic semiconductors is applied for the imaging measurement of magnetic flux patters of superconductors as an example of spintronics. Section 11.4 is devoted to fascinating subjects in laser spectroscopy, such as nonlinear spectroscopy, time-resolved spectroscopy and THz spectroscopy. In Sect. 11.5 fiber optics is summarized, including transmission properties, nonlinear optical properties, fiber gratings, photonic crystal fibers, etc. In Sect. 11.6 optical recording technology for high-density storage is described in detail, including the measurement methods for the characteristic properties of phase-change and magneto-optical materials. Finally, in Sect. 11.7 a variety of optical sensing methods are described, including the measurement of distance, displacement, three-dimensional shape, flow, temperature and, finally, the human body for bioscience and biotechnology.

This chapter begins with a section on basic technology for optical measurements. Sections 11.2–11.4 deal with advanced technology for optical measurements. Finally Sects. 11.5–11.7 discuss practical applications to photonic devices.

Part C | 11

11.1 Fundamentals of Optical Spectroscopy

11.1.1 Light Source

There are many light sources for use in scientific and industrial measurements [11.1–4]. This subsection deals with the features of various light sources. For source selection, various characteristics should be considered, such as wavelength range, radiant flux, directionality, stability in time and space, lifetime, area of emission, and temporal behavior. Spectral output, whether it is a continuum, a line, or a continuum-plus-line source, should also be considered. No light source covers all wavelengths simultaneously from the ultraviolet (UV) to infrared (IR) wavelength region. Although a black-body with extremely high temperature could realize such an ideal light source, the melting point of the materials that form the electrodes must be extremely high,

and it is impossible to construct it. We, therefore, should select an adequate source that covers the required wavelength region from the UV to the IR region. In general, we use a gas discharge lamp for the UV region and a radiation source from a solid for the visible and the IR region. At present, many kinds of light sources covering each wavelength region, as shown in Fig. 11.1, are available. Those can be broadly classified into: 1) thermal radiation sources such as a tungsten filament lamp (W lamp) and an incandescent lamp in the IR region such as a Nernst glower and a glouber, 2) arc lamps such as a high-pressure xenon arc lamp (Xe lamp), a high- or low-pressure mercury lamp, a hydrogen and a deuterium-hydrogen arc lamp (D_2 lamp) based on electrical discharge in gas, 3) a light-emitting diode (LED) or a laser diode (LD) basing on emission from
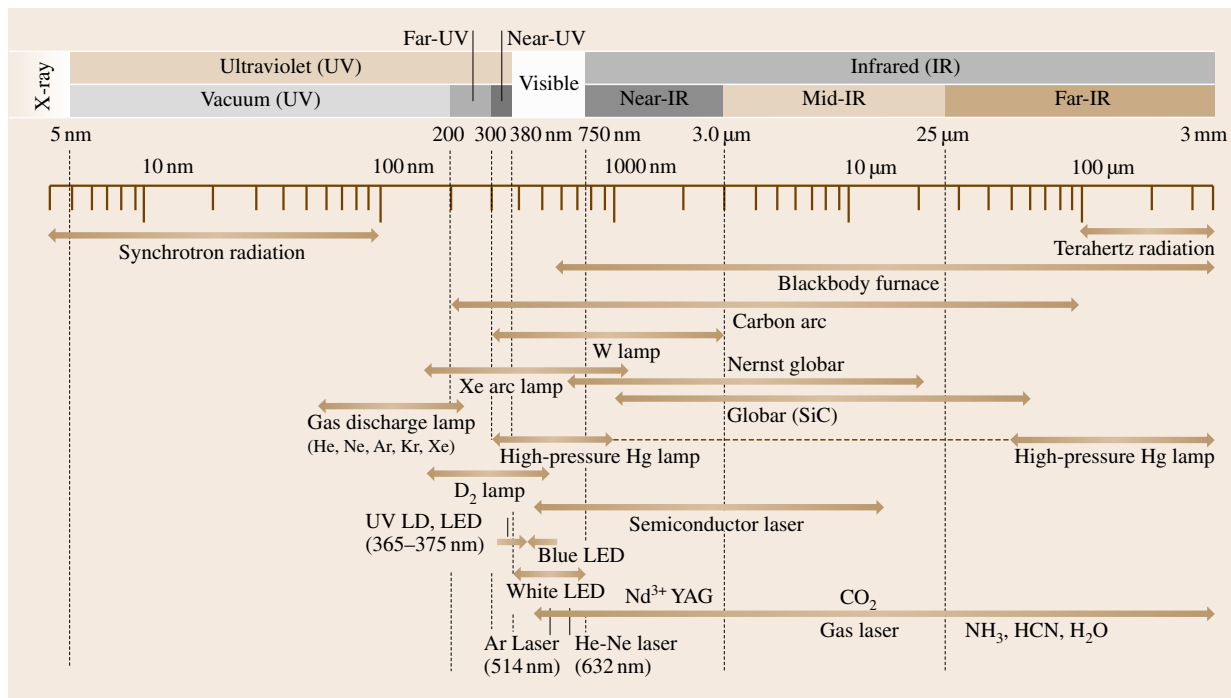

Fig. 11.1 Wavelength regions of various light sources

the pn junctuon of a semiconductor, and 4) narrow-line sources using an atomic or molecular transition lines such as a hollow cathode discharge tube and an electrodeless discharge lamp, including many kinds of lasers. Recently, synchrotron radiation and terahertz emission in the far-UV and submillimeter wavelength regions, respectively, have become available, mainly for research purposes.

Among those light sources, one of the most stable, well-known, and intensively characterized in the visible and the near-IR region is the W lamp (or tungsten-filament white bulb). Although the spectral emissivity of tungsten is about 0.5 in the visible region and about 0.25 in the near-IR region, its spectral distribution of emission agrees relatively well with that of Planck's blackbody radiation. The W lamp can be used in an arbitrary color temperature up to 3100 K. However, more than 90% of the total emission energy is distributed in the IR wavelength region and less than 1% in the UV region below 400 nm. Therefore, it cannot be used in the UV region. The UV region, however, is especially important in the field of spectrochemical analysis. To cover the lower energy in the UV region, the D_2 lamp is used in combination with the W lamp, although the D_2 lamp has some problems in terms of emission stability and ease of operation.

For the tungsten white bulb, a vacuum bulb is used for color temperatures up to 2400 K. A gas bulb sealed in nitrogen, argon, or krypton gas at around 1 atm is used for color temperatures between 2000 and 2900 K. For color temperatures around 3100 K, a tungsten-halogen bulb is used. In order to prevent deposition of tungsten atoms onto the inner surface of the bulb, the pressure of argon or krypton gas is maintained at several atmospheres and the bulb is made mechanically rigid by using quartz. Furthermore, by mixing a small amount of halogen molecules such as I_2, Br_2, or Cl_2 into the gas, the decrease in transmittance due to the deposition of tungsten atoms on the inner surface of the bulb is effectively prevented. This process is known as a halogen cycle. To make the process effective, the bulb temperature must be kept relatively high. The lifetime of the lamp is extended by about two times compared to a lamp that does not benefit from this process.

One of the most significant developments in light sources during the last 15 years is blue or UV LEDs. Blue and UV LDs have even appeared. The blue LED is used mainly for traffic signals and the blue and UV LD as recording or read-out light sources for circular discs and digital videodiscs. However, they also have great potential as light sources for scientific measurement. At present, UV LEDs and UV LDs with an emission wavelength around 365–375 nm are commercially available. Such LEDs and LDs are based on emission from gallium nitride (GaN) materials. GaN is a direct-transition-type semiconductor and has an energy gap of about 3.44 eV at room temperature, which corresponds to the UV emission wavelength. By adding indium (In) and aluminum (Al) to the GaN, one can obtain blue emission. When using gallium phosphorus (GaP) instead of GaN materials, and when adding In and Al, one can obtain green emission. When adding only In, one can obtain red emission. Another light source to be noted is the white LED, which has been commercialized rapidly as a back-illumination light source for liquid crystal displays. The white LED consists of a blue or UV LED and fluorescent materials deposited onto the LED in the same package. The blue or UV LED is used as an excitation light source for the fluorescent materials, which may be yttrium aluminum garnet (YAG) materials or some kinds of rare-earth compounds. The excitation light and fluorescence together make the white light. A high-power white LED exceeding 5 W has been developed. Figure 11.2 shows typical emission spectra of such LEDs and that of the UV LD.

For scientific measurements or for spectrochemical analyses, a pulsed light source in the UV wavelength region is important, for example, for distance measurements, fluorescence lifetime measurements, and so on. For such requirements, a picosecond light pulsar with a pulse duration around 60 ps, a wavelength of 370 nm, and a repetition frequency of 100 MHz has appeared on the market. However, in general, such a laser has a problem in wavelength selection and cost. To solve such problems, a technique to drive the Xe lamp in
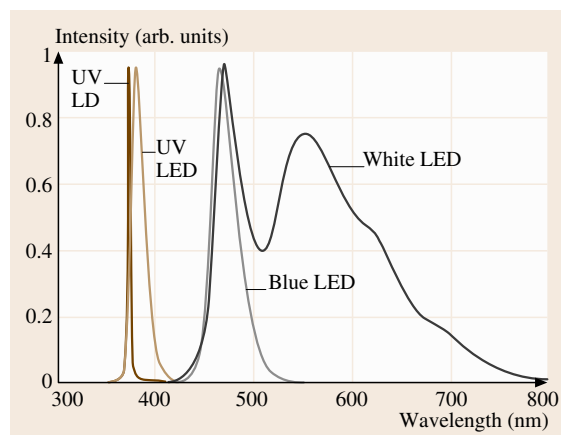
Part C | 11.1

Fig. 11.2 Emission spectra of a blue, UV, and white LED, and that of a UV LD

a nanosecond pulsed mode has been developed [11.5–7]. A technique to modulate the Xe lamp sinusoidally has also been developed so that it can be used in combination with a lock-in light-detection scheme. The UV or the blue LED also can be driven with a large current pulse, resulting in a pulse duration less than 1.5 ns [11.8–10].

11.1.2 Photosensors

This subsection deals with sensing features of various photosensors [11.1–4]. The photosensor is the terminology used for a photodetector when used for a sensing purpose. Photodetectors can be broadly classified into quantum-effect (QE) detectors (or photon detector) and thermal detectors. The QE detector can be subdivided into an external and an internal type, as shown in Table 11.1 Furthermore, the internal type is subdivided into a photoconductive (PC) detector, a photovoltaic (PV) detector, and a photoelectromagnetic (PEM) detector. Figure 11.3 shows the spectral response of each photodetector.

The operating principle of the external QE detector is based on the photoelectron emissive effect of a metal. Representative detectors are a phototube (PT) and a photomultiplier tube (PMT). A variety of photosensitive cathodes, having different spectral responses, are available from the UV to the near-IR wavelength region. A photocathode whose principal component is gallium arsenic (GaAs) gives high quantum efficiency and has sensitivity at longer wavelengths exceeding 1 μm. The PT consists of two electrodes sealed in a vacuum tube: a photocathode and an anode. The PT had been used for light sensing at relatively high powers. At present, it is mainly used for measuring ultra-short light pulses by taking advantage of its simple structure. Such a special PT is known as a biplaner type. The PMT consists of the photocathode, the anode, and 6–12 stages of dynodes aligned between the two electrodes. The role of each dynode is to emit a larger number of secondary electrons than are incident on it. The total amplification factor is typically 10^6, depending on the number of dynodes and the applied voltage. Because of its stability, wide dynamic range, and large specific detectivity D^*, the PMT is widely used for precise light detection. The PMT can be considered as a constant-current source with high impedance. Therefore, the intensity of the output signal is mainly determined by a value of the load resistor. The response time is determined by a time constant calculated from the load resistor and an output capacitance. By cooling the photocathode and adopting a photon counting technique, shot-noise-limited weak-light measurement is possible. Recently, a small type of a metal-packaged PMT has become available [11.11]. By taking advantage of its shorter electron-transit time and smaller time spread of secondary electrons, a new gating technique with a resolution time of less than 0.3 ns has been proposed [11.12].

The operating principle of the PC detector is based on the photoconductive effect of a semiconductor. The electric conductivity of materials, especially semi-

Table 11.1 Classification of photosensors

Type	D^* (cm Hz$^{1/2}$ W^{-1})	Spectral range (nm)	Linear range (decades)	Rise time (ns)
External quantum-effect detector (photon detector)				
Phototube (PT)	$10^8 - 10^{10}$	200–1000	4.5–5.5	0.3–10
Photomultiplier tube (PMT)	$10^{12} - 10^{18}$	200–1000	5.0–6.0	0.3–15
Internal quantum-effect detector				
Photoconductive detector (PC) (PbS, InSb, Ge)	$10^9 - 10^{12}$	750–6000	5.0–6.0	$50 - 10^6$
Photovoltaic detector (PV) (Si photodiode)	$10^8 - 10^{12}$	400–5000	3.0–4.0	$10^3 - 10^6$
Photoelectromagnetic detector (PEM) (InSb)				
	D^* (cm Hz$^{1/2}$ W^{-1})	Spectral range (μm)	Linear range (W)	Time constant (ms)
Thermal detector				
Thermocouple	$10^8 - 10^9$	0.8–40	$10^{-10} - 10^{-8}$	10–30
Thermistor (Bolometer)	$10^8 - 10^9$	0.8–40	$10^{-6} - 10^{-1}$	10–30
Pneumatic detector (Golay cell)	$10^8 - 10^9$	$0.8 - 10^3$	$10^{-6} - 10^{-1}$	2–50
Pyroelectric detector TGS, PZT	$10^7 - 10^8$	$0.3 - 10^3$	$10^{-6} - 10^{-1}$	5–1000

conductors, varies depending on the intensity of the incident light. For UV and visible wavelength regions, intrinsic semiconductors are used. For the IR region, impurity semiconductors are used. The upper limit on wavelength sensitivity for intrinsic semiconductors is determined by the band gap energy (E_g) and that for impurity semiconductors by the ionized potential of the impurities. Generally, CdS ($E_g = 2.4\,\mathrm{eV}$) and CdSe are ($E_g = 1.8\,\mathrm{eV}$) used in the UV and the visible region. For the IR region, PbS, PbSe, PbTe, and $Hg_{1-x}Cd_xTe$ are used, where a cooling procedure is often required to suppress noise.

The operating principle of the PV detector is based on the photovoltaic effect. When a light flux whose energy is larger than the energy gap of the pn junction of a semiconductor is incident, a photoinduced voltage proportional to the incident light intensity is generated. Silicon detectors are popular and can be used from the visible to the near-IR region. The dynamic range for the incident intensity is more than 10^5. To achieve sensitivity in the UV region, detectors with a processed surface or made from GaAsP have been devised; commercially these are known as blue cells. Compared to PC detectors, the PV detector gives a faster response time. Another advantage is that it requires no power supply. The PV detector has two operation modes: the photovoltaic mode and photoconductive mode (or photodiode mode). In the photovoltaic mode, the detector is used with zero bias voltage and the detector is considered as a constant-voltage source with low internal resistance. In the photoconductive mode, the detector is used with a reverse bias voltage and can be considered as a constant-current source with high impedance. The photoconductive mode gives a wide dynamic range and a fast response. When one needs a high-speed subnanosecond response, use of a pin photodiode or an avalanche photodiode (APD) should be considered [11.13, 14].

The PEM detector utilizes contributions of an electron–hole pair to the photovoltage. The electron–hole pair is generated on the surface of an intrinsic semiconductor such as InSb. By applying the external magnetic field to the semiconductor during a diffusion process, the pair is divided in opposition directions, each contributing to the voltage. This type of detector is, however, not commonly used now.

In a thermal detector, optical power absorbed on the surface of the detector is converted to thermal energy and a temperature detector measures the resulting change of temperature. A variety of techniques have been developed to attain high-speed response and high sensitivity, which is a tradeoff. Although, in principle, an ideal thermal detector does not have a wavelength-dependent sensitivity, one cannot realize such an ideal detector. Typical thermal detectors are thermocouples, thermopiles, pneumatic detectors, Golay cells, pyroelectric detectors etc.

A multichannel (MD) detector has been developed that integrates many internal QE detectors onto a silicon substrate. Electric charges produced by the incident light, usually in the UV and visible range, are
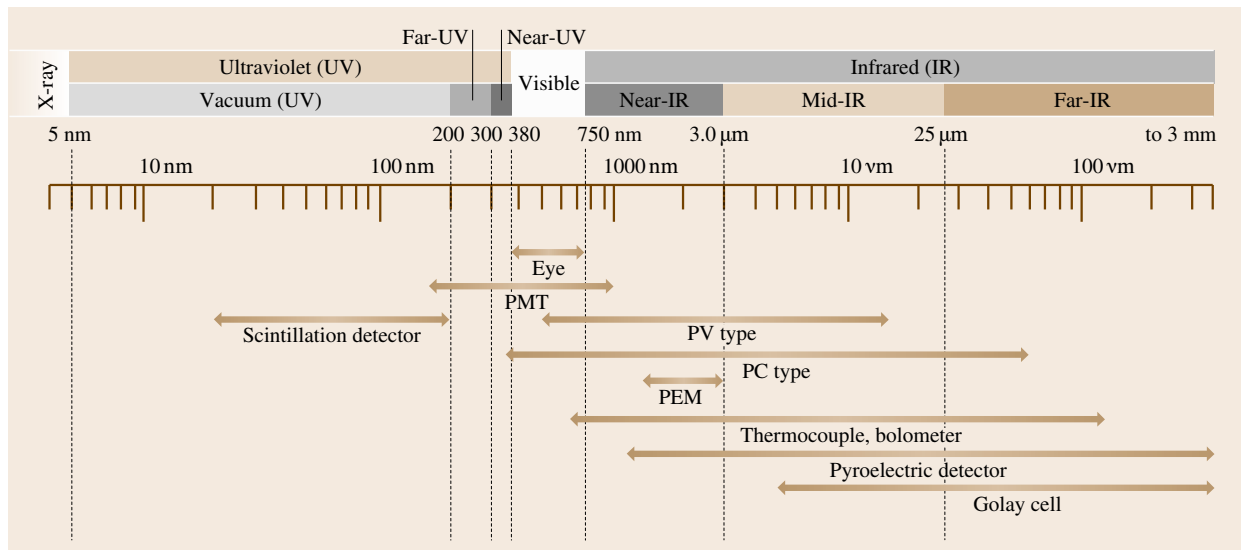

Fig. 11.3 Applicable wavelength regions of various photodetectors

accumulated on individual detectors. A metal–oxide–semiconductor-type (MOS) detector employs electric switches to read out the electric charge. A charge-coupled device (CCD) has a larger integration density than the MOS type because of the simplicity of the process of charge accumulation and transfer. The sensitivity is 10^7–10^8 photons/cm^2 and the dynamic range is 10^3–10^4. Recently, infrared image sensors using HdCdTe have appeared in the market. This MD can be used not only as a spectral photosensor but also as a position sensor.

To select the optical detector, the fundamental issues to be considered are: 1) spectral response, 2) sensitivity, 3) detection limit, and 4) time response. Concerning the spectral response, spectral matching with the light source should be considered. The spectral distribution of the background light also should be taken into account. The sensitivity of the detector is defined by the ratio of the intensity of the output signal to that of the incident light. Generally, overall (or all-spectral) sensitivity is employed. To determine the sensitivity, a standard light source whose spectral distribution is known is used as the incident light: a tungsten lamp of 2856 K for the UV and the visible region and a pseudo-blackbody furnace of 500 K for the IR region. The detection limit is usually represented by the noise-equivalent power (NEP) or

the specific detectivity D^*, where $NEP = PV_n/V_s$ and $D^* = \sqrt{A\Delta f}/NEP$, where P is the radiation flux, V_s is the output signal, V_n is the root mean squared value of output noise, A is area of the detector, and Δf is the noise-equivalent frequency bandwidth. The time response is represented by a step response or a steady-state frequency response. The step response is represented by a rise time or a fall time, which are used especially for detectors with a nonlinear response. For high-speed detectors, the time constant is important; this is calculated by the internal resistance of the detector and the parallel output capacitance. Impedance matching with the following electronics is also important.

11.1.3 Wavelength Selection

In a practical measurement, it is often necessary to select a suitable wavelength from the light source. This section deals with some wavelength-selection techniques [11.1–4]. In order to select the monochromatic or quasi-monochromatic light, we usually use a dispersion element, such as an optical filter, a prism, and a diffraction grating. Generally, the diffraction grating is installed in a monochromator (MON). To gather all spectral information simultaneously, one uses a polychromator (POL) in combination with a multichannnel detector
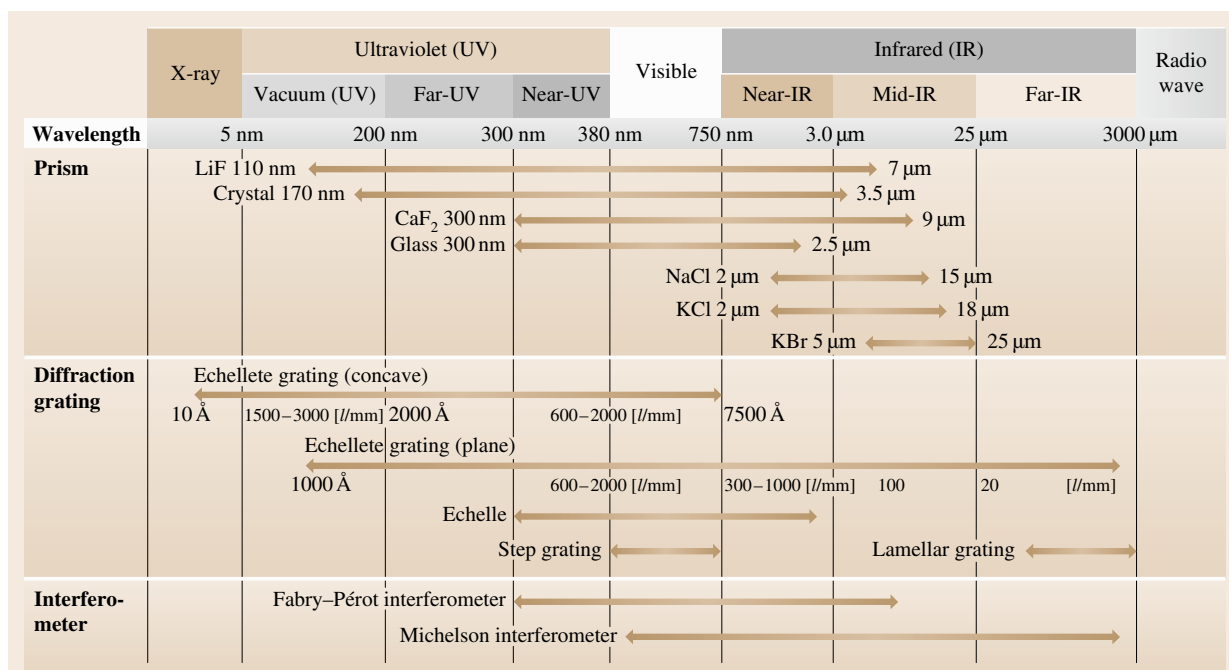

Fig. 11.4 Wavelength regions of various wavelength-selection elements and devices

(MD). In the IR region, a Michelson-type interferometer is sometimes used for a Fourier-transform spectrometer (FTS) [11.15]. For extremely high spectral-resolution measurements, a Fabry–Pérot interferometer should be considered. [11.16] Figure 11.4 shows various elements, devices, systems applicable in each wavelength region.

The prism has been used as the main dispersion element. Dispersion occurs in the prism primarily because of the wavelength dependence of the refractive index of the prism material. Many materials for the prism have been used, for example, glass (350 nm–1 µm), quartz (185 nm–2.7 µm), CaF (125 nm–9 µm), NaCl (200 nm–17 µm), KCl (380 nm–21 µm). When the wavelength is λ (or $\lambda + \Delta\lambda$) and the angle between the incident beam and the deviated monochromatic ray is θ (or $\theta + \Delta\theta$), the angular dispersion, $\Delta\theta/\Delta\lambda$, is given by $\Delta\theta/\Delta\lambda = \Delta\theta/\Delta n \cdot \Delta n/\Delta\lambda = 2\sin(\alpha/2)/\sqrt{1 - n^2\sin^2(\alpha/2)}\,\Delta n/\Delta\lambda$, where n and α are the refractive index and the apex angle of the prism, respectively. In order to increase the spectral resolution, $\lambda/\Delta\lambda$, we should use a prism with a long base L because $\lambda/\Delta\lambda = L \cdot (\Delta n/\Delta\lambda)$.

A plane diffraction grating is made by ruling parallel closely spaced grooves on a thin metal layer deposited on glass. When collimated light flux strikes the grating in a plane perpendicular to the direction of the grooves, different wavelengths are diffracted and constructively interfere at different angles. Although there are two types of gratings, transmission and reflection, the reflection type is invariably used for wavelength selection. If the incident angle is α and the diffraction angle is β, measured from the normal to the grating plane, and the groove interval is d, the following grating formula holds, $d(\sin\alpha + \sin\beta) = m\lambda$, where m is the order of diffraction. In the formula, the order m as well as the diffraction angle β is taken as positive for diffraction on the same side of the grating normal as the incident ray and negative on the opposite side. Then, the angular dispersion is given by $\Delta\beta/\Delta\lambda = m/(d\cos\beta)$ and the resolution power is given by $\lambda/\Delta\lambda = mN$, where N is the total number of grooves. From the formula, we can understand that many wavelengths are observed for a specified diffraction angle β for a given α and d. This phenomenon is known as overlapping orders. From the following two equations, $d(\sin\alpha + \sin\beta) = m\lambda = (m+1)(\lambda - \Delta\lambda)$, we can obtain $\Delta\lambda = \lambda/(m+1)$; the value $\Delta\lambda$ is called the free spectral range. The overlapping orders are usually separated by limiting the source bandwidth with a broadband filter, called the order sorter, or with a predisperser.

Figure 11.5 shows a typical shape of the cross section of the groove. When the angle between the grating plane and the long side of the groove is γ so that $\gamma - \alpha = \beta - \gamma$, the incident and the diffracted light satisfy the relation for specular reflection on the long side of the triangle. Then, we obtain the relation $2d\sin\gamma\cos(\alpha - \gamma) = m\lambda$. When, we put $\alpha = \beta = \gamma$ and $m = 1$, then $2d\sin\gamma = \lambda$. Such a wavelength λ and angle γ are called the blaze wavelength and angle, respectively. The blazed grating is often called an echellete. In this situation, the maximum diffraction efficiency is obtained. For high-resolution spectral measurements, an echelle grating is used, which is a relatively coarse grating with large blaze angles. The steep side of the groove is employed at very high orders.

A concave grating is the same as a plane grating but the grooves are ruled on a concave mirror so that the grooves become a series of equally spaced straight lines when projected onto a plane perpendicular to the straight line connecting the center of the concave shape and a center of its curvature. A circle, whose diameter is equal to the radius of the curvature and which is on a plane perpendicular to the grooves, is called the Rowland circle. Rays starting from a point on the Rowland circle and diffracted by the grating are focused onto a point on the same circle. The two points form an optical conjugate pair with respect to each other. Usually, an entrance and an exit slit are placed on the two points. A problem concerning the concave grating is the presence of relatively large astigmatism. It is, however, used for the UV region because no additional reflection optical element that introduces reflection energy loss is necessary. Recently, various kinds of holographic gratings have been developed to solve the problem of aberration, including astigmatism.
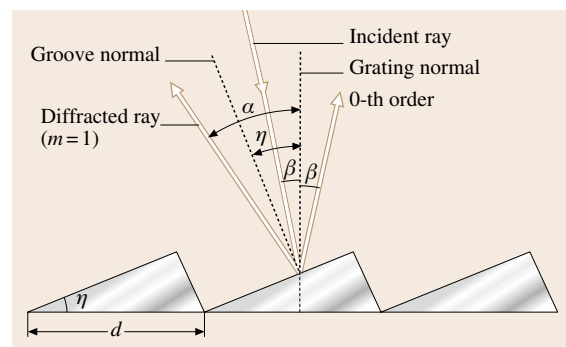
Fig. 11.5 Cross section of a blazed grating. By tilting the groove facet by an angle γ, the zeroth-order ray does not correspond to the specularly reflected ray from the groove surface

When choosing a wavelength-selection method, significant parameters to be considered are the dispersion characteristics, resolution power, solid angle and F-number (or optical throughput factors), degree of stray light, and optical aberration. One of the most convenient and simplest ways is to use a spectroscopic filter such as a color glass filter or an interference filter. However, those lack versatility. The MON is a multipurpose apparatus, which has a grating, an entrance, an exit slit, additional optics, and a wavelength-selection mechanism in one box, by which monochromatic light can be extracted. Many types of mounting and optical arrangement of the optics including the grating, have been proposed.

Although the dispersion-type MON is widely used for the purpose of wavelength selection, it has some drawbacks. In principle, its optical throughput is not large because of the presence of the entrance slit. Furthermore, because of the requirement of the wavelength-scanning mechanism for measuring a continuum spectrum, the total number of wavelength elements limits the signal-gathering time allocatable to a unit wavelength element, resulting in lowering signal-to-noise (SNR) ratio. On the contrary, the FTS has optical throughput and multiplex advantages over the dispersion-type MON. This is because the FTS requires no entrance slit and the entire spectrum is measured simultaneously in the form of an interferogram. However, the multiplex advantage is given only when the detector noise is dominant, such as for an IR detector. Nevertheless, it is sometimes used in the visible region. This is because of the presence of the optical throughput advantage, high precision in wavenumber, and the possibility of realizing extremely high spectral resolution. However, even for the dispersion-type MON, when used in a form of a POL together with the MD, the multichannel advantage is generated. Table 11.2 summarizes the SNR of the FTS, (SNR)$_{\text{FTS}}$, and that of the POL with an MD, (SNR)$_{\text{POL}}$, over that of the dispersion MON with a single detector, (SNR)$_{\text{MON}}$, for cases of when the detector noise, the shot noise, and the scintillation noise is dominant. In the table, n is the total number of spectral elements.

11.1.4 Reflection and Absorption

Reflection or absorption spectra provide rich information on the energy levels of the material, such as inner or valence electrons, vibrations or rotations of molecules or defects in condensed matters, a variety of energy gaps and elementary excitations, e.g. phonons and excitons.

Reflection and Transmission

When a light beam incident on a material surface passes through the material, some of the light is reflected at the surface, while the rest propagates through the material. During the propagation the light is attenuated due to absorption or scattering. The coefficients of *reflectivity R* and *transmittance T* are defined as the ratio of the reflected to the incident power and the transmitted to the incident power, respectively. If there is no absorption or scattering, $R + T = 1$. A schematic diagram for measuring R or T is shown in Fig. 11.6. A tunable light source, a combination of a white light (Sect. 11.1.1) and a monochromator (Sect. 11.1.3) or a tunable laser (Sect. 11.1.5), is used here. Details of detectors are reviewed in Sect. 11.1.2. Changing the wavelength λ of the tunable light source, one can obtain a reflectivity spectrum $R(\lambda)$ or a transmittance spectrum $T(\lambda)$. For convenience the white light directly irradiates the sample and the reflected or transmitted light is detected with a combination of a spectrometer and an array detector, e.g. CCD, if the luminescence from the sample caused by the white light is negligible.

If the beam propagates in the x direction, the intensity $I(x)$ at position x satisfies the following relation

$$\Delta I(x) = I(x + \mathrm{d}x) - I(x) = -\alpha I(x)\,\mathrm{d}x \ ,$$
$$\therefore \frac{\mathrm{d}I(x)}{\mathrm{d}x} = -\alpha I \ .$$

Table 11.2 Comparisons of the SNR of the FTS, (SNR)$_{\text{FTS}}$, and that of the POL with a MD, (SNR)$_{\text{POL}}$, over that of the MON with a SD, (SNR)$_{\text{MON}}$, for cases when the detector noise, the shot noise, and the scintillation noise are dominant, where n is the total number of spectral elements

Noise	Detector noise	Shot noise	Scintillation noise
SNR			
$\dfrac{(\text{SNR})_{\text{FTS}}}{(\text{SNR})_{\text{MON}}}$	$\dfrac{\sqrt{n}}{2}$	$\dfrac{1}{\sqrt{2}}$	$\dfrac{1}{n}$
$\dfrac{(\text{SNR})_{\text{POL}}}{(\text{SNR})_{\text{MON}}}$	$\sqrt{n}$	$\sqrt{n}$	1
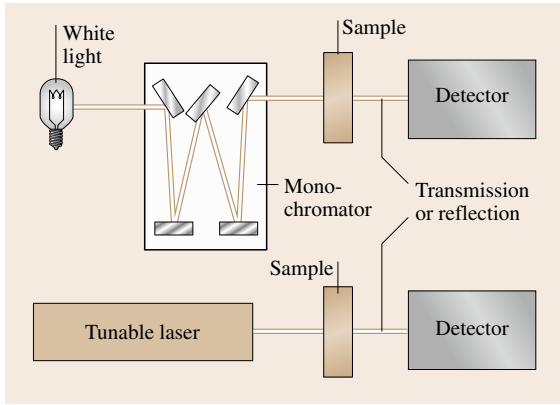
Fig. 11.6 Schematic diagram of reflection or transmission measurement

Here α is called the *absorption coefficient*. The integrated form is

$$I(x) = I_0 \exp(-\alpha x) , \tag{11.1}$$

where I_0 is the intensity of the incident light. The position at $x = 0$ corresponds to the surface of the material. This relation is called *Beer's law*. If the scattering is negligible, the transmittance T is described by

$$T = (1 - R_1) \exp(-\alpha l)(1 - R_2) , \tag{11.2}$$

where R_1 and R_2 are the reflectivities of the front and back surfaces, respectively, and l is the sample thickness.

Optical Constants

If the light propagates in the x direction, the electric field is described by

$$E(x, t) = E_0 \exp\left[i\left(kx - \omega t\right)\right] , \tag{11.3}$$

where k is the wavevector of the light and ω is an angular frequency. In a transparent material with refractive index n, k and the wavelength in vacuo λ are related each other through

$$k = \frac{2\pi}{\lambda/n} = \frac{n\omega}{c} . \tag{11.4}$$

This formula can be generalized to the case of an absorbing material by introducing the *complex refractive index* [11.17]

$$\tilde{n} = n + i\kappa , \tag{11.5}$$

$$k = \frac{\tilde{n}\omega}{c} , \tag{11.6}$$

where κ is called the *extinction coefficient*. The imaginary part of $\tilde{n}$ leads to an exponential decay of the electric field; the absorption coefficient can be described by

$$\alpha = \frac{2\kappa\omega}{c} = \frac{4\pi\kappa}{\lambda} . \tag{11.7}$$

The *amplitude reflectivity* r, the ratio of the electric field of the incident light to that of the reflected light, in the case of normal incidence is described by [11.18]

$$r = \frac{\tilde{n} - 1}{\tilde{n} + 1} . \tag{11.8}$$

If we define the real and imaginary part of r by

$$r \equiv R \exp(i\theta) , \tag{11.9}$$

then the (intensity) reflectivity can be described by

$$R = \left|\frac{\tilde{n} - 1}{\tilde{n} + 1}\right|^2 = \frac{(n - 1)^2 + \kappa^2}{(n + 1)^2 + \kappa^2} , \tag{11.10}$$

and conversely, n and k are written as

$$n = \frac{1 - R}{1 + R - 2\sqrt{R}\cos\theta} , \tag{11.11}$$

$$\kappa = \frac{2\sqrt{R}\sin\theta}{1 + R - 2\sqrt{R}\cos\theta} . \tag{11.12}$$

Ellipsometry enables us to obtain the amplitude reflectivity [11.19]. Thus one can obtain the complex refractive index by measuring the reflectivity.

The optical response of the material, e.g. light propagation described in the complex refractive index, originates from the polarization induced by the incident light. If the electric field E of the light is weak and within linear regime (cf. Sect. 11.4), the polarization P is given by

$$P = \varepsilon_0 \chi E , \tag{11.13}$$

where ε_0 and χ are the vacuum dielectric constant and the *electric susceptibility*, respectively. The electric displacement is

$$D = \varepsilon_0 E + P ,$$
$$\equiv \varepsilon_0 \varepsilon E . \tag{11.14}$$

where ε is the *complex dielectric constant*;

$$\varepsilon = \varepsilon_0(1 + \chi) , \tag{11.15}$$

$$= \varepsilon_1 + i\varepsilon_2 , \tag{11.16}$$

where ε_1 and ε_2 are the real and imaginary parts of ε. From the Maxwell equation [11.1],

$$\frac{\varepsilon}{\varepsilon_0} = \tilde{n}^2 ,$$

$$\frac{\varepsilon_1}{\varepsilon_0} = n^2 - \kappa^2 , \tag{11.17}$$

$$\frac{\varepsilon_2}{\varepsilon_0} = 2n\kappa , \tag{11.18}$$

and conversely,

$$n = \sqrt{\frac{\varepsilon_1 + \sqrt{\varepsilon_1^2 + \varepsilon_2^2}}{2}} \,, \tag{11.19}$$

$$\kappa = \sqrt{\frac{-\varepsilon_1 + \sqrt{\varepsilon_1^2 + \varepsilon_2^2}}{2}} \,. \tag{11.20}$$

Kramers–Kronig Relations

The Kramers–Kronig relations allow us to find the real (imaginary) part of the response function of a linear passive system, if one knows the imaginary (real) part at all frequencies. The relations are derived from the principle of causality [11.17]. In the case of the complex refractive index, the relations are written as

$$n(\omega) = 1 + \frac{2}{\pi} P \int_0^\infty \frac{\omega' \kappa(\omega')}{\omega'^2 - \omega^2} \, d\omega' \,, \tag{11.21}$$

$$\kappa(\omega) = -\frac{2}{\pi\omega} P \int_0^\infty \frac{\omega'^2 [n(\omega') - 1]}{\omega'^2 - \omega^2} \, d\omega' \,, \tag{11.22}$$

where P indicates the Cauchy principal value of the integral. Using these relations one can calculate n from κ, and vice versa. The θ in (11.9) is calculated from the reflectivity R using the following formula

$$\theta(\omega) = -\frac{\omega}{\pi} P \int_0^\infty \frac{\ln\left[\frac{R(\omega')}{R(\omega)}\right]}{\omega'^2 - \omega^2} \, d\omega' \,, \tag{11.23}$$

thus n and κ are determined using (11.11, 11.12) from the reflectivity spectrum. This analysis is very useful for materials with strong absorption in which only the reflectivity is measurable. The Kramers–Kronig analysis of reflection spectra with synchrotron radiation, which covers extremely wide wavelength regions from the far-IR to x-rays, reveals the electronic structures of a huge number of materials [11.20].

The Lorentz Oscillator Model
(Optical Response of Insulators)

The responses of bound (valence) electrons in insulators can be written by the equation of motion of a damped harmonic oscillator

$$m\frac{d^2x}{dt^2} = -m\gamma\frac{dx}{dt} - m\omega_0^2 x$$
$$- eE_0 \exp(-i\omega t) \,, \tag{11.24}$$

where m and e are the mass and charge of the electron, γ is the damping constant, ω_0 is the resonant frequency,

E_0 is the amplitude of the electric field of the light. If we assume $x(t) = x_0 \exp(-i\omega t)$,

$$x_0 = \frac{-eE_0}{m(\omega_0^2 - \omega^2 - i\gamma\omega)} \,. \tag{11.25}$$

Thus the *polarization* is given by

$$P_{\text{resonant}} = \frac{ne^2}{m(\omega_0^2 - \omega^2 - i\gamma\omega)} \,, \tag{11.26}$$

where n is the number of electrons per unit volume. Now we can write the electric displacement

$$D = \varepsilon_0 E + P_{\text{background}} + P_{\text{resonant}} \,,$$
$$= \varepsilon_0 E + \varepsilon_0 \chi_{\text{background}} E + P_{\text{resonant}} \,,$$

where the electric susceptibility $\chi_{\text{background}}$ accounts for all other contributions to the polarization. Using (11.15, 16), we obtain the following equations

$$\varepsilon(\omega) = 1 + \chi + \frac{ne^2}{\varepsilon_0 m(\omega_0^2 - \omega^2 - i\gamma\omega)} \,, \tag{11.27}$$

$$\varepsilon_1(\omega) = 1 + \chi + \frac{ne^2(\omega_0^2 - \omega^2)}{\varepsilon_0 m\left[(\omega_0^2 - \omega^2)^2 + (\gamma\omega)^2\right]} \,, \tag{11.28}$$

$$\varepsilon_2(\omega) = n\frac{e^2\gamma\omega}{\varepsilon_0 m\left[(\omega_0^2 - \omega^2)^2 + (\gamma\omega)^2\right]} \,. \tag{11.29}$$

The dielectric constants in the low and high frequency limit are defined as

$$\varepsilon(0) \equiv \varepsilon_{\text{ST}} \,, \quad \varepsilon(\infty) \equiv \varepsilon_\infty \,.$$

Figure 11.7 shows the frequency dependence of the optical constants introduced in this section.

Typical Absorption Spectrum of Insulators

A schematic plot of a typical absorption spectrum of insulators is shown in Fig. 11.8. There are sharp absorption lines due to *phonons* in the far-infrared region and due to *excitons* in the visible or ultraviolet region; a phonon is a quantized lattice vibration and an exciton is a bound state of an electron and hole like a hydrogen atom. The shape of the absorption or reflection spectra of phonons or excitons can be analyzed by using the Lorentz oscillator model. If the coupling between the photon and the phonon (exciton) is strong, we have to introduce a coupled mode of a photon and a phonon (exciton), *phonon–polariton (exciton–polariton)* [11.21]. Phonon sidebands usually accompany the exciton absorption lines and provide information on the phonons and excitons [11.22].

Above the exciton lines, strong interband absorption is observed. The absorption edge is caused by the onset of the interband transition, in which free electrons and free holes are created simultaneously across the band gap of the insulator. We can obtain a variety of information on the band structure of the material from the interband absorption spectra. Between the phonon and exciton lines there are two weak bands: the multiphonon absorption band due to the combination of several phonons lies around the mid-infrared region and the Urbach tail appears as the onset of optical absorption in the near-infrared or visible region at finite temperature. The shape of the Urbach tail is expressed as [11.21]

$$\alpha(\omega) \propto \exp\left[-\sigma\frac{\hbar(\omega_0 - \omega)}{k_B T}\right], \quad (\omega < \omega_0), \quad (11.30)$$

where σ is an empirical steepness parameter. The σ indicates the strength of the exciton–phonon coupling, because the Urbach tail is caused by phonon-assisted processes. Generally, there is a minimum in the absorption coefficient between the multiphonon region and the Urbach tail. In the case of SiO_2 glasses this minimum lies in the near-infrared region around 1 eV. Thus optical fibers operate between $1.2-1.6\,\mu m$ (Sect. 11.1.5).

Drude Model (Optical Response in Metals)

The responses of free electrons in metals can be written by the equation of motion (11.24) without a restoring force

$$m\frac{d^2x}{dt^2} = -m\gamma\frac{dx}{dt} - eE_0\exp(-i\omega t). \quad (11.31)$$
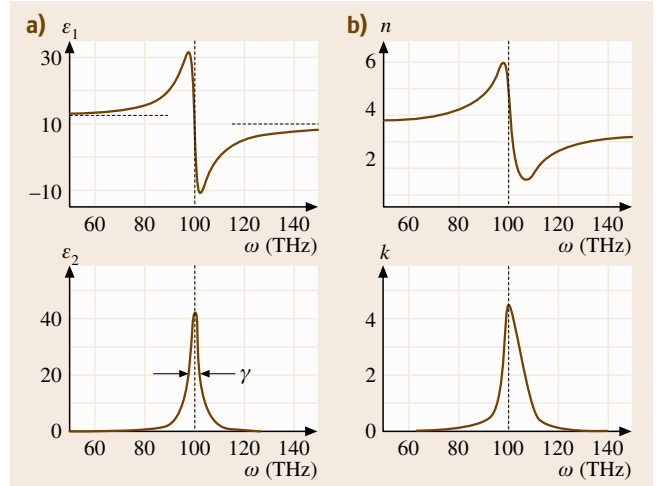
If we assume $x(t) = x_0 \exp(i\omega t)$,

$$x_0 = \frac{eE_0}{m(\omega^2 + i\gamma\omega)}. \quad (11.32)$$

Thus the polarization is given by

$$P = -nex,$$
$$= \frac{-ne^2E}{m(\omega^2 + i\gamma\omega)}. \quad (11.33)$$
$$D = \varepsilon_0 E + P$$
$$\equiv \varepsilon_0 \varepsilon E,$$
$$\therefore \varepsilon = 1 - \frac{ne^2}{\varepsilon_0 m\left(\omega^2 + i\omega/\tau\right)}$$
$$= 1 - \frac{\omega_p^2}{\varepsilon_0 m\left(\omega^2 + i\omega/\tau\right)}. \quad (11.34)$$
$$\tau \equiv \frac{1}{\gamma},$$
$$\omega_p = \left(\frac{ne^2}{\varepsilon_0 m}\right)^{1/2}, \quad (11.35)$$

Fig. 11.7 (a) Frequency dependence of the real and imaginary parts of the dielectric constant, and **(b)** frequency dependence of the complex refractive index, calculated in the case of $\omega_0 = 100\,THz$, $\gamma = 5\,THz$, $\varepsilon_{ST} = 12$ and $\varepsilon_\infty = 10$ using (11.28, 29)

where τ is the relaxation time and ω_p is called the *plasma frequency*. Figure 11.9 shows the reflectivity R in the case of $\gamma = 0$ using (11.10). Perfect reflection occurs for $\omega \leq \omega_p$, and then R decreases for $\omega > \omega_p$, approaching zero.

Electric conductivity can be generalized to the optical frequency region. The current density j is related to the velocity of free electrons and the electric field through

$$j \equiv -Ne\frac{dx}{dt} = \sigma E, \quad (11.36)$$
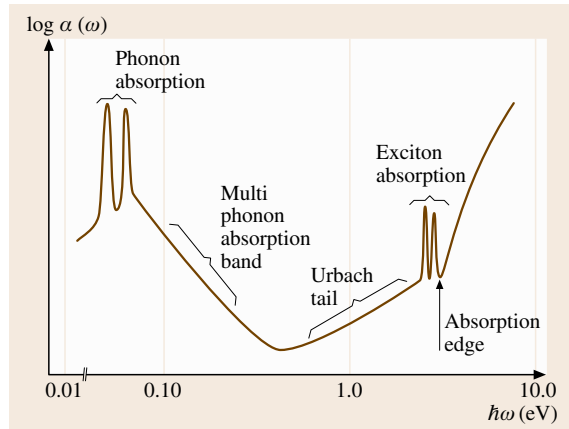
Fig. 11.8 Schematic illustration of the absorption spectrum of insulators

where σ is called the *optical conductivity*. From (11.23) and (11.27),

$$\sigma(\omega) = \frac{\sigma_0}{1 - i\omega\tau} ,\tag{11.37}$$

where

$$\sigma_0 \equiv \frac{ne^2\tau}{m} .\tag{11.38}$$

σ_0 corresponds to the DC conductivity. Thus the DC conductivity can be estimated by purely optical measurements without electrical contacts. Optical conductivity is written in terms of the dielectric function as follows

$$\sigma(\omega) = -i\varepsilon_0\omega\left[\varepsilon(\omega) - 1\right] .\tag{11.39}$$

The Kramers–Kronig relations of the optical conductivity are as follows

$$\sigma_1(\omega) = \frac{2}{\pi} P \int_0^\infty \frac{\omega'\sigma_2(\omega')}{\omega'^2 - \omega^2} \,d\omega' ,\tag{11.40}$$

$$\sigma_2(\omega) = \frac{-2\omega}{\pi} P \int_0^\infty \frac{\sigma_1(\omega')}{\omega'^2 - \omega^2} \,d\omega' ,\tag{11.41}$$

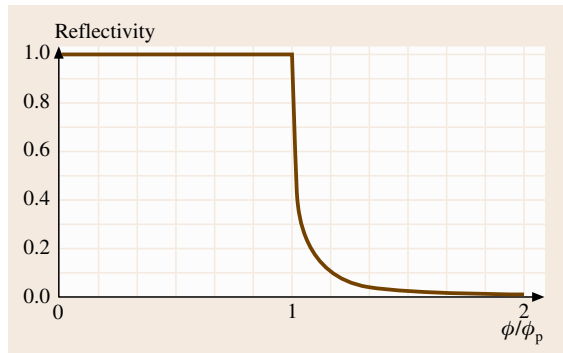where $\sigma_1(\sigma_2)$ is the real (imaginary) part of the σ.

Optical Conductivity of Superconductors

Superfluid electrons in superconductors can move without dissipation, therefore one can take the limit $\tau^{-1} \to 0$ in (11.37),

$$\sigma(\omega) \to -\frac{n_S e^2}{i\omega m} ,$$

where n_S corresponds to the superfluid electron density. Accordingly, the real part σ_1 for the superfluid electrons is zero unless $\omega = 0$. Using (11.40), σ_1 is expressed by a delta function,

$$\sigma_1(\omega) = \frac{\pi n_S e^2}{m} \delta(\omega) .\tag{11.42}$$

Finally, the optical conductivity of superfluid electrons is given by

$$\sigma(\omega) = \frac{\pi n_S e^2}{m}\delta(\omega) - \frac{n_S e^2}{i\omega m} .\tag{11.43}$$

Superconductivity originates from the formation of Cooper pairs. In the higher-frequency region above the binding energy of the Cooper pair, σ_1 should be finite. A schematic illustration of optical conductivity spectrum in superconductors is depicted in Fig. 11.10. Here Δ is called the Bardeen–Cooper–Schrieffer (BCS) gap parameter and 2Δ corresponds to the energy gap in the superconductor [11.17]. Thus we can measure the superconducting gap by optical spectroscopy in the infrared region.

11.1.5 Luminescence and Lasers

Materials emit light by *spontaneous emission* when electrons in the excited states drop to a lower level. The emitted light is called *luminescence*. Such materials with excited electrons can amplify the incident light via *stimulated emission*, which is utilized in *lasers*, an acronym for light amplification by stimulated emission of radiation.

Emission and Absorption of Light

The processes of spontaneous emission, stimulated emission and absorption are illustrated in Fig. 11.11 in the case of a two-level system.

The rate equations are as follows

$$\frac{dN_2}{dt} = -A_{21}N_2 ,\tag{11.44}$$

$$\frac{dN_2}{dt} = -B_{21}N_2\rho(v) ,\tag{11.45}$$

$$\frac{dN_1}{dt} = -B_{12}N_1\rho(v) ,\tag{11.46}$$

Fig. 11.9 The reflectivity of free electrons in the case of $\gamma = 0$
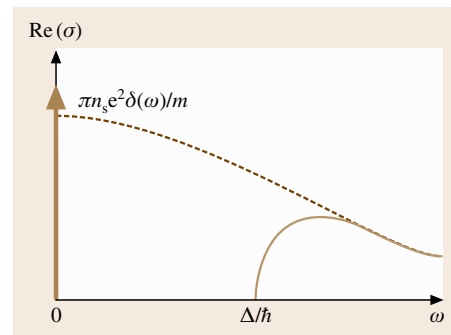
Fig. 11.10 Optical conductivity of a normal metal (*dashed line*) and a superconductor (*solid line*)

where N_1 and N_2 are the populations of a ground state $|1\rangle$ and an excited state $|2\rangle$, respectively, $\rho(\nu)$ is an energy density of the incident light, and A_{21}, B_{21} and B_{12} are Einstein coefficients. The right-hand side of (11.44) shows spontaneous emission (Fig. 11.11a) of a photon with the energy $h\nu = E_2 - E_1$. A radiative lifetime τ_R of the excited state is defined by

$$\tau_R = \frac{1}{A_{21}} . \qquad (11.47)$$

The right-hand side of (11.45) shows stimulated emission (Fig. 11.11b) from $|2\rangle$ to $|1\rangle$. The rate is proportional to the energy density at the resonant frequency ν. Equation (11.46) represents absorption (Fig. 11.11c) from $|1\rangle$ to $|2\rangle$. As seen in the derivation of Beer's law, (11.1), the rate of absorption is proportional to the energy density of the incident light. Combining (11.44–11.46), we obtain the rate equation

$$\frac{dN_2}{dt} = -A_{21}N_2 - B_{21}N_2\rho(\nu) + B_{12}N_1\rho(\nu) . \qquad (11.48)$$

In the steady state, $N_1/dt = N_2/dt = 0$, then

$$A_{21}N_2 + B_{21}N_2\rho(\nu) = B_{12}N_1\rho(\nu) . \qquad (11.49)$$

In thermal equilibrium, the Planck distribution for cavity radiation is

$$\rho(\nu) = \frac{8\pi h\nu^3}{c^3} \frac{1}{\exp\left(\frac{h\nu}{k_B T}\right) - 1} , \qquad (11.50)$$

and the Boltzmann distribution between two levels is

$$\frac{N_2}{N_1} = \exp\left(-\frac{E_2 - E_1}{k_B T}\right) = \exp\left(-\frac{h\nu}{k_B T}\right) . \qquad (11.51)$$

From (11.49–11.51) we obtain the *Einstein relations*

$$\frac{A_{21}}{B_{21}} = \frac{8\pi h\nu^3}{c^3} , \qquad (11.52)$$

$$B_{21} = B_{12} . \qquad (11.53)$$

Luminescence

Luminescence is categorized as follows

1. Photoluminescence (PL)
   The reemission of light after absorbing an excitation light. Details are described in this section.
2. Electroluminescence (EL)
   The emission of light caused by an electric current flowing through the material. This is utilized in op-
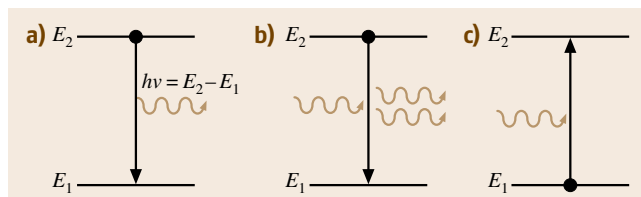
Fig. 11.11a–c Transition processes in a two-level system: (**a**) spontaneous emission, (**b**) stimulated emission, and (**c**) absorption

toelectronic devices: the light emitting diode (LED) and the laser diode (LD).
3. Cathodoluminescence (CL) The emission of light due to irradiation by an electron beam. Details are explained in Sect. 11.2.
4. Chemiluminescence
   The emission of light caused by a chemical reaction. Bioluminescence which originates in an organism belongs to chemiluminescence.

The process involved in luminescence does not simply correspond to the reverse process of absorption in condensed matter. Nonradiative processes, e.g. a phonon-emission process, compete with the radiative process. Hence the decay rate of an excited state $1/\tau$ is described by

$$\frac{1}{\tau} = \frac{1}{\tau_R} + \frac{1}{\tau_{NR}} , \qquad (11.54)$$

where the two terms on the right-hand side represent the radiative and nonradiative decay rates, respectively. The luminescence efficiency or quantum efficiency η is defined by

$$\eta = \frac{1/\tau_R}{1/\tau_R + 1/\tau_{NR}} . \qquad (11.55)$$

If the radiative lifetime τ_R is faster than the nonradiative lifetime τ_{NR}, luminescence is a main de-excitation process and luminescence spectroscopy is a powerful method for the investigation of the excited state. Time-resolved measurements introduced in Sect. 11.4.3 provide direct information on $1/\tau_R$. In many cases, nonradiative decay processes give rise to heating of the material. Therefore, photocalorimetric or photoacoustic spectroscopy is utilized to obtain the information on the nonradiative decay processes [11.23].

PL Spectroscopy

The experimental set-up for the PL measurement is shown in Fig. 11.12. The sample is excited with a laser or a lamp. The PL spectrum is obtained by using array detectors, e.g. a CCD, or by scanning the wavelength

of the spectrometer with a PMT. The sample is usually mounted in a cryostat to cool it to liquid nitrogen or helium temperatures, because the nonradiative process is activated at higher temperature. Conversely, the temperature dependence of PL gives information on the nonradiative decay mechanism. The spectra obtained should be corrected to take into account the sensitivity of the detection system (the spectrometer and the CCD or PMT), while this correction is not required in the case of reflection and absorption measurements, in which the response function of the detection system is canceled in the calculation of I/I_0 (see (11.1)). Reabsorption effects should also be taken into account [11.22] if the frequency region of the luminescence overlaps that of the absorption. Time-resolved PL spectroscopy provides the radiative decay time and direct information on the relaxation process in the excited states. The experimental set-up will be reviewed in Sect. 11.4.3.

PL excitation spectroscopy (PLE) in which the detection wavelength is fixed and the excitation wavelength is scanned allows the absorption spectrum to be measured in the case that direct transmission measurements are impossible because of very weak absorption or an opaque surface of the material. PLE spectroscopy is similar to ordinary absorption measurements but is subject to the condition that there exists a relaxation channel from the (higher) excited state to the emission state being monitored. *Fluorescence line narrowing* (FLN) or *luminescence line narrowing* is a high-resolution spectroscopic technique that uses laser excitation to selected specific subpopulations optically from the inhomogeneously broadened absorption band of the sample, as
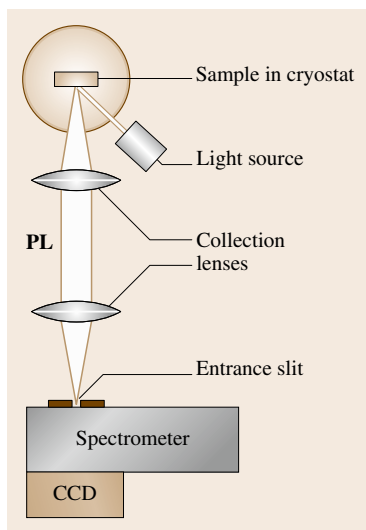
Fig. 11.12 Experimental setup for PL measurement

shown in Fig. 11.23a,b [11.24]. One can obtain the homogeneous width using FLN spectroscopy (Sect. 11.2).

Optical Gain

Laser action arises from stimulated emission, while spontaneous emission prevents lasing. Using (11.44, 11.45, 11.52) the ratio between the rates of stimulated emission and spontaneous emission is calculated as

$$\frac{N_2 B_{21}\rho(\nu)}{N_2 A_{21}} = \frac{1}{\exp\left(\frac{h\nu}{k_B T}\right) - 1} . \qquad (11.56)$$

This ratio is less than unity if T is positive. Hence a *negative temperature* is required for the lasing. From (11.51) this negative temperature corresponds to $N_2 > N_1$, which is called *population inversion*.

If population inversion is realized, the incident light, called *seed light*, is amplified by stimulated emission. In the case that the seed light originates from the luminescence of the material itself, *amplified spontaneous emission* (ASE) appears, as shown in Figure 11.13.

Optical gain is calculated using (11.45,11.46) as an extension of Beer's law (11.1)

$$\frac{dI(x)}{dx} = (B_{21}N_2 - B_{12}N_1)\frac{g(\nu)h\nu I(x)}{c} , \qquad (11.57)$$

where $g(\nu)$ is a spectral function which describes the frequency spectrum of the spontaneous emission. Then, using the Einstein relation (11.52), we obtain

$$I(x) = I_0 \exp[G(\nu)x] , \qquad (11.58)$$

$$G(\nu) = \frac{(N_2 - N_1)A_{21}c^2 g(\nu)}{8\pi\nu^2} , \qquad (11.59)$$

where I_0 and I are the input and output light intensities, respectively. $G(\nu)$ is called the *gain coefficient*.

The population inversion can be obtained in the following ways

1. Optical pumping
   This method is used in solid-state lasers (except LDs) and dye lasers.
2. Electric discharge
   Gas lasers and flash lamps which are used for the optical pumping of solid state lasers, e.g. Nd:YAG laser.
3. Electron beam
   Large excimer lasers are pumped with a large-volume electron beam.
4. Current injection
   This method allows compact, robust and efficient laser device (LDs).
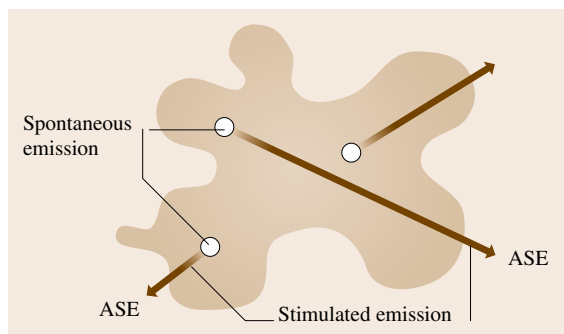
Fig. 11.13 Schematic illustration of amplified spontaneous emission. The *shaded area* shows an excited volume where population inversion is established

Laser Configuration

A combination of the population-inverted medium and the optical cavity which gives optical feedback provides the laser oscillation, which is like an electronic oscillator. Thus the laser consists of a laser medium, a pumping source and an optical cavity. Figure 11.14 shows a schematic arrangement of a laser. ASE with the correct frequency and direction of propagation is reflected back and forth through the laser medium. One of the mirrors, called the *output coupler*, is partially transparent to extract the light within the cavity. The cavity acts as a Fabry–Pérot resonator, so that the cavity modes are formed inside the cavity. The mode separation is expressed by

$$\Delta \nu = c/2l, \tag{11.60}$$

where l is a cavity length. We see lasing in the frequency region in which the intensity is above the threshold, as shown in Fig. 11.15. As seen in the figure, several modes oscillate simultaneously, which is called *multimode operation*. The random phases between these laser modes may cause a chaotic behavior of the output power. To avoid this effect, there are two solutions: *single-mode operation* in which a single cavity mode is selected by introducing another interferometer within the cavity and *mode-locked operation*, which is introduced in Sect. 11.4.2. The former operation achieves very narrow line widths down to 1 Hz.

Typical Lasers

Typical lasers are concisely summarized in the following. The lasers are classified depending on the laser media: gas, liquid and solid. Solid-state lasers are categorized into rare-earth metal lasers, transition-metal lasers
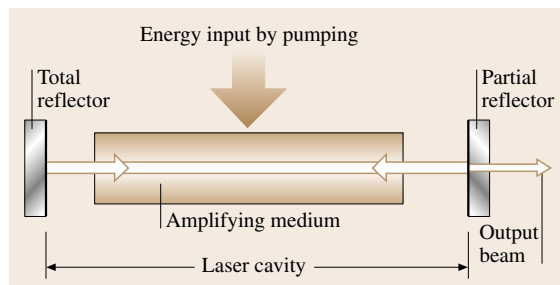
Fig. 11.14 Schematic arrangement of a laser. The partial reflector corresponds to the output coupler

and semiconductor lasers (LD). There are two laser operation modes: continuous wave (CW) and pulsed.

Gas lasers utilize atomic or molecular gases, as shown in Table 11.3. Though they are fixed-wavelength lasers in principle, multiple lines exist in molecular gas lasers and tunable operation is possible in CO_2 lasers. Excimer lasers utilize an excited diatomic molecule *excimer*, which is unstable in the ground state, and provide high-intensity pulses at UV wavelengths.

Dye lasers provide tunable operation, because dyes are organic molecules and have broad vibronic emission bands due to interaction with the solvent. Figure 11.16 shows the tuning range of typical dye lasers.

Solid-state lasers with transition-metal ions, as summarized in Table 11.4, also show broad emission bands (except the ruby laser) caused by the strong interac-
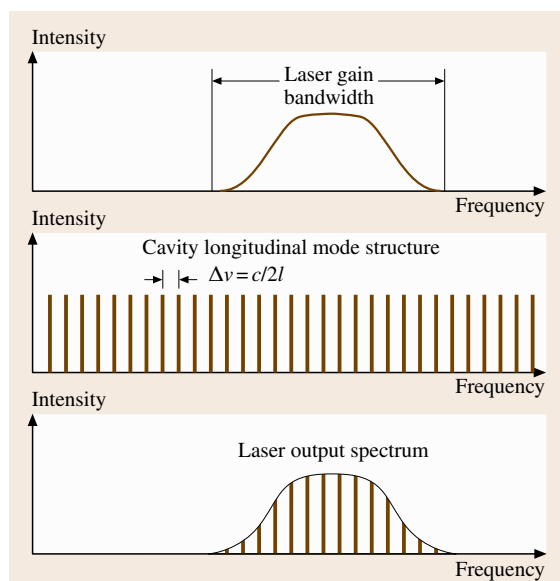
Fig. 11.15 Schematic illustration of laser output spectrum

Part C | 11.1

Table 11.3 Typical gas lasers

Laser media	Oscillation wavelength (μm)	Notes
He-Ne	0.6328, 1.15/1.52/3.39, 0.604/0.612, 0.594, 0.543	CW, used in metrology (length standard) and in optical alignment
He-Cd	0.636, 0.538, 0.442, 0.325	Typical CW laser in UV region
Cu (vapor)	0.511, 0.578	Pulse operation with 10 kHz repetition in visible region
Ar ion	0.275–1.09 (discrete), 0.515, 0.488 (typical lines)	Typical CW laser in visible region
CO_2	9–11 (tunable), 10.6	CW or pulse operation, giant pulse in infrared region, used in material processing
N_2	0.337	Compact pulsed laser
XeCl	0.308	Used in pumping for dye lasers
KrF	0.248	Highest power among excimer lasers
ArF	0.193	LSI fabrication
F_2	0.157	Commercially shortest wavelength

tion between 3d electrons and phonons, e.g. the Ti ion in sapphire provides very wide tuning range shown in Fig. 11.16 and are widely used, in particular, as ultrafast pulsed lasers (Sect. 11.4.2).

Solid-state lasers with rare-earth ions, as summarized in Table 11.5, work as fixed-wavelength lasers because of the narrow emission lines due to the weak interaction between 4f ions and their environments. They are pumped with flash lamps or LDs and, are themselves used for the optical pumping of tunable lasers.

Finally, semiconductor diode lasers, as summarized in Fig. 11.17, are nowadays most widely applied in tiny light sources for optical fiber communication, optical recording of CDs, DVDs, MOs, etc. Current injection is used for the laser pumping, which makes their combination with electronic circuitry feasible.

Fig. 11.16 Tuning range of typical dye and solid-state lasers

11.1.6 Scattering

Scattering is the phenomenon in which the incident light changes its wavevector or frequency. Scattering is called *elastic* if the frequency is unchanged, or *inelastic* if the frequency changes.

Elastic Scattering
This phenomenon occurs due to variation of the refractive index of the material. The scattering can be classified into two types depending on the size of the variation a as follows [11.18]

1. Rayleigh scattering: in the case of $a \ll \lambda$
   The probability (cross section) of Rayleigh scattering is proportional to $1/\lambda^4$.
2. Mie scattering: in the case of $a \geq \lambda$
   The size dependence of the probability of the Mie scattering is not simple but is approximately proportional to $1/\lambda^2$ in the case of $a \approx \lambda$. This phenomenon enables us to monitor the sizes of the particles in the air or in transparent liquid.

Inelastic Scattering
This phenomenon occurs due to fluctuation of the electric susceptibility of electrons or lattices in a material. The electric field E of the incident light and the polarization P of the material are described by (Sect. 11.1.4)

$$E = E_0 \cos \omega t ; \quad P = P_0 \cos \omega t . \quad (11.61)$$

If the fluctuation of the electric susceptibility can be written by

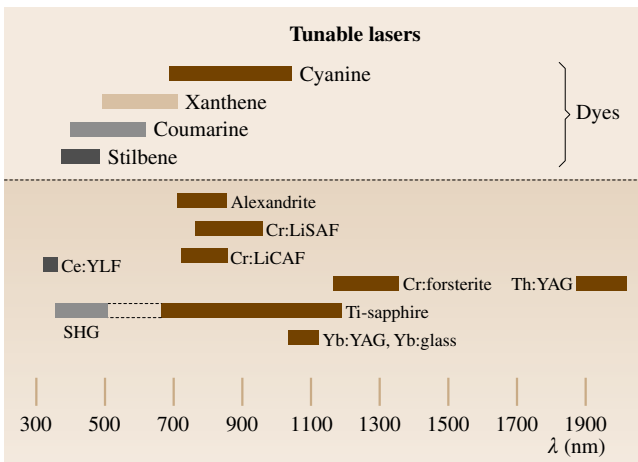$$\chi = \chi_0 + \chi' Q \cos \Omega t , \quad (11.62)$$

Table 11.4 Typical transition-metal-ion lasers

Laser media	Oscillation wavelength (μm)	Notes
Ruby (Cr:sapphire (Al_2O_3))	0.6943	Pulse, the first laser invented in 1960
Ti:sapphire (Al_2O_3)	0.65–1.1	CW or pulse, ultrafast pulse generation (Sect. 11.4.2)
Alexandrite (Cr:$BeAl_2O_4$)	0.70–0.82	CW or pulse, removal of hair, tattoos, and visible leg veins
Cr:LiSAF ($LiSrAlF_6$)	0.78–1.01	Pumped with LD, medical imaging and remote sensing
Cr:forsterite (Mg_2SiO_4)	1.13–1.35	Frequency-doubled range located at missing region covered with Ti:sapphire laser

Table 11.5 Typical rare-earth-ion lasers

Laser media	Oscillation wavelength (μm)	Notes
Nd:YAG	1.064	CW or pulse, used in material processing. SHG, THG and FHG are also used.
Nd:glass	1.062 (SiO_2 glass), 1.054 (PO glass)	CW or pulse, very strong pulse operation
Nd:YLF	1.053, 1.047, 1.323, 1.321	CW or pulse, good thermal stability
Nd:YVO_4	1.065	CW, pump source for Ti:sapphire laser
Yb:YAG	1.03	CW, used in a disk laser
Er:glass	1.54	CW, fiber laser, optical communication
Ce:LiSAF	0.285–0.299	UV operation

Compound	Laser media	Oscillation wavelength (μm)
III–V	InGaN AlGaAs GaInAsP AlGaInP AlGaAsSb	
IV–VI	InAsSbP PbSnSeTe PbS	
II–VI	CdZnSe MgZnSSe	
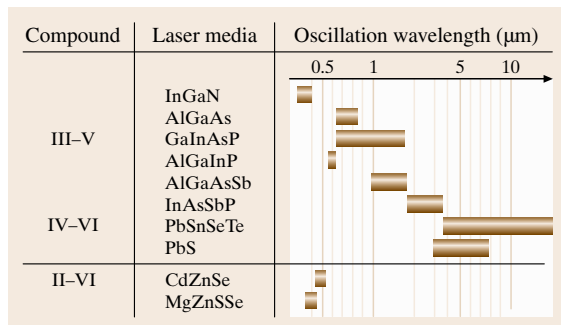
Fig. 11.17 Typical laser diodes

the polarization of the material is described as

$$P = \varepsilon_0 \chi E_0 \cos \omega t + \varepsilon_0 \chi' E_0 Q \cos \Omega t \cos \omega t$$
$$= \varepsilon_0 \chi E_0 \cos \omega t + \tfrac{1}{2} \varepsilon_0 \chi' E_0 Q$$
$$\times [\cos(\omega + \Omega)t + \cos(\omega - \Omega)t] \ . \tag{11.63}$$

The first term corresponds to the Rayleigh scattering and the second term means that new frequency components with $\omega \pm \Omega$, called *Raman scattering*, arises from the fluctuation. The down- and upshifted components are called the *Stokes scattering* and the *anti-Stokes scattering*, respectively.

In the case of the Raman scattering due to phonons, the Stokes (anti-Stokes) process corresponds to a phonon emission (absorption), as shown in Fig. 11.19. The scat-tering caused by acoustic phonons has a special name: *Brillouin scattering*. The frequency shift with respect to the incident light is called the *Raman shift*, and is determined by the phonon energy. In other words, the energy of the phonons or other elemental excitations can be obtained by Raman spectroscopy. Nowadays Raman spectroscopy is indispensable for material science and is applied to a huge number of materials [11.25].

Selection Rules for Raman Scattering

In the case of Raman or Brillouin scattering of phonons in crystals, energy and momentum conservation rules hold

$$\omega_i = \omega_s \pm \Omega \ , \tag{11.64}$$
$$k_i = k_s \pm K \ , \tag{11.65}$$

where ω_i and $k_i (\omega_s, k_s)$ are the frequency and wavevector of the incident (scattered) photon and Ω and K are those of the phonon. The plus sign corresponds to the Stokes process, which is shown in Fig. 11.20 and the minus sign corresponds to the anti-Stokes process.

If the incident light is in the optical region (from IR to UV), the wavevector is negligibly small in comparison with the Brillouin zone of the crystal. Hence, phonons with $q \approx 0$ are usually observed in the Raman scattering.

In a crystal with inversion symmetry, the phonon modes which are observed in the Raman scattering, called *Raman-active modes*, are not *infrared active* (not
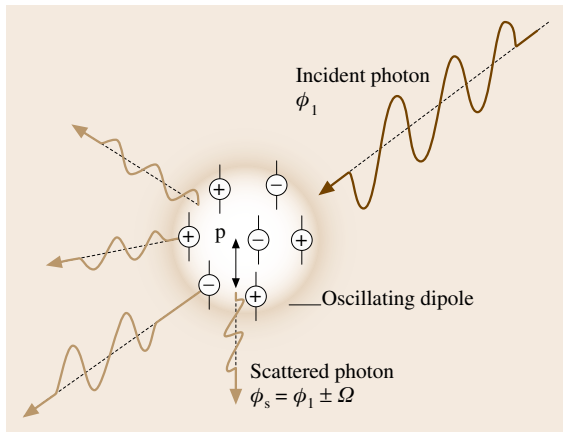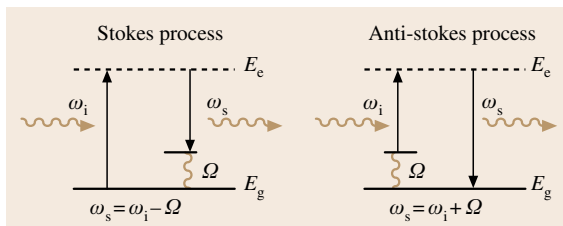
Fig. 11.18 Oscillator model for light scattering

Fig. 11.19 Energy-level diagram of the Raman processes. Stokes and anti-Stokes processes are illustrated

Fig. 11.20 Schematics of the Stokes scattering process. The wavevector conservation rule is also depicted

observed in the infrared absorption), and vice versa. This is called the *rule of mutual exclusion* [11.26].

In general, the coefficient χ' of the Raman scattering term in (11.62) is a tensor and is related to a Raman tensor $\boldsymbol{R}$, which is determined by the symmetry of the crystal or molecule. The intensity of the Raman scattering I is proportional to

$$I \propto |\boldsymbol{e}_i \boldsymbol{R} \boldsymbol{e}_s| \,, \tag{11.66}$$

where $\boldsymbol{e}_i$ and $\boldsymbol{e}_s$ are the polarization vectors of the incident and scattered light, respectively. The configuration for Raman spectroscopy is specified as $\boldsymbol{k}_i(\boldsymbol{e}_i\boldsymbol{e}_s)\boldsymbol{k}_s$ and the allowed combination of the polarizations are found if the Raman tensor $\boldsymbol{R}$ is given. This is called the *polarization selection rule* [11.26].

Electronic Raman Scattering

An electronic transition as well as a phonon is observed in the Raman scattering. This is called *electronic Ra-*
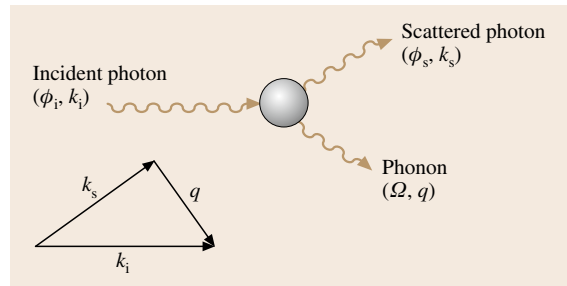
man scattering. This is a very useful probe for plasmons in semiconductors, magnons in magnetic materials, or in determining the superconducting gap and the symmetry of the order parameter of superconductors, in particular, strongly correlated electron systems; a new type of elementary excitation was found by this technique [11.27].

Resonant Raman Scattering

If the frequency of the incident light ω_i approaches the resonance of the material ω_0, the scattering probability is enhanced and the process is called *resonant Raman scattering*. In this case violation of the selection rules and multiple-phonon scattering occur. In the just-resonant case ($\omega_i \approx \omega_0$), the discrimination between the scattering, which is a coherent process, and the luminescence, an incoherent process, is a delicate problem. The time-resolved measurement of resonant Raman scattering reveals the problem and provides information on the relaxation process of the material [11.28].

Experimental Set-up

The configuration for Raman spectroscopy is similar to that used for luminescence spectroscopy, but a spectrometer with less stray light is required, because strong incident laser or Rayleigh scattering is located near the signal light. A double or triple spectrometer instead of a single spectrometer is usually used in Fig. 11.12 to reduce the stray light. An alternative method is to cut the laser light with a very narrow-line sharp-cut filter placed just in front of the entrance slit of a single spectrometer. This kind of filter is called a *notch filter*, which is a kind of dielectric multilayer interference filter.

11.2 Microspectroscopy

In nanoscience and nanotechnology the optical spectroscopic study of the individual properties of nanostructured semiconductor materials or biomolecules with ultrahigh spatial resolution is useful. This is achieved by avoiding the inhomogeneity caused by differences in the size, shape or surrounding environment. This kind of spectroscopy is called *single-quantum-dot or single-molecule spectroscopy*. In this section, we will introduce the principles and the application of three kinds of microspectroscopic methods based on conventional microscopy, near-field optical microscopy and cathodoluminescence spectroscopy with the use of scanning electron microscopy.

11.2.1 Optical Microscopy

Since light has a wave nature and suffers from diffraction, the spatial resolution of an optical microscope cannot go below approximately a half of the optical wavelength: the so-called diffraction limit. The typical set-up of microphotoluminescence spectroscopy is illustrated in Fig. 11.21. A laser beam for the photoexcitation source is focused on a sample surface with a spot diameter of about 1 μm through an objective lens with a high magnification factor. The luminescence from the sample is collected by the same objective lens and passed through an achromatic beam splitter to separate the luminescence from the scattered light of the excitation laser, and the luminescence image is focused onto a CCD camera or the luminescence spectrum is analyzed through the combination of spectrometer and intensified CCD camera.

The principle of single-quantum-dot or single-molecule spectroscopy is illustrated in Fig. 11.22. For example, the luminescence from the ensemble of quantum dots of semiconductors having a size distribution shows the inhomogeneous spectral broadening due to the size-dependent luminescence peak energy, as shown in Fig. 11.22a. If the spot size of the focused point is comparable to the mean separation distance between the quantum dots, the number of quantum dots detected by the objective lens is limited and the sharp luminescence lines with discrete photon energies are detected, as shown in Fig. 11.22c. If the distribution of the dots is dilute enough, one can detect a single dot, as shown in Fig. 11.22b where the line width is limited by intrinsic homogeneous broadening corresponding to the inverse of the phase relaxation time of the excited state.

As an example of laser microphotoluminescence spectroscopy, Fig. 11.23 shows the result of the ZnCdSe quantum dots grown on a ZnSe substrate [11.29]. Although the diameter of the quantum dots is 10 nm on average and has a wide size distribution, the microphotoluminescence spectra show the spiky structures that critically depend on the spot position of observation. From the top to the bottom spectra, the spot position is shifted successively by 10 μm distance. The bottom spectrum is taken at the original position to check the reproducibility, from which one notes that the change in the spectra comes from fluctuation not in time but in position.

As another example of single-molecule spectroscopy, Fig. 11.24 illustrates the microluminescence excitation spectroscopy for light-harvesting complexes LH2 acting as an effective light antenna in photosynthetic purple bacteria at 2 K [11.30]. The complexes contain two types of ring structure of bacteriochlorophyll molecules (BChl a) with 9 and 18 molecules stacked against each other. Since the 9- and 18-molecule rings have their absorption bands at 800 and 860 nm, respectively, the ensemble of LH2 complexes, as illustrated in curve (a), shows two broad peaks with inhomogeneous broadening caused by different surrounding environment. On the other hand, when the complexes are dilutely dispersed in polyvinyl acetate (PVA) polymer film, individual complexes are found to show different spectra, as illustrated in curves (b)–(f). Here sharp structures are found around
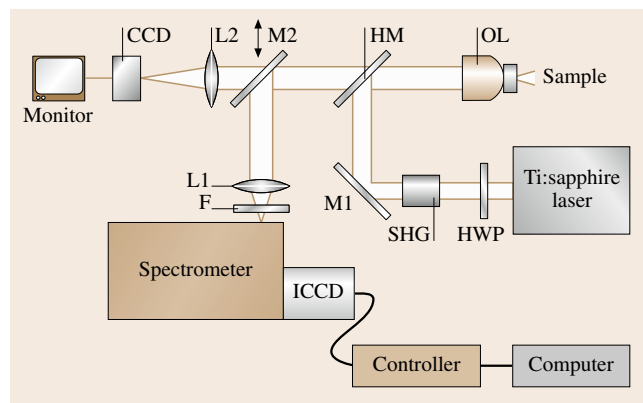
Fig. 11.21 Experimental set-up of microphotoluminescence spectroscopy. HM – dichroic reflection mirror for excitation light; OL – objective lens; HWP – half-wave plate; F – laser-blocking filter or linear polarizer
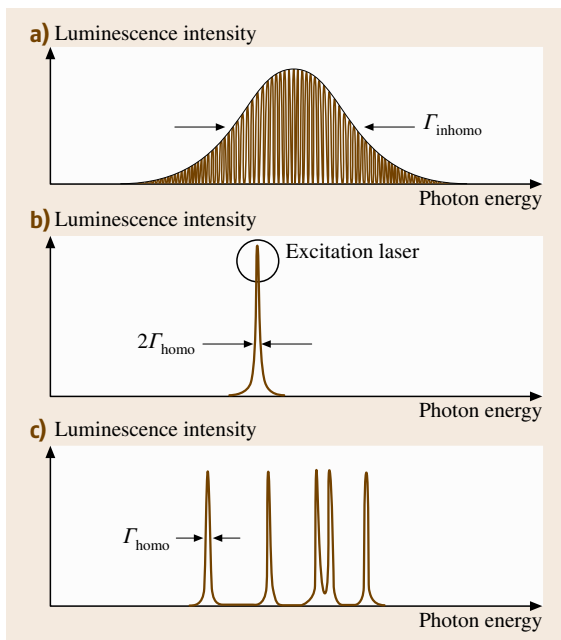
Fig. 11.22a–c Schematic drawing of luminescence spectra for samples with inhomogeneous broadening observed by: **(a)** broadband excitation, **(b)** site- or size-selective excitation, and **(c)** single-molecule/particle spectroscopy
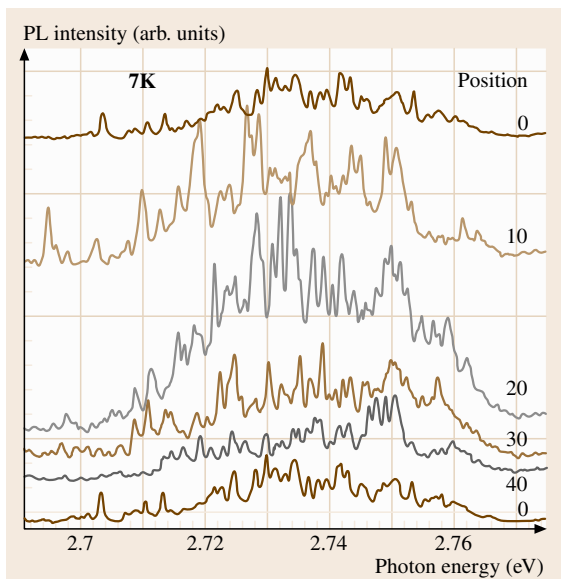
Fig. 11.23 Focussed position dependence of exciton luminescence of ZnCdSe quantum dots observed at 2 K by microphotoluminescence spectroscopy. The positions moved on a *straight line* are given in units of μm (after [11.29])

Fig. 11.24 Comparison of fluorescence-excitation spectra for an ensemble of LH2 complexes (a), and for several individual LH2 complexes (b–f) of photosynthetic bacteria at 1.2 K (after [11.30])
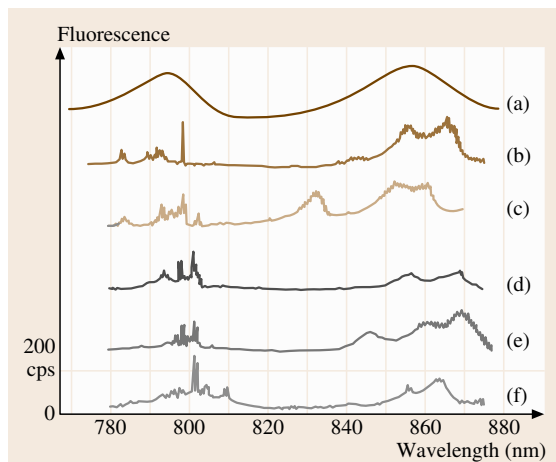
800 nm, while still broad structures around 860 nm. The former result indicates the localization of photoexcitation energy at one molecule, while the latter, indicates delocalization over the ring.

11.2.2 Near-field Optical Microscopy

In order to realize the spatial resolution beyond the diffraction limit, one can illuminate the sample with an extremely close light source of evanescent wave having large wavevectors produced from an aperture smaller than the wavelength of light. Here, the lateral resolution is mainly limited by the aperture size of the light source, if the distance between the light source and the sample surface is much smaller than the wavelength of light. Such a microscopy is called near-field optical microscopy. A schematic diagram of near-field microscope is illustrated in Fig. 11.25. One end of the optical fiber is sharpened by melting or chemically etching and used as a microprobe tip not only for the optical tips but also for atomic-force tips. To avoid the leakage of the light from the side of the tip end, the tip end is coated with Al or Au. The distance of the probe tip end from the surface of the sample is kept constant to within a few tens of nanometers using the principle of the atomic-force microscope (AFM). Laser light is sent through the optical fiber and the light emitted from the ultra-small aperture that illuminates the sample surface with a spot size similar to the aperture size (illumination mode). The transmitted or luminescent light from the sample is
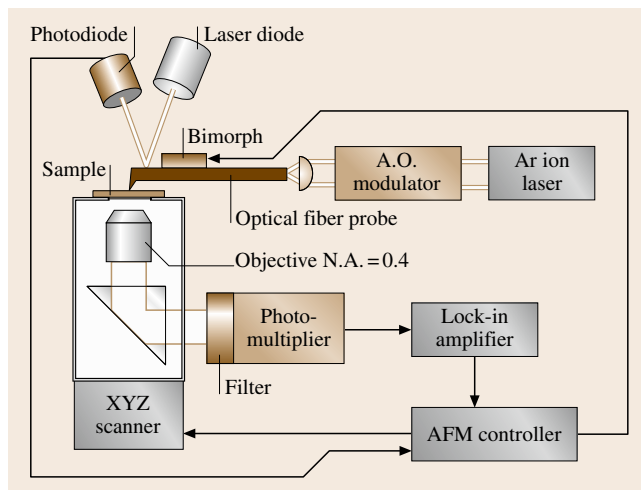
collected by an objective lens and detected by a photodetector such as photomultiplier. For luminescence measurements a band-pass filter or a monochromator is placed before the photodetector. In some case to improve the spatial resolution the reflected or luminescence light is again collected by the same probe tip (illumination/collection mode). The lateral position of the tip end or the sample is scanned on the X–Y plane and the two-dimensional intensity image of the optical response of the sample can be recorded together with the topographical image of the sample surface. The minimum spatial resolution using the optical fiber tip end is considered practically to be a few tens of nanometers.

Figure 11.26 illustrates the example of images of the double monolayer of a self-organized array of polystyrene microparticles with a diameter of 1 µm on a glass substrate [11.31]. Figure 11.26a shows the AFM image of the sample surface where the close packed hexagonal array is observed. The near-field transmission image using light from a 514.5 nm Ar ion laser is shown in Fig. 11.26b. Inside one microparticle indicated by a white circle, one can see seven small bright spots with a characteristic pattern. The spot size is about 150 nm, which is restricted by the aperture size. Since the distance between these spots depends on the wavelength of light, the pattern represents nanoscale field distribution of a certain electromagnetic wave mode standing inside the particle double layer.

Another example of monitoring the spatial distribution of the wave function of electronic excited states is shown in Fig. 11.27 [11.32]. The near-field luminescence images of confined excitons and biexcitons in GaAs single quantum dots are observed using the illumination/collection mode with a probe tip with an aperture size of less than 50 nm. The size of the image of the exciton is found to be larger than that of the biexciton, reflecting the difference in effective sizes for the translational motion of the electronically excited quasi-particles.

11.2.3 Cathodoluminescence (SEM–CL)

Cathodoluminescence (CL) spectroscopy is one of the techniques that can be used to obtain extremely high spatial resolution beyond the optical diffraction limit. Cathodoluminescence refers to luminescence from a substance excited by an electron beam, which is usually measured by means of the system based on a scanning electron microscope (SEM), as illustrated in Fig. 11.28. The electron beam is emitted from an electron gun of the SEM, collected by electron lenses and

Fig. 11.25 Schematic diagram of a scanning near-field optical microscope (SNOM) in illumination mode. Near-field light coming out from a fiber probe illuminates a sample. Transmitted light is collected by an objective lens and fed to a photomultiplier
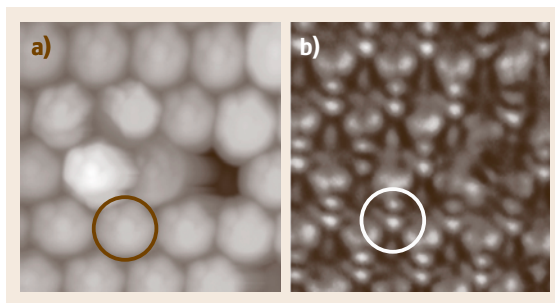
Fig. 11.26a,b 4.5 µm × 4.5 µm images of a double monolayer film of self-organized 1.0-mm polystyrene spherical particles on a glass substrate: **(a)** AFM topographic image, and **(b)** SNOM optical transmission image (after [11.31])

focused on a sample surface. The luminescence from the sample is collected by an ellipsoidal mirror, passed through an optical fiber and sent to a spectrometer equipped with a CCD camera. Lateral resolutions less than 10 nm are available in CL measurement, since the de Broglie wavelength of electrons is much shorter than light wavelengths. Moreover, energy- and wavelength-dispersive x-ray spectroscopy can be carried out simultaneously due to the high energy excitation of the order of keV. However, there are some difficulties in CL spectroscopy that are common to the observation of SEM images. A tendency toward charge accumulation at the irradiated spot requires that specimens have an elec-

a) X   [Ī10]

b) XX   [Ī10]

50 nm

50 nm

12   43
                 (cps)

12   30
               (cps)

c) PL intensity (cps)
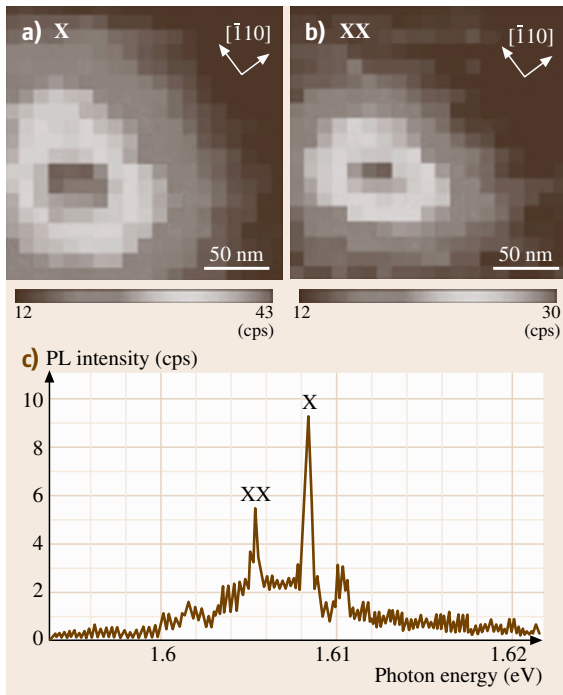
Fig. 11.27a–c High-resolution photoluminescence SNOM images of (**a**) X – exciton state, and (**b**) XX – biexciton state for a single GaAs quantum dot. The corresponding photoluminescence spectrum is also shown in (**c**) (after [11.32])

Fig. 11.28 Configuration of the CL measurement system based on SEM

Fig. 11.29 (**a**) Spectrally integrated CL image of ZnO:Zn particles, and (**b**) SEM image at the same position

tric conductivity, since it induces an electric field which disturbs the radiative recombination of carriers. In addition, incident electrons with high kinetic energy often give rise to degradation of the sample. In CL spectroscopy, it is important to recognize those properties and to treat samples with a metal coating if needed.

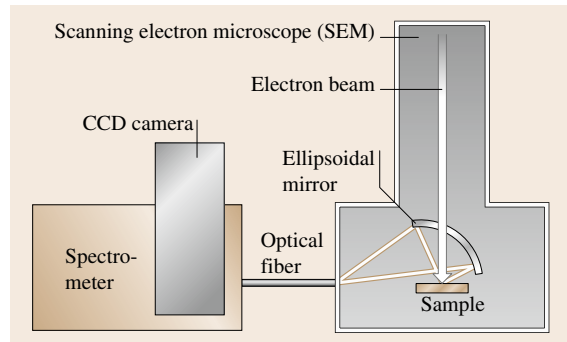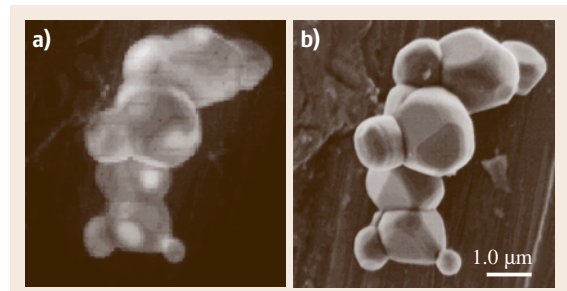Figure 11.29 illustrates an example of CL measurement on a system based on SEM. Spatial distribution of spectrally integrated CL intensity as well as SEM image is obtained, as shown in Fig. 11.29a,b. The sample is ZnO:Zn which corresponds to ZnO with many oxygen vacancies near the surface, and is a typical green phosphor. The CL image consists of 100×100 pixels, and the brightness of each pixel shows the CL intensity under the excitation within an area of 63×63 nm^2. The CL intensity is different among spatial positions at the nanoscale. The CL spectrum for each pixel can also be derived from this measurement, and the feature varies according to positions.

The penetration depth of incident electrons under electron-beam excitation is controllable by changing the accelerating voltage [11.33]. Electrons with high ki-

netic energy are able to penetrate deeper than photons which penetrate at most up to the depth corresponding to the reciprocal of the absorption coefficient, and therefore internal optical properties of substances can be examined in CL measurement. An example of accelerating voltage dependence of CL spectra is illustrated in Fig. 11.30. The sample is once again ZnO:Zn, in which free-exciton luminescence by photoexcitation is not observed at room temperature, since excitons are separated into electrons and holes due to the electric field in the surface depletion layer [11.34]. For an accelerating voltage of 2 kV, at which the penetration depth of incident electrons is comparable to the reciprocal of the absorption coefficient of photons, the CL spectrum does not show any structure in the exciton resonance region. On the other hand, the free exciton luminescence appears for an accelerating voltage of 5 kV, at which the penetration depth of the incident electrons is estimated to be about five times larger than that of photons. The luminescence is highly enhanced for an accelerating voltage of 10 kV, at which incident electrons are considered from the estimation of the penetration depth to spread throughout the electron-injected
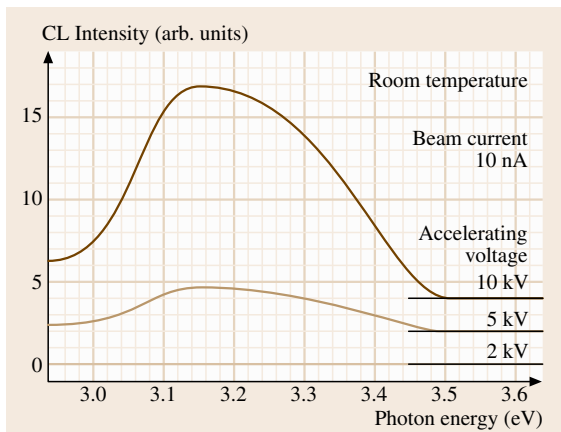
Fig. 11.30 Accelerating-voltage dependence of CL spectra in the exciton-resonance region at room temperature

ZnO:Zn particle. Although the total number of carriers in the particle increases with the accelerating voltage, the change in carrier density should be small because of the increase in excitation volume, i.e. nonlinear enhancement of the luminescence is not attributed to any high density effects. These facts indicate that injected

electrons penetrate into the internal region where many excitons can recombine radiatively due to the lower concentration of oxygen vacancies, and the width of the depletion layer in the particle is of the order of the reciprocal of the absorption coefficient.

The electric field in the depletion layer can be screened by increasing the density of photoexcited carriers. However, photoexcitation with high carrier density also induces strong nonlinear optical response near the exciton resonance region, such as exciton–exciton scattering and electron–hole plasmas [11.35]. In CL measurements, nonlinear effects do not appear in ZnO:Zn, since the carrier density under electron-beam excitation in the system based on SEM is much lower than that under photoexcitation using pulsed lasers. The free exciton luminescence does not appear with low accelerating voltage and low beam current, as shown in Fig. 11.30, whereas it can be observed with larger beam current. In CL spectroscopy, the internal electric field in the depletion layer is weakened with high efficiency and the free exciton luminescence near the surface can be observed without high density effects, since electrons are directly supplied into the oxygen vacancies, which are a source of the internal field.

11.3 Magnetooptical Measurement

11.3.1 Faraday and Kerr Effects

It is well known in magnetooptical effect that the polarization plane of an electromagnetic wave propagating through matter is rotated under the influence of a magnetic field or the magnetization of the medium [11.36]. This effect is called the Faraday effect, named after the discoverer *Michael Faraday* [11.37]. This effect is phenomenologically explained as the difference of the refractive index between right and left circular polarizations. In this effect the angle of optical rotation is called the Faraday rotation angle. In the case of low applied magnetic field the Faraday rotation angle θ_F is proportional to the sample thickness l and the applied magnetic field H. Thus θ_F is written as

$$\theta_F = VlH ,\qquad(11.67)$$

where V is called the Verdet constant. The Faraday effect appears even without a magnetic field in an optically active medium, e.g. saccharide, etc. Furthermore, the magnetic Kerr effect is the Faraday effect for reflected light [11.38]. This effect is ascribed to the phase difference between right and left circular polarizations

when the electromagnetic wave is reflected on the surface of a magnetic material.

For practical use the Faraday effect is utilized for imaging of magnetic patterns. These magnetic patterns have been experimentally studied by various techniques,

1. moving a tiny magnetoresistive or Hall-effect probe over the surface,
2. making powder patterns with either ferromagnetic or superconducting (diamagnetic) powders (Bitter decoration technique),
3. using the Faraday magnetooptic effect in transparent magnetic materials in contact with the surface of a superconducting film as a magnetooptic layer (MOL).

In order to get a high-resolution image of the magnetic pattern, one of these methods, Faraday microscopy (3 above), is the most useful [11.39, 40]. A schematic drawing of the Faraday imaging technique is shown in Fig. 11.31.

The linearly polarized light enters the MOL, in which the Faraday effect occurs and is reflected at the mirror layer. In areas without flux, no Faraday rotation

takes place. This light is not able to pass through the analyzer that is set in a crossed position with respect to the polarizer, hence the superconducting regions stay dark in the image. On the other hand, in regions where flux penetrates, the polarization plane of the incident light is rotated by the Faraday effect so that some light passes through the crossed analyzer, thus the normal areas will be brightly imaged.

Figure 11.31 shows the case of nonzero reflection angle, whereas in the experiment perpendicular incident light is normally used (Faraday configuration).

The Faraday rotation angle is transformed into light intensity levels. The sample surface is imaged onto a CCD detector array. In the case of crossed polarizer and analyzer the intensity of the signal from the CCD detector is

$$I(r, \lambda, B) = I_0(r, \lambda) \sin^2[\theta_F(r, \lambda, B)] + I_1(r, \lambda) ,$$
(11.68)

where r is the spatial coordinate on the CCD surface, λ is the wavelength of the incident light, B is the applied magnetic field, θ_F is the Faraday angle, and I_0 is the light intensity reflected by the sample. I_1 is the background signal ascribed to the dark signal of the CCD and residual transmission through the crossed polarizer and analyzer. When the analyzer is uncrossed by an angle θ,

$$I(r, \lambda, B) = I_0(r, \lambda) \sin^2[\theta + \theta_F(r, \lambda, B)] + I_1(r, \lambda) .$$
(11.69)

The angular position θ of the analyzer should be adjusted to obtain the best contrast between superconducting ($\theta_F = 0$) and normal ($\theta_F \neq 0$) areas. By changing the sign of θ, normal areas can appear brighter or darker than superconducting areas. In our experiment the angle
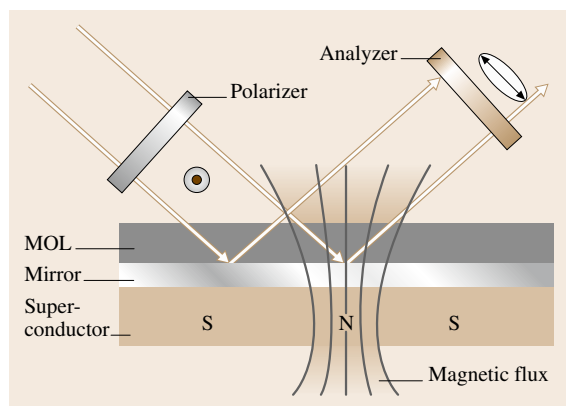

Fig. 11.31 Schematic drawing of the Faraday effect

θ is set to yield black in normal areas and gray in superconducting areas.

11.3.2 Application to Magnetic Flux Imaging

Experimental Set-up

Magnetooptical imaging is performed using a pumped liquid-helium immersion-type cryostat equipped with a microscope objective. This objective, with a numerical aperture of 0.4, is placed in the vacuum part of the cryostat and can be controlled from outside. The samples are studied in a magnetic field applied from exterior coils. The optical set-up is similar to a reflection polarizing microscope as shown in Fig. 11.32. Before measurement the samples are zero-field cooled to 1.8 K. The indium-with-QWs sample is illuminated with linearly polarized light from a Ti:sapphire laser, through a rotating diffuser to remove laser speckle. In the case of a lead-with-EuS sample a tungsten lamp with an interference filter is used the light source. Reflected light from the sample passes through a crossed or slightly uncrossed analyzer and is focused onto the CCD camera. The spatial resolution of $1 \, \mu m$ is limited by the numerical aperture of the microscope objective.

Magnetooptic Layers
Conventional magnetooptic layers. As for typical conventional MOLs, essentially, thin layers of Eu-based MOL (Eu chalcogenides, e.g. EuS and EuF_2 mixtures, EuSe) and doped yttrium iron garnet (YIG) films have been used [11.41]. These are usable up to the critical temperature of the ferromagnetic–paramagnetic transition ($\approx 15–20$ K) because their Verdet constants decrease with increasing temperature.

Since EuS undergoes ferromagnetic ordering below $T_c \approx 16.3$ K, a mixture of EuS with EuF_2 is better used. EuF_2 stays paramagnetic down to very low temperatures, therefore the ordering temperature of the mixture can be tuned by the ratio EuS : EuF_2. But there are several problems; difficulty of preparation due to difference of melting temperatures, and the need for a coevaporation technique.

Then the single-component EuSe layer has been further used because, even in the bulk, EuSe is paramagnetic down to 4.6 K and has a larger Verdet constant. Below 4.6 K, EuSe becomes metamagnetic, however, the reappearance of magnetic domains in the EuSe layers is not seen down to 1.5 K. However, there is also a problem owing to the toxicity of Se compounds.

On the other hand, due to their high transition temperature (Curie temperature), bismuth- and gallium-

doped yttrium-iron garnets (YIG) have been developed and used for the study of high-T_c superconductors. They are disadvantageous since they show ferrimagnetic domains, however, these MOLs are developed further by the introduction of ferrimagnetic garnet films with in-plane anisotropy. Using such films, the optical resolution is about 3 μm, but a direct observation of the magnetic flux patterns is possible and the advantages of the garnet films, i.e. high magnetic field sensitivity, large temperature range, are retained.

Generally this kind of MOL often has the demerit of poor spatial resolution because of their thickness of several micrometers. Furthermore, self-magnetic ordering that may modify the flux distributions in superconducting samples may limit their use. However, it was recently reported that an optimized ferrite garnet film allowed the observation of single flux quanta in superconducting NbSe₂ [11.42].

Novel magnetooptic layers. In this section we refer to an alternative type of MOL [11.39, 40] based on semimagnetic semiconductor (SMSC) $Cd_{1-x}Mn_xTe$. It consists of SMSC (also called diluted magnetic semiconductor (DMS)) $Cd_{1-x}Mn_xTe$ quantum wells (QWs) embedded in a semiconductor–metal optical cavity. It is well-known that SMSCs exhibit a large Faraday rotation mainly due to the giant Zeeman splitting of the excitonic transition ascribed to sp–d exchange interactions between spins of magnetic material and band electron spins. The most advantageous point is no self-magnetic ordering due to paramagnetic behavior of Mn ions. Therefore, it is very convenient since there is no possibility to modify the magnetic flux patterns of intermediate

state of type-I superconductors. There are several other advantages of this MOL. It is easy to increase Faraday rotation by making an optical cavity (metal/semiconductor/vacuum) with a thickness of $= (2n + 1)\lambda/4$. Multiple reflections of light take place inside the cavity. Moreover, in order to adjust the cavity thickness at the desired wavelength, a wedged structure is constructed. The highest spatial resolution is obtained when the superconducting film is evaporated directly onto the MOL. This is because, the smaller the distance between the MOL and the sample, the better the magnetic imaging becomes since there is little stray-field effect.

In addition to these ideas already proposed for conventional MOL (EuSe) [11.41], there is another strong point. Using QWs is also interesting due to low absorption, easy adjustment of the balance between absorption and Faraday rotation by choosing the number of QWs, and the possibility to have a thin active layer (QWs) in a thick MOL in order to keep good spatial resolution. When a $Cd_{1-x}Mn_xTe$ QW is inserted in an optical cavity the Faraday rotation can be further increased by using a Bragg structure, that is, placing the QWs at antinodes of the electric field in the optical cavity.

In order to make an optical cavity Al, or the superconductor itself if it is a good reflector, should be evaporated on top of the cap layer as a back mirror. In order to obtain the largest Faraday rotation, a minimum of the reflectivity spectrum has to be matched with the QWs transition. This is the resonance condition. However, the reflectivity, which decreases at the QW transition when the resonance condition is fulfilled, has to be kept to a reasonable level that is compatible with a good signal-to-noise ratio. Therefore an
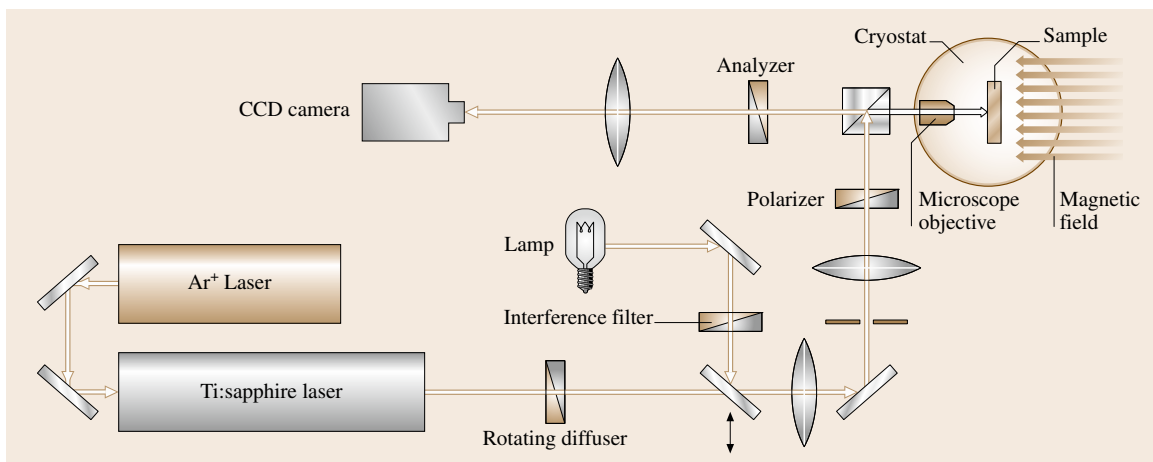
Fig. 11.32 Experimental set-up for the Faraday imaging technique

optimum number of QWs has to be found in multi-quantum-well structures. The Mn composition of the QWs also has to be optimized. It governs not only the Zeeman splitting of the excitonic transition but also the linewidth.

The time decay of the magnetization of the Mn ions in SMSC is known to be fast, in the subnanosecond range, since it is governed by spin–spin relaxation rather than by spin–lattice relaxation [11.43, 44]. This opens the way for time-resolved imaging studies with good temporal resolution, e.g. the study of the dynamics of flux penetration. On the other hand, there are also problems in fabrication. It is troublesome to remove the GaAs substrate by chemical etching while retaining fragile layers. Furthermore, the chemical etching solution strongly reacts with some metals e.g. lead.

Lead with europium sulfide magnetooptic layers. Since lead reacts strongly with the chemical etching solution used to remove the GaAs substrate from the
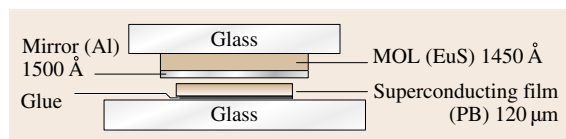
Fig. 11.33 Schematic drawing of Pb with EuS sample. The thickness of EuS, Al, and Pb are 145, 150 nm, and 120 μm, respectively. EuS is fabricated by Joule-effect evaporation. The EuS MOL is fixed on the Pb by pressing overnight

Fig. 11.34 *Right scale*: light reflection spectrum for zero applied magnetic field $H = 0$ mT at $T = 2$ K. *Left scale*: Faraday rotation-angle spectrum for $H = 53.3$ mT (after T. Okada, unpublished)

SMSC sample, we tried to use EuS as a MOL. The sample is shown in Fig. 11.33.

The thickness of the EuS MOL fabricated by Joule-effect evaporation on a 0.4 mm glass substrate is 145 ± 15 nm, hence it is thin enough for good spatial resolution. A 150-nm-thick Al layer is evaporated on the EuS MOL as a mirror in order to get high reflectivity. The EuS MOL is pressed onto Pb with a weight and left overnight.

A typical reflectivity spectrum and Faraday angle curve of EuS MOL are displayed in Fig. 11.34. The Ti:sapphire laser is tuned to 700 nm to get good reflected light and large Faraday rotation angle from the sample. Indeed EuS MOL may be expected to disturb the flux pattern, but no self-magnetic domain could be observed in this EuS sample, probably because the layer consists of a mixture of EuS and EuO. Figure 11.35 shows the images of the magnetic flux pattern at the surface of a 120-μm-thick superconducting lead film for magnetic field values of 20 mT. The temperature is 2 K, that is, much lower than the critical temperature of lead (7.18 K). The critical field of lead at 2 K is $H_c(2\,\text{K}) = 74.1$ mT.

The raw image has to be processed in order to correct the intensity fluctuations of the reflected light for thickness fluctuations in the MOL and for the sensitivity of CCD detector. In order to obtain an intensity level proportional to the Faraday angle, the gray level of each pixel should be calculated as

$$I' = I_H^{\alpha}/I_{H=0}^{\alpha} \,. \tag{11.70}$$

Fig. 11.35 The image of the magnetic flux patterns at the surface of 120-μm-thick superconducting Pb revealed with an EuS magneto-optical layer in an applied magnetic field of 20 mT ($h = 0.270$). Normal and superconducting domains appear in *black* and *gray*, respectively. The image size is 233 μm × 233 μm. The temperature is $T = 2$ K (after T. Okada, unpublished)
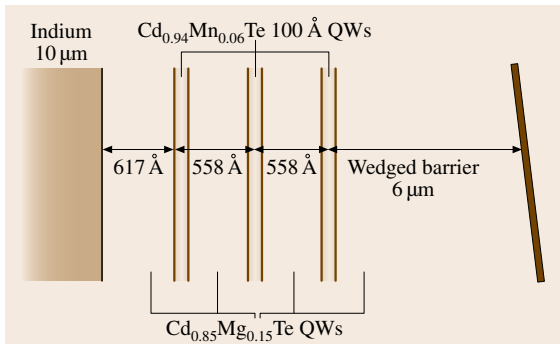
Fig. 11.36 Schematic representation of the sample composition (not to scale) after the etching of the GaAs substrate
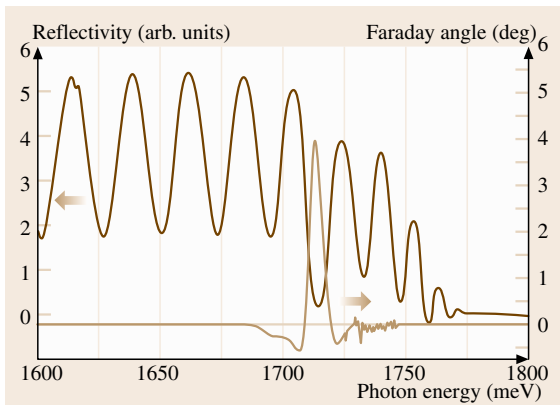
Fig. 11.37 *Left scale*: light reflection spectrum for zero applied magnetic field $H = 0$ mT at $T = 2$ K. *Right scale*: Faraday rotation-angle spectrum for $H = 56$ mT

where I_H^α is the raw gray level obtained for an applied field H and an analyzer angle α and θ is the Faraday angle. The quality of the image is further improved by Fourier-transform filtering, but the magnetic contrast is not very good because the contact between lead and the MOL may not be as good as for an evaporated metallic sample.

Indium with quantum–well magnetooptic layers.
The sample consists of an indium layer as the superconducting material and a $Cd_{1-x}Mn_xTe/Cd_{1-y}Mg_yTe$ heterostructure as the MOL. The structure is sketched in Fig. 11.36 [11.40].

The semiconductor heterostructure was grown by molecular beam epitaxy. The $Cd_{0.85}Mg_{0.15}Te$ buffer was deposited on (001)GaAs substrate without rotation of the sample holder, resulting in a slight gradient of both the thickness of the buffer and its refrac-
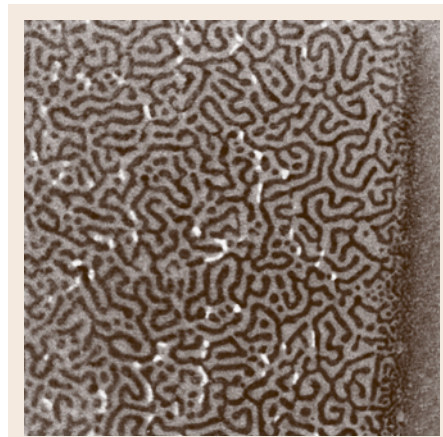
Fig. 11.38 The image of the magnetic flux patterns at the surface of 10-µm-thick superconducting In film revealed with the $Cd_{1-x}Mn_xTe$ QWs structure as the magneto-optical layer in an applied magnetic field of 6.3 mT ($h = 0.325$). Normal and superconducting domains appear in *black* and *gray*, respectively. The edge of the indium film can be seen on the right-hand side of images where the flux pattern disappears. The image size is 527 µm × 527 µm. The analyzer was uncrossed by $\alpha = 20°$ with respect to the polarizer. The temperature is $T = 1.9$ K (after T. Okada, unpublished)

tive index. The buffer was followed by three 10-nm $Cd_{0.94}Mn_{0.06}Te$ QWs separated by $Cd_{0.85}Mg_{0.15}Te$ barriers that were 55.8 nm thick. A 10-µm-thick indium layer was then evaporated directly on top of the 61.7-nm $Cd_{0.85}Mg_{0.15}Te$ cap layer. The MOL is designed as an optical cavity and indium serves both as the superconducting layer and the cavity back mirror. The first and third QWs are nearly located at antinodes of the electric field in the cavity in order to enhance Faraday rotation. The indium-covered side was glued onto a glass plate and the GaAs substrate was removed by mechanical thinning and selective chemical etching. For the Faraday microscopy the spatial resolution was checked as 1 µm, with a magnetic resolution of 10 mT; the range of temperature for use should be up to 20 K.

A typical reflectivity spectrum and Faraday angle curve are displayed in Fig. 11.37. The reflectivity spectrum presents an interference pattern associated with the metal/semiconductor/vacuum optical cavity. This pattern shows a spectral shift when the illuminating spot is scanned along the sample surface, according to the thickness variation of the cavity. The maximum Faraday angle is observed when a minimum of reflec-

tivity is matched with the QW transition energy (the cavity resonance condition). The peak Faraday angle was found to vary linearly with the applied magnetic field H. The measured slope equals $54.4° \, \mathrm{T}^{-1}$ at the QWs (e1-hh1) exciton transition. Fig. 11.38 shows an intermediate state structure at the surface of the indium superconducting layer obtained at $T = 1.9 \, \mathrm{K}$ at magnetic field values $6.3 \, \mathrm{mT}$. The critical field of indium at $1.9 \, \mathrm{K}$ is $19.4 \, \mathrm{mT}$.

Black and gray areas are normal and superconducting state, respectively. The intricate flux pattern results from the competition between long-range repulsive magnetic interactions between normal zones and short-range interactions due to the positive interfacial energy between normal and superconducting areas [11.45, 46].

In the same way as for the lead sample, the raw images were processed in order to eliminate intensity fluctuations of the reflected light due to thickness inhomogeneities of the MOL and the sensitivity of CCD detector. The quality of the image is further improved compared with Fig. 11.35.

11.4 Nonlinear Optics and Ultrashort Pulsed Laser Application

Nonlinear optical effects with lasers are utilized in frequency conversion, optical communication (Sect. 11.5) and spectroscopy of materials. This chapter deals with nonlinear optics and its application to pulsed lasers.

11.4.1 Nonlinear Susceptibility

Definition of Nonlinear Susceptibility and Symmetry Properties

Nonlinear optical phenomena originate from nonlinearity of materials. Linear and nonlinear polarization induced in the material is expressed as follows

$$P_i = \chi_{ij} E_j + \chi_{ijk}^{(2)} E_j E_k + \chi_{ijkl}^{(3)} E_j E_k E_l + \cdots ,$$
(11.71)

where i, j, k and l represent x, y, or z and $\chi^{(n)}$, which is an $(n+1)$th-rank tensor, is called the n-th-order *nonlinear optical susceptibility*. Each term corresponds to the n-th order polarization

$$P_{i_1}^{(n)} = \chi_{i_1 i_2 \cdots i_{n+1}}^{(n)} \overbrace{E_{i_2} E_{i_3} \cdots E_{i_{n+1}}}^{n} ,$$
(11.72)

where $i_1, i_2, \ldots,$ or i_{n+1} represents x, y, or z. The second-order nonlinearity in the argument ω is described by

$$P_i^{(2)}(\omega_1 + \omega_2) = \chi_{ijk}^{(2)}(\omega_1 + \omega_2; \omega_1, \omega_2)$$
$$\times E_j(\omega_1) E_k(\omega_2) .$$
(11.73)

The $\chi^{(2)}$ tensor has the following symmetry properties [11.47].

1. Intrinsic permutation symmetry

$$\chi_{ijk}^{(2)}(\omega_1 + \omega_2; \omega_1, \omega_2) = \chi_{ikj}^{(2)}(\omega_1 + \omega_2; \omega_2, \omega_1)$$
(11.74)

2. Permutation symmetry for materials without losses

$$\chi_{ijk}^{(2)}(\omega_1 + \omega_2; \omega_1, \omega_2)$$
$$= \chi_{jki}^{(2)}(\omega_1; -\omega_2, \omega_1 + \omega_2)$$
$$= \chi kij^{(2)}(\omega_2; \omega_1 + \omega_2, -\omega_1)$$
(11.75)

3. Kleinman's relation (for the nonresonant case $\chi^{(2)}$ is independent of the frequency ω)

$$\chi_{ijk}^{(2)} = \chi_{jki}^{(2)} = \chi_{kij}^{(2)} = \chi_{ikj}^{(2)} = \chi_{jik}^{(2)} = \chi_{kji}^{(2)} ,$$
(11.76)

where the arguments are $(\omega_1 + \omega_2; \omega_1, \omega_2)$. A consideration of crystal symmetry allows us to reduce the number of elements of the $\chi^{(n)}$ tensor of the material [11.47, 48]. A typical example is as follows. If the material has inversion symmetry,

$$-P_i^{(2)} = \chi_{ijk}^{(2)}(-E_j)(-E_k) ,$$
$$P_i^{(2)} = 0 .$$

In the same way, we obtain

$$P^{(2n)} = 0 \quad (n : \text{integer}) .$$

Then if the material has inversion symmetry,

$$\chi^{(2n)} = 0 \quad (n : \text{integer}).$$
(11.77)

Oscillator Model Including Nonlinear Interactions

The nonlinear optical susceptibility can be calculated quantum mechanically using the density matrix formalism [11.47]. Here we use a classical model [11.49], modifying the Lorentz oscillator model (11.15) to include nonlinear interactions of light and matter as follows

$$m \frac{\mathrm{d}^2 x}{\mathrm{d}t^2} = -m\gamma \frac{\mathrm{d}x}{\mathrm{d}t} - m\omega_0^2 x - am x^2$$
$$- bm x^3 + e E(t) ,$$
(11.78)

where the third and fourth terms on the right-hand side correspond to the second- and third-order anharmonic potentials, respectively. Here we assume that the driving term can be expressed by

$$E(t) = \{E_1[\exp(-i\omega_1 t) + \exp(i\omega_1 t)]$$
$$+ E_2[\exp(-i\omega_2 t) + \exp(i\omega_2 t)]\}/2 . \quad (11.79)$$

We can solve (11.78) by perturbative expansion of $x(t)$ in powers of the electric field $E(t)$,

$$x(t) \equiv x^{(1)} + x^{(2)} + x^{(3)} + \cdots ,$$

where $x^{(i)}$ is proportional to $[E(t)]^i$. Then we get the successive equations as follows

$$\frac{d^2 x^{(1)}}{dt^2} + \gamma \frac{dx^{(1)}}{dt} + \omega_0^2 x^{(1)} = \frac{eE(t)}{m} , \quad (11.80)$$

$$\frac{d^2 x^{(2)}}{dt^2} + \gamma \frac{dx^{(2)}}{dt} + \omega_0^2 x^{(2)} = a(x^{(1)})^2 , \quad (11.81)$$

$$\frac{d^2 x^{(3)}}{dt^2} + \gamma \frac{dx^{(3)}}{dt} + \omega_0^2 x^{(3)} = 2ax^{(1)}x^{(2)}$$
$$+ b(x^{(1)})^3 . \quad (11.82)$$

If we define a common denominator

$$D(\omega) \equiv \frac{1}{\omega_0^2 - \omega^2 - i\gamma\omega} , \quad (11.83)$$

the solution of (11.80) is expressed by

$$x^{(1)} = [E_1 D(\omega) \exp(-i\omega_1 t)$$
$$+ E_2 D(\omega) \exp(-i\omega_2 t)] \times e/(2m) + \text{c.c.} , \quad (11.84)$$

where c.c. means complex conjugate. This is just a superposition of (11.95). Then we substitute this result for the right-hand side of (11.81). The solution consists of five groups as follows

$$x^{(2)}(2\omega_1) = -[E_1^2 D(2\omega_1)D(\omega_1)^2$$
$$\times \exp(-2i\omega_1 t)]a e^2/(4m^2) + \text{c.c.} , \quad (11.85)$$

$$x^{(2)}(2\omega_2) = -[E_2^2 D(2\omega_2)D(\omega_2)^2$$
$$\times \exp(-2i\omega_2 t)]a e^2/(4m^2) + \text{c.c.} , \quad (11.86)$$

$$x^{(2)}(\omega_1 + \omega_2) = -\{E_1 E_2 L(\omega_1 + \omega_2)D(\omega_1)D(\omega_2)$$
$$\times \exp[-i(\omega_1 + \omega_2)t]\}a e^2/(2m^2)$$
$$+ \text{c.c.} , \quad (11.87)$$

$$x^{(2)}(\omega_1 - \omega_2) = -\{E_1 E_2^* D(\omega_1 - \omega_2)D(\omega_1)D(\omega_2)^*$$
$$\times \exp[-i(\omega_1 - \omega_2)t]\}\frac{a e^2}{2m^2} + \text{c.c.} , \quad (11.88)$$

$$x^{(2)}(0) = -[|E_1|^2 D(\omega_1) + |E_2|^2 D(\omega_2)]$$
$$\times \frac{a e^2}{2m^2} . \quad (11.89)$$

These equations indicate that new frequency components arise from the second-order nonlinearity. These components are used in frequency conversion. Details are discussed in the following subsection.

Next, the third-order nonlinearity is treated similarly, assuming three frequency components

$$E(t) = [E_1 \exp(-i\omega_1 t) + E_2 \exp(-i\omega_2 t)$$
$$+ E_3 \exp(-i\omega_3 t)]/2 + \text{c.c.} \quad (11.90)$$

Then using (11.82–11.89) for all combinations of ω_1, ω_2 and ω_3, we finally obtain 22 groups

$x^{(3)}$ for $\omega_1 + \omega_2 + \omega_3, \omega_1 + \omega_2 - \omega_3, \omega_1 - \omega_2 + \omega_3,$
$\quad -\omega_1 + \omega_2 + \omega_3, 2\omega_1 \pm \omega_2, 2\omega_1 \pm \omega_3,$
$\quad 2\omega_2 \pm \omega_3, 2\omega_2 \pm \omega_1, 2\omega_3 \pm \omega_1, 2\omega_3 \pm \omega_2,$
$\quad \omega_1, \omega_2, \omega_3, 3\omega_1, 3\omega_2 \text{ and } 3\omega_3 .$

For example,

$$x^{(3)}(\omega_1, \omega_2, -\omega_2)$$
$$= -E_1 E_2 E_2^* D(\omega_1)^2 D(\omega_2)D(\omega_2)^* \exp(-i\omega_1 t)$$
$$+ \text{c.c.} , \quad (11.91)$$

$$x^{(3)}(\omega_1, \omega_1, -\omega_2)$$
$$= -E_1^2 E_2^* D(2\omega_1 - \omega_2)D(\omega_1)^2 D(\omega_2)^*$$
$$\times \exp[-i(2\omega_1 - \omega_2)t]\left[\frac{3b}{2} - 2a^2 D(\omega_1 - \omega_2)\right.$$
$$\left. - a^2 D(2\omega_1)\right]\frac{e^2}{4m^3} + \text{c.c.} \quad (11.92)$$

The i-th-order polarization is given by

$$P^{(i)} = -nex^{(i)} . \quad (11.93)$$

Then from (11.72), (11.91) we obtain a frequency component of the third-order polarization

$$P^{(3)}(\omega_1) = neD(\omega_1)^2|D(\omega_2)|^2|E(\omega_2)|^2 E(\omega_1)$$
$$\equiv \chi^{(3)}(\omega_1; \omega_1 + \omega_2 - \omega_2)$$
$$\times |E(\omega_2)|^2 E(\omega_1) . \quad (11.94)$$

This term means that the optical constant, e.g. refractive index n for the ω_1 light, can be controlled by the other light of ω_2.

Part C | 11.4

Table 11.6 Values of $\chi^{(2)}$ for typical nonlinear crystals

Material	Maximum value of $\chi^{(2)}$ (10^{-8} esu)	Fundamental wavelength (μm)
α-SiO$_2$	0.19	1.06
Te	2.5×10^3	10.6
BaNaNb$_5$O$_{15}$	9.6	1.06
LiNbO$_3$	19	1.06
BaTiO$_3$	-8.5	1.06
ADP (NH$_4$H$_2$PO$_4$)	0.24	0.694
KDP (KH$_2$PO$_4$)	0.25	1.06
β-BBO (BaB$_2$O$_4$)	0.98	1.06
ZnO	-3.3	1.06
LiIO$_3$	-2.8	1.06
CdSe	26	10.6
GaAs	95	10.6
GaP	18	3.39

Estimation of Nonlinear Susceptibility

We can estimate the value of $\chi^{(2)}$ using the anharmonic oscillator model, e.g. in the case of (11.84) as follows

$$P^{(2)}(\omega_1 + \omega_2) = -nex^{(2)}$$
$$\equiv \chi^{(2)}(\omega_1 + \omega_2, \omega_1, \omega_2) E(\omega_1) E(\omega_2) ,$$
(11.95)

if we neglect the complex conjugate term,

$$\chi^{(2)}(\omega_1 + \omega_2, \omega_1, \omega_2)$$
$$= \frac{D(\omega_1 + \omega_2) D(\omega_1) D(\omega_2) n a e^3}{m^2} .$$
$$= \frac{\chi^{(1)}(\omega_1 + \omega_2) \chi^{(1)}(\omega_1) \chi^{(1)}(\omega_2) m a}{N^2 e^3} .$$

Then we obtain *Miller's rule*

$$\chi^{(2)} \frac{\omega_1 + \omega_2, \omega_1, \omega_2}{\chi^{(1)}(\omega_1 + \omega_2) \chi^{(1)}(\omega_1) \chi^{(1)}(\omega_2)} = \frac{ma}{n^2 e^3} (\text{const.}) .$$
(11.96)

The density is estimated approximately

$$n \approx \frac{1}{d^3} ,$$

where d is a lattice constant. If we assume $m\omega_0^2 d = mad$,

$$a = \frac{\omega_0^2}{d} .$$

In the nonresonant case, the denominator is approximated by

$$D(\omega) \approx \frac{1}{\omega_0^2} .$$

Table 11.7 Second-order nonlinear effects

Name of frequency conversion	Conversion process
Second harmonic generation (SHG)	$\omega \to 2\omega$
Sum frequency generation (SFG)	$\omega_1, \omega_2 \to \omega_1 + \omega_2$
Difference frequency generation (DFG)	$\omega_1, \omega_2 \to \omega_1 - \omega_2$
Optical rectification (OR)	$\omega \to 0$ (DC)
Optical parametric generation (OPG)	$\omega \to \omega_1, \omega_2$ ($\omega = \omega_1 + \omega_2$)

Finally we can estimate the value of $\chi^{(2)}$

$$\chi^{(2)} \approx \frac{e^3}{m^2 \omega_0^4 d^4}$$
$$\approx 10^{-8} \text{ esu} ,$$
(11.97)

if we assume $\omega_0 \approx 10^{16}$ s^{-1} and $d \approx 0.1$ nm. Table 11.6 shows values of $\chi^{(2)}$ for typical nonlinear crystals.

Frequency Conversion

As seen in (11.85–11.89), second-order nonlinearity enables frequency conversion by mixing of two photons. Frequency conversion processes using $\chi^{(2)}$ are summarized in Table 11.7.

Second-harmonic generation (SHG), expressed by (11.85), is widely used for generation of visible or ultraviolet lights, because most solid-state lasers including LDs deliver infrared or red lights; e.g. a green line at 532 nm is the SH of a Nd:YAG laser (1064 nm) and near-UV region (350–500 nm) is covered by the SH of a Ti:sapphire laser (Fig. 11.16). The SHG is also used to measure the pulse width of an ultrashort pulsed laser (Sect. 11.4.3).

Sum-frequency generation (SFG) in (11.87) is also used for the generation of the higher frequency region from the lower frequency region; the third-harmonic generation (THG) at 355 nm is achieved by SFG of the SH and fundamental of the Nd:YAG laser. The SFG provides up-conversion spectroscopy (Sect. 11.4.3).

Difference-frequency generation (DFG) in (11.88) is used for generation of infrared light. A combination of DFG and OPO enables us to tune the frequency in the infrared region (3–18 μm) with AgGaS$_2$ or GaSe crystals. *Optical rectification* (OR) in (11.89) is a special case of DFG and provides ultra-broadband infrared pulse generation by using femtosecond lasers (Sect. 11.4.5).

Optical-parametric generation (OPG) is the reverse process of SFG; one photon is divided into two pho-
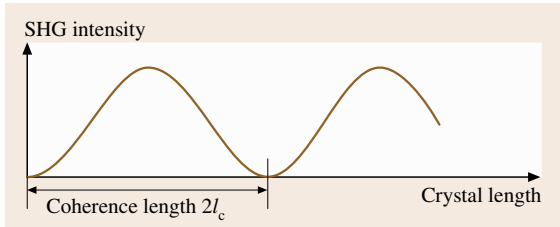
Fig. 11.39 SHG intensity with respect to crystal length

tons. This process is utilized in a tunable laser, *optical-parametric oscillator* (OPO), pumped with a fixed-frequency laser.

Phase-matching condition is crucial for efficient frequency conversion [11.47]. The wavevector should be conserved in the frequency conversion processes; in the SHG case the phase-matching condition is described by

$$k(2\omega) = 2k(\omega) , \quad (11.98)$$

where $k(\omega)$ is the wavevector at frequency ω. In other cases, the converted component 2ω and the incident component ω interfere with each other destructively, as seen in Fig. 11.39. Here the *coherence length* l_c is defined by

$$l_c = \frac{\pi c}{2}[\omega|n(\omega) - n(2\omega)|] , \quad (11.99)$$

where $n(\omega)$ is the refractive index at frequency ω. The condition in (11.98) means that l_c becomes infinity. The phase-matching condition can be achieved using birefringence of a nonlinear crystal [11.47].

Third−order Nonlinear Effects

The third-order nonlinearity causes a variety of effects, which are summarized in Table 11.8.

Though the *third-harmonic generation* (THG) is used in frequency conversion, this process is useful for obtaining the spectroscopic information on the magnitude of $\chi^{(3)}$ or electronic structures, which is called *THG spectroscopy* [11.50].

Refractive index of the material depends on the intensity of the incident light as follows

$$n = n_0 + n_2 I , \quad (11.100)$$

where n_2 is nonlinear refractive index and I is the intensity of the light. As already seen in (11.94), the n_2 is proportional to $\chi^{(3)}$

$$n_2 = \frac{\chi^{(3)}}{n_0^2 c \varepsilon_0} . \quad (11.101)$$

This refractive index change that is dependent on the light intensity is called the *optical Kerr effect* (OKE), and

Table 11.8 Third-order nonlinear effects

The third-order effect	Notes
Third-harmonic generation (THG)	$\omega \rightarrow 3\omega$
Optical Kerr effect (OKE)	$n \rightarrow n_0 + n_2 I$
Two-photon absorption (TPA)	$\alpha \rightarrow \alpha_0 + \beta I$
Four-wave mixing (FWM)	$\omega_1, \omega_2, \omega_3 \rightarrow \omega_4$

produces a nonlinear phase shift $\Delta \Phi$

$$\Delta \Phi = \frac{2\pi}{\lambda} n_2 I l , \quad (11.102)$$

where l is the sample length. The nonlinear phase shift is utilized in optical switching (Sect. 11.5). The OKE gives rise to transverse variations of a light beam which cause the wavefront distortion that leads to *self-focusing* [11.47], used in Kerr lens mode-locking (Sect. 11.4.2) or Z-scan measurement (Sect. 11.4.4). The OKE also leads to temporal variations of the phase of the light pulse, called *self-phase modulation* (SPM), which cause frequency shift, called *frequency chirp* [11.51], shown in Fig. 11.40. If a strong beam is focused on a material with large nonlinearity, *white-light continuum* can be generated via the SPM. This phenomenon is widely used in spectroscopy (Sect. 11.4.4).

The imaginary part of the complex refractive index also depends on the intensity of the incident light due to the third-order nonlinearity. Thus the absorption coefficient is defined by

$$\alpha(I) = \alpha + \beta I , \quad (11.103)$$

where β is called the *two-photon absorption* (TPA) coefficient. TPA is explained in Sect. 11.4.4. We apply the Kramers–Kronig relation (11.21) to the nonlinear optical constants

$$n_2(\omega) = \frac{c}{\pi} \int_0^\infty \frac{\beta(\omega')}{\omega'^2 - \omega^2} d\omega' . \quad (11.104)$$
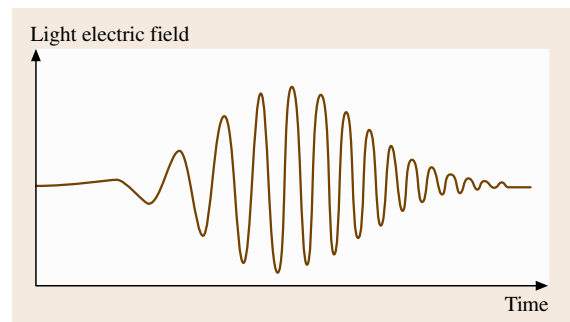
Fig. 11.40 Schematic illustration of a frequency chirp. The instantaneous frequency changes from red to blue

Four-wave mixing (FWM) is a general name for the third-order nonlinear optical processes and has a number of variations. Its spectroscopic application is introduced in Sect. 11.4.4.

11.4.2 Ultrafast Pulsed Laser

Properties of Ultrashort Pulses [11.51]

The relationship between a temporal profile (envelope of the electric power $|E(t)|^2$) and a spectral shape is illustrated in Fig. 11.41. A CW laser, in particular a single-mode laser, delivers monochromatic light and the envelope is independent of time, as shown in Fig. 11.41a. On the other hand, a pulsed laser produces a pulsed light which consists of a number of frequency components; the pulse duration Δt and spectral width $\Delta \nu$ are finite in Fig. 11.41b. The relation between them is determined by the Fourier transformation

$$\Delta \nu \Delta t \geq K , \tag{11.105}$$

where K is a constant determined by the pulse shape function, as shown in Table 11.9. The equal sign is valid only for pulses without frequency modulation and such pulses are called *Fourier-transform-limited*. This inequality corresponds to the uncertainty relation between energy and time in quantum mechanics.

The temporal shape of the utrashort pulses with very broad spectral width is easily distorted by *group velocity dispersion*, $dv_g/d\omega$ [11.51], where v_g is a group velocity; the red component propagates through the material normally faster than the blue component. If the original pulse envelope is described by a Gaussian $\exp(-t^2/\tau_0^2)$,

the pulse width broadens as

$$\tau = \tau_0 \sqrt{1 + \left(\frac{|GDD|}{\tau_0^2}\right)^2} , \tag{11.106}$$

where the *group delay dispersion* (GDD) is written as

$$GDD(\omega) = l \frac{d^2}{d\omega^2}\left[\frac{\omega}{c}n(\omega)\right] , \tag{11.107}$$

where l is the sample length. The GDD is related to the group velocity dispersion as follows

$$GDD(\omega) = \frac{d}{d\omega}\left(\frac{l}{v_g}\right) . \tag{11.108}$$

The compensation of the pulse broadening in (11.106) is crucial when dealing with ultrashort pulses.

The time width of the ultrashort pulses is determined by an *auto-correlator* in Fig. 11.42. The incoming pulse is divided in a beam splitter; a part of the light passes through a fixed delay line, while the other part passes through a variable delay line. They overlap on the nonlinear crystal surface and SHG occurs. The intensity of the SH light with respect to the time delay τ corresponds to the *autocorrelation function* $I_A(\tau)$ of the input pulse $I(t)$ as follows

$$I_A(\tau) = \int I(t)I(t-\tau)\,dt . \tag{11.109}$$

The pulse width of the input pulse $I(t)$ is estimated from the width of the autocorrelation function $I_A(\tau)$ using Table 11.9, if the pulse shape function is known (or assumed).

Q-Switching

A *Q-switch*, which controls the Q value of a cavity, provides a short and very intense laser pulse. The Q value
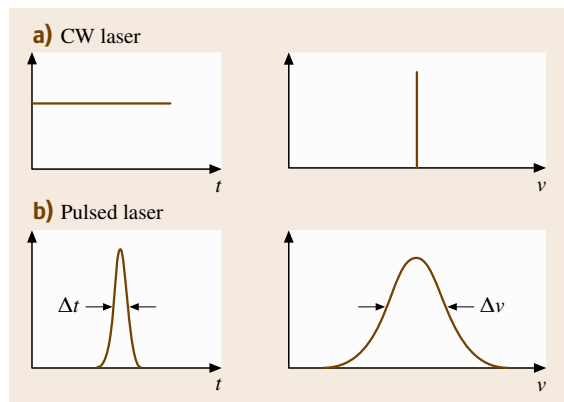

Fig. 11.41a,b Relationship between temporal profile and spectral shape
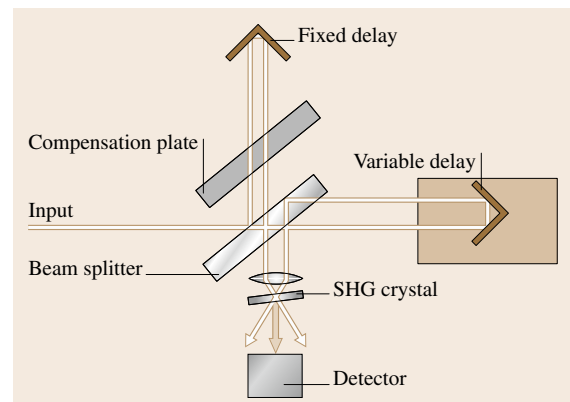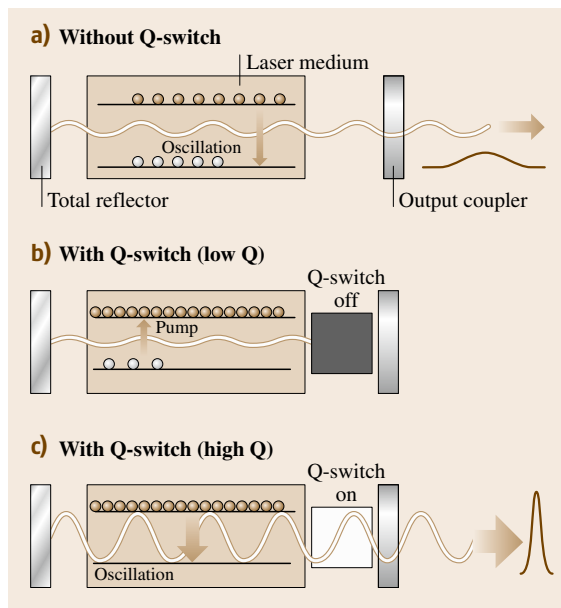

Fig. 11.42 Set-up of auto-correlator

Table 11.9 Calculated results of K, the relation between Δt, τ_A which is the width of the autocorrelation function for typical functions

Pulse shape function	K	$\Delta t/T$	τ_A/T	$\Delta t/\tau_A$
Gaussian: $\exp(-t^2/T^2)$	0.441	$2\sqrt{\ln 2}$	$2\sqrt{2\ln 2}$	0.707
Diffraction function: $\sin c^2(t/T)$	0.886	2.78	3.71	0.751
Hyerbolic square: $\mathrm{sech}^2(t/T)$	0.315	1.76	2.72	0.648
Lorentzian: $[1+(t/T)^2]^{-1}$	0.221	2	4	0.500
One-sided exponential: $\exp(-t/T)\,(T>0)$	0.110	$\ln 2$	$2\ln 2$	0.500

is a measure of how much light from the laser medium is fed back into itself by the cavity resonator. A high Q value corresponds to low resonator losses per round trip. A schematic description of Q-switching is illustrated in Fig. 11.43. Without a Q-switch, the laser delivers pulses with a moderate intensity and pulse width, shown in Fig. 11.43a, according to the pumping condition, e.g. optical pumping with a flash lamp. With the Q-switch (off), initially the laser medium is pumped, while the Q-switch, producing the resonator with low Q, prevents feedback of light into the medium as shown in Fig. 11.43b. This produces population inversion; the amount of energy stored in the laser medium will increase, and finally reach some maximum level, as shown in Fig. 11.44, due to losses from spontaneous emission and other processes. At this point, the Q-switch is quickly changed from low to high Q, allowing feedback

and the process of optical amplification by stimulated emission to begin, as shown in Fig. 11.43c. Because of the large amount of energy already stored in the laser medium, the intensity of light builds up very quickly; this also causes the energy stored in the medium to be exhausted quickly, as seen in Fig. 11.44. The net result is a short pulse with a width of $1-100$ ns, which may have a very high peak intensity. The typical example is a Q-switched Nd:YAG laser, which can deliver 1 MW.

Mode–Locking

If all modes shown in Fig. 11.15 operate with fixed phases among them, the laser output in a simple case is described by

$$E(t) = \sum_{m=-N}^{N} E_0 \exp[\mathrm{i}(\omega_0 + m\Delta\omega)t + m\theta_0] ,$$
$$= E_0 \frac{\sin[(2N+1)(\Delta\omega t + \theta_0)/2]}{\sin[(\Delta\omega t + \theta_0)/2]} \exp(\mathrm{i}\omega_0 t) ,$$

(11.110)

where ω_0 is the center frequency of the laser spectrum, $\Delta\omega = \pi(c/l)$ from (11.60) and we assume that $2N+1$ modes with the same amplitude E_0 exist and that the phase difference between adjacent modes is constant θ_0.

a) Without Q-switch

Laser medium

Oscillation

Total reflector

Output coupler

b) With Q-switch (low Q)

Q-switch off

Pump

c) With Q-switch (high Q)

Q-switch on

Oscillation

Fig. 11.43a–c Schematic illustration of Q-switching

Cavity loss

Cavity gain

Output intensity

100 %

Cavity loss

Cavity gain

0 %
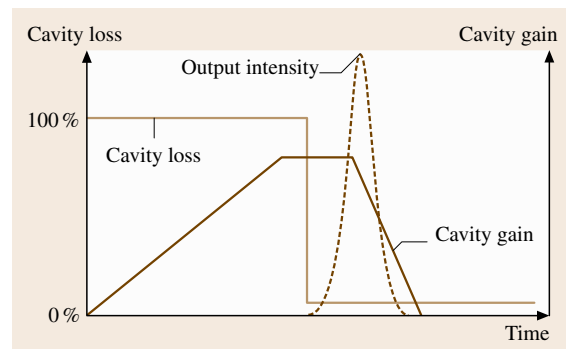
Time

Fig. 11.44 Time evolution of cavity loss caused by the Q-switch, optical gain due to the pumping and laser intensity

The calculated envelope $|E(t)|^2$ is plotted in Fig. 11.45. The time interval between the strong peaks Δt is

$$\Delta t = \frac{2\pi}{\Delta\omega} = \frac{2l}{c} \, , \tag{11.111}$$

which corresponds to the round-trip time of the laser pulse inside the cavity. The pulse width of the peak δt is

$$\delta t = \frac{2\pi}{(2N+1)\Delta\omega} \, . \tag{11.112}$$

This means that a broader spectral width results in a shorter pulse width, as expected from the energy–time uncertainty relation.

Mode-locking is achieved by modulation of the resonator loss synchronized to the round-trip time of the
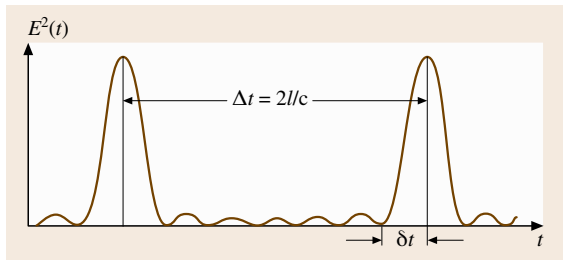
Fig. 11.45 A temporal profile of $|E(t)|^2$ in the case $N = 7$ in (11.105)
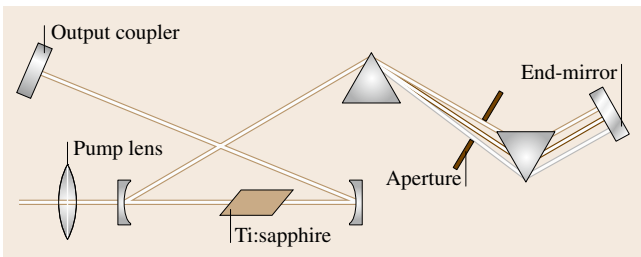
Fig. 11.46 Schematic construction of a mode-locked Ti:sapphire laser
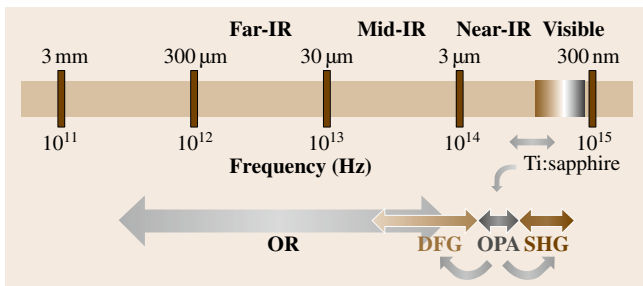
Fig. 11.47 Frequency map covered by the OPA system

laser pulse. There are two types: *active mode-locking* and *passive mode-locking*. The former uses an AOM which acts as a shutter that is open during a certain duration separated by the round-trip time; a typical example is a mode-locked Nd:YAG laser. The most successful method for the passive mode-locking is *Kerr-lens mode-locking* (KLM), which manifests itself in a mode-locked Ti:sapphire laser. KLM is based on the optical Kerr effect of the laser medium, Ti:sapphire itself.

Figure 11.46 shows a schematic configuration of a Ti:sapphire laser. An intense pulse which experiences large refractive index due to the n_2 is focused within the Ti:sapphire rod, so the diameter of the pulse is reduced. Only the intense pulse can pass through the aperture inside the cavity with less loss and be amplified further. The very broad gain spectrum of the Ti:sapphire crystal allows the formation of ultrashort pulses with 10-fs duration. The group velocity dispersion is compensated with the prism pair, which introduces different delays for the different frequency components. The repetition rate of the mode-locked lasers is determined by the cavity length, typically 80 MHz. Generation of more intense pulses is possible by reducing the repetition rate; a *regenerative amplifier* delivers intense pulses with energy of ≈ 1 mJ and repetition frequency of ≈ 1 kHz [11.51]. Such pulses bring a variety of nonlinear phenomena; an *optical parametric amplifier* (OPA) which utilizes parametric process in Sect. 11.4.1 boosts a seed light of white-light continuum and works as a tunable light source. Thus the OPA system with additional frequency converters in Fig. 11.47 pumped with a regenerative amplifier based on a Ti:sapphire oscillator provides tunable light pulses with fs duration from the far-IR to UV region. This is a powerful tool for time-resolved and/or nonlinear spectroscopy.

11.4.3 Time–Resolved Spectroscopy

Time-resolved spectroscopy enables us to obtain the dynamics of electrons, phonons, spins, etc. in the materials in timescales down to femtoseconds. Pulsed lasers introduced in the last section are usually utilized as light sources, while many detection techniques are used depending on the timescale or the repetition rate of events. The techniques for time-resolved spectroscopy are classified into electrical methods with electronic apparatus and optical methods using nonlinear optics. Time-resolved measurements for the luminescence are reviewed in this section.

Electrical Methods

The electric signal from a photosensor, e.g. a PMT or PD (Sect. 11.1.2), is registered with electrical apparatus shown in Table 11.10 (except a streak camera). Their principles are illustrated in Fig. 11.48.

1. A *digital storage oscilloscope* with sample rates higher than 1 GS/s makes it possible to follow the electric signal with a time resolution of nanoseconds [11.52].
2. A *boxcar integrator* stores the signal during a time window whose position and duration (wider than ns) can be set arbitrarily [11.52]. Though temporal profiles can be obtained by sweeping the time window, this apparatus is mainly used for the gating of the temporal signal with a low repetition rate of up to 1 kHz, e.g. in pump-probe experiments using a regenerative amplifier (Sect. 11.4.4).
3. A *time-to-amplitude converter* (TAC) is used with a multichannel analyzer (MCA) to perform *time-correlated single-photon counting* (TCSPC).

A schematic diagram of the TCSPC method is depicted in Fig. 11.49. Here CFD is an abbreviation of *constant fraction discriminator* which discriminates a signal pulse from a noise as follows. The CFD produces an output electric pulse when the input voltage exceeds a preset threshold value; the time delay between the input and output pulses does not depend on the input electric pulse height or shape. Very weak light behaves as a photon, which can be counted as an electric pulse from a PMT or APD. The time interval between the excitation pulse and the luminescence pulse from the sample reflects the decay time statistically; the accumulation of a number of such events reproduces the decay curve. The TAC produces an electronic pulse with a height which is proportional to the time difference between the start pulse triggered by the excitation pulse and the stop pulse from the detector. The MCA receives the electronic pulse from the TAC and converts the voltage into a channel address number of a storage memory. A histogram, which corresponds to the decay curve, is built up in the MCA with increasing numbers of events. The counting rate should be smaller than $\approx 1\%$, so that the probability
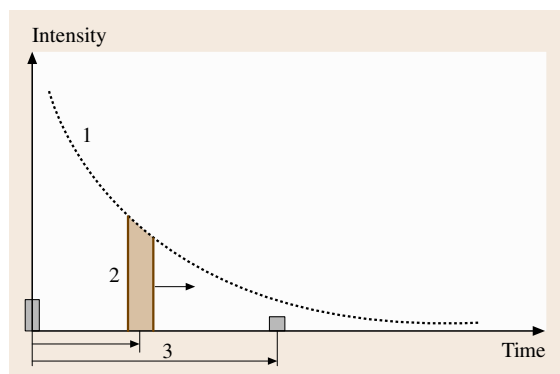
Fig. 11.48 Illustration of the principles for detecting transient electric signals
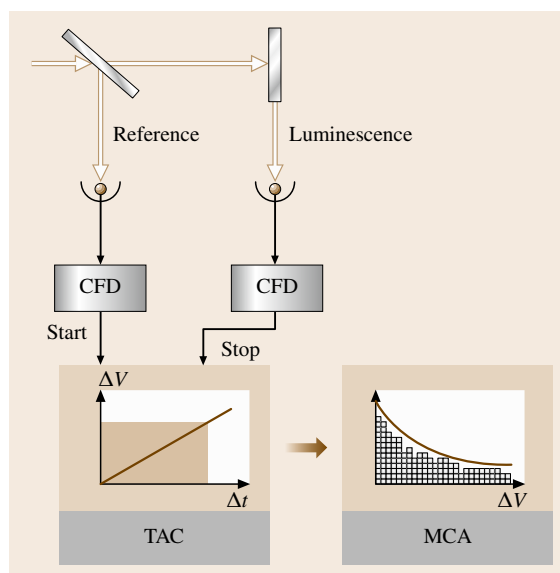
Fig. 11.49 Schematic diagram of the time-correlated single-photon counting method

of a simultaneous arrival of two photons is negligible ($< 0.01\%$). Thus a light source with a high repetition rate, e.g. a mode-locked laser, is required [11.53]. The time resolution of this technique is determined by the jit-

Table 11.10 Comparison between four electric methods

Apparatus	Time resolution	Features
Digital storage oscilloscope	$\approx$ ns	Single-shot or repetitive events
Boxcar integrator	$\approx$ sub-ns	Repetitive events
Time-to-amplitude converter (TAC)	$\approx$ 10 ps	Repetitive events, single photon counting
Streak camera	$\approx$ ps	Single-shot or repetitive events

Part C | 11.4
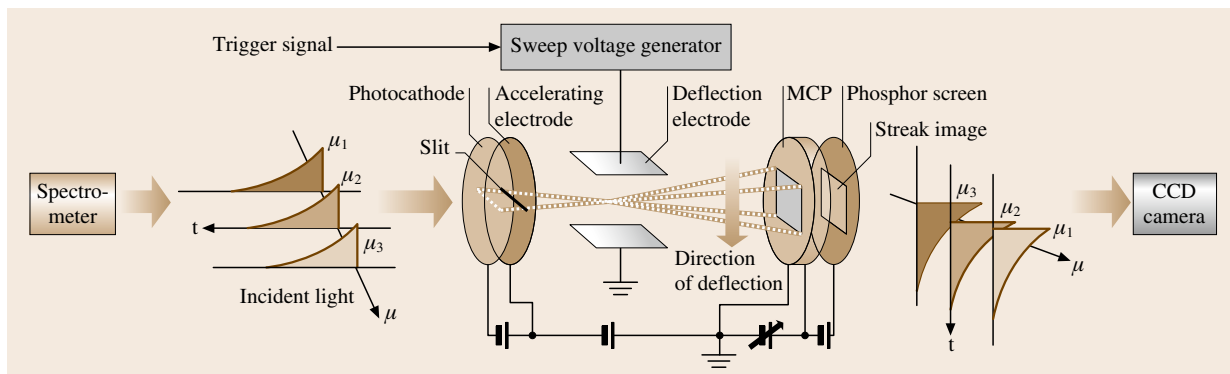
Fig. 11.50 Schematic construction of the streak camera
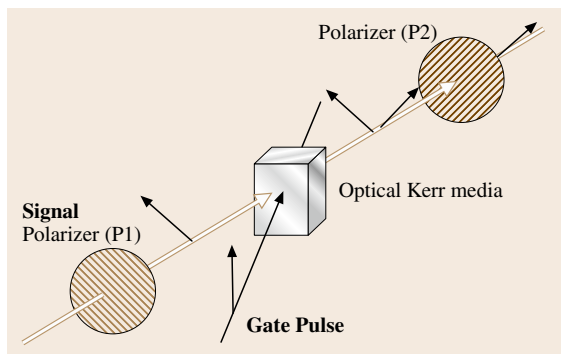
Fig. 11.51 Schematic illustration of the Kerr shutter

ter of the electric circuit, not by the width of the electric signal from the photosensors. Therefore, time resolution of tens of picoseconds can be achieved with a specially designed PMT or APD. Very accurate data can be obtained because of no linearity problems in the detector, but *convolution analysis* is usually required in sub-ns region, because an artifact, called *after-pulse*, due to the photosensors distorts the signal.

A *streak camera* is widely used in time-resolved spectroscopy, because it enables us to obtain temporal and spectral information simultaneously. A schematic construction of the streak camera is illustrated in Fig. 11.50. A spectrometer is usually installed before the streak camera in order to disperse the incoming light horizontally. The spectrally dispersed light impinges on a photocathode from which photoelectrons are emitted. The electrons are accelerated and temporally dispersed by deflection electrodes subjected to a rapidly changing sweep voltage in the vertical direction. Then the spectrally and temporally dispersed electrons hit a *microchannel plate* (MCP) which multiplies electrons while keeping their spatial distribution. The multiplied

electrons irradiate a phosphor screen on which a so-called streak image appears. The image is recorded with a CCD camera. A time-resolved spectrum can be obtained even for a single event, if the incident light is strong. This feature enables us to study a phenomenon which shows substantial shot-by-shot fluctuations [11.54]. Time resolution of 200 fs is achieved in single-shot detection. Usually repetitive events are integrated on a CCD chip. In this case, the electronic jitter of the trigger signal synchronized to the incident light pulse determines the time resolution of the streak camera. A synchroscan streak camera used for mode-locked lasers with high repetition rates of ≈ 100 MHz achieves picosecond time resolution [11.55]. In the case of very weak light, single-photon counting detection is possible using a fast-readout CCD camera, because the MCP has a large multiplication factor.

Optical Methods (Using Nonlinear Optics)

Optical Kerr shutters (OKS) utilize the optical Kerr effect (Sect. 11.4.1); a Kerr-active medium with large $\chi^{(3)}$ works as an optical gate. The schematic configuration of the OKS is depicted in Fig. 11.51. A strong laser pulse induces birefringence in the Kerr medium, so that the plane of the polarization of the incident light determined by a polarizer P1 is rotated. Thus the incident light, normally blocked by a crossed polarizer P2, can pass through the P2. This configuration is inserted between the collection lenses and the spectrometer in Fig. 11.12. The time-resolved spectrum is then obtained by changing the delay between the gate and incident pulses [11.56]. The extinction ratio of the crossed polarizers determines the background of this technique, while the time response of the Kerr medium determines the time resolution of the OKS.
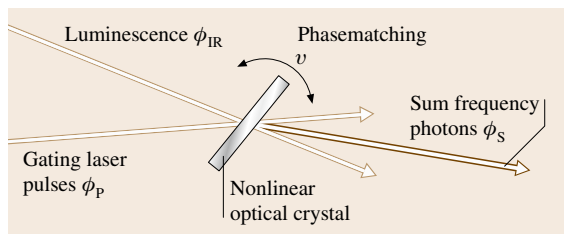
Fig. 11.52 Principle of up-conversion spectroscopy

Table 11.11 Comparison between the Kerr shutter and up-conversion

Method	Time resolution	Features
Kerr shutter	sub-ps	Strong gating pulse is required
Up-conversion	≈ 100 fs	Wavelength scanning is required

Up-conversion spectroscopy is based on SFG (Sect. 11.4.1); the up-converted photon ω_s from IR luminescence ω_{IR} is emitted when the gating laser pulse ω_p irradiates the nonlinear crystal, as shown in Fig. 11.52. A combination of the pump pulse and the nonlinear crystal acts as an optical gate like a boxcar integrator. By sweeping the delay time of the pump pulse, a temporal profile of the luminescence is obtained. A time-resolved spectrum is obtained by scanning the crystal angle (and monochromator) for the phase-matching condition [11.57]. Down-conversion for UV luminescence is also possible.

11.4.4 Nonlinear Spectroscopy

Nonlinear spectroscopy reveals electronic structures, relaxation processes in various materials and provides us rich information on the materials which cannot be supplied by linear spectroscopy. Though the application of nonlinear spectroscopy is very wide, this section focuses on the topics for time-resolved measurements.

Pump–Probe Experiment

In the *pump-probe experiment*, a pump pulse causes the absorption or reflection change of the material, which is observed in a probe pulse. This technique enables us to obtain a temporal evolution of an optical response of the material with ultrafast time resolution (shorter than 10 fs) by sweeping the time delay between pump and probe pulses. A schematic experimental set-up is shown in Fig. 11.53. Two laser beams are focused on the same spot of the sample. A delay line with vari-
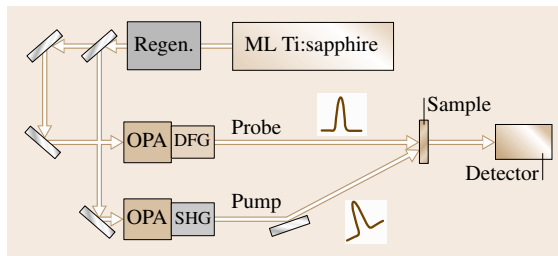
Fig. 11.53 Typical experimental set-up for the pump–probe transmission measurement. ML: mode-locked laser; Regen.: regenerative amplifier

able length is used to change the optical path difference between pump and probe paths. In the case of transmission pump-probe measurement, differential transmission change is defined as

$$\frac{\Delta T}{T} = \frac{I_{on} - I_{off}}{I_{off}} , \qquad (11.113)$$

where I_{on} and I_{off} are the intensities of the probe pulses passing through the sample with and without the pump pulse, respectively. Pump-induced absorption change $\Delta\alpha$ is expressed by

$$\Delta\alpha l = \ln\left(1 + \frac{\Delta T}{T}\right) , \qquad (11.114)$$

where l is the sample thickness.

By scanning the probe frequency the spectrum of the absorption change can be obtained. A combination of white-light continuum in Sect. 11.4.1, which is available in the visible region, as a probe pulse and an array detector reduces the acquisition time remarkably. In this case, the frequency chirp of the white-light continuum should be corrected.

Transient Absorption and Two–Photon Absorption

A schematic diagram for transient absorption is illustrated in Fig. 11.54. If nonradiative processes is dominant and luminescence cannot be observed, the transient absorption measurement provides decay process of the excited state $|e_1\rangle$. In addition, the higher excited state $|e_2\rangle$, which cannot be observed in the linear (one-photon) absorption, may be found in the transient absorption. Here materials with inversion symmetry have a selection rule

$$\langle g|r|e_1\rangle \neq 0, \ \langle e_1|r|e_2\rangle \neq 0, \ \langle g|r|e_2\rangle = 0 , \quad (11.115)$$

if $|g\rangle$ and $|e_2\rangle$ are even, $|e_1\rangle$ is odd. Absorption decrease called *bleaching*, corresponding to a negative signal of
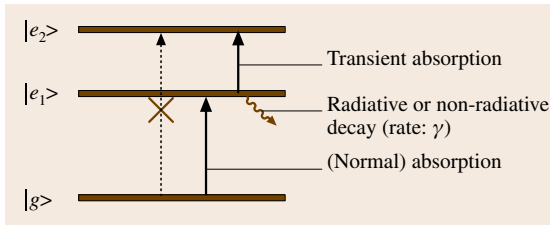
Fig. 11.54 Schematic diagram for transient absorption
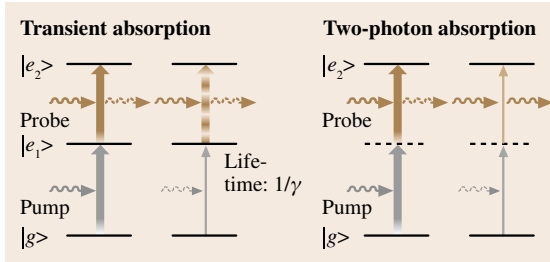
Fig. 11.55 Comparison between transient absorption and two-photon absorption
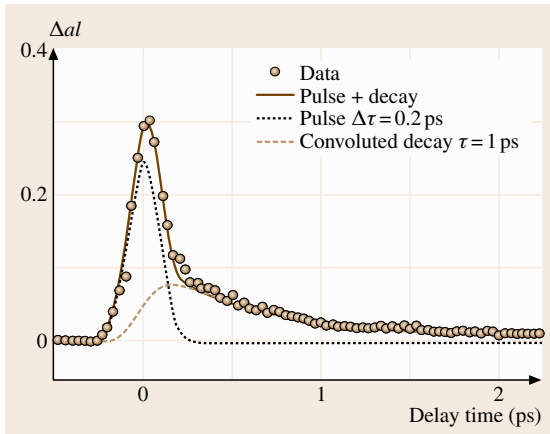
Fig. 11.56 Typical example of the absorption change

Fig. 11.57 (a) Schematic illustration of Z-scan measurement, and **(b)** normalized transmission against z

$\Delta\alpha l$, shows population decrease in the ground state $|g\rangle$. This signal reflects a process of ground-state recovery.

The transient absorption shows an exponential decay profile, while *two-photon absorption* (TPA) in which pump and probe pulses absorbed simultaneously results in an instantaneous response following the temporal profile of the pump pulse, as illustrated in Fig. 11.55. The TPA reveals hidden electronic levels which are not detectable in linear spectroscopy.

Example of Pump–Probe Measurement

A typical example of the absorption change is shown in Fig. 11.56 [11.58]. The signal consists of two components: a Gaussian pulse with 0.2-ps width which is determined by the pulse duration of the laser and an exponential decay with decay constant $\tau = 1$ ps. The former is caused by the TPA. Changing the pump and probe frequencies, we can obtain a TPA spectrum directly [11.59]. The latter arises from the transient absorption from the excited state $|e_1\rangle$ to the higher excited state $|e_2\rangle$ in Fig. 11.55. Its decay constant reflects the decay time of the excited state $|e_1\rangle$. It is noted that convolution analysis is required in this case in which the decay time is comparable to the pulse duration. Here we calculated a convolution of Gaussian shape with 0.2-ps width and a single exponential decay with a 1-ps decay constant, shown in the figure by a broken line.

Z-scan

This simple technique allows us to measure both the sign and magnitude of the nonlinear refractive index n_2. A schematic set-up is shown in Fig. 11.57. A laser beam with a Gaussian spatial beam profile is focused at $z = 0$ and the sample position is varied. The intensity transmitted through the aperture is measured as a function of the sample position z shown in Fig. 11.57b. Here the sample acts as a lens whose focal length depends on the position z. Numerical calculation shows [11.60]

$$\Delta T \approx 0.4\Delta\Phi , \tag{11.116}$$

where (11.102) is used. Thus we can obtain n_2 directly.

Four-Wave Mixing

There are many variations of four-wave mixing (FWM) with two or three beams, which have the same frequency (degenerate) or different frequencies (nondegenerate). This phenomenon is based on the interference between several beams inside the material [11.61]. FWM spectroscopy generally provides information on
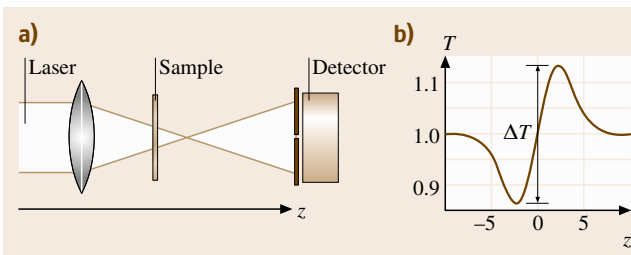
coherent processes in the excited states. This technique is also used to estimate the value of $\chi^{(3)}$.

11.4.5 Terahertz Time–Domain Spectroscopy

As a unique application of ultrashort pulsed lasers, terahertz (THz) time-domain spectroscopy (TDS) is introduced in this section. The THz region is located between microwave radiation and infrared light. Due to the lack of a suitable light source and detector, spectroscopy in this region was difficult and tedious. After the development of the mode-locked Ti:sapphire laser, THz TDS is intensively applied to many materials, e.g. doped semiconductors, superconductors, biomaterials [11.62]. The TDS enables us to obtain a waveform of the THz electric field $E(t)$ itself, not $|E(t)|^2$ as in conventional spectroscopy. This provides us a lot of advantages, e.g. simultaneous determination of real and imaginary parts of the dielectric function.

A schematic illustration of the generation and detection method for a THz pulse using a photoconductive antenna is depicted in Fig. 11.58 [11.63]. The antenna structure is fabricated on a substrate of semi-insulating semiconductors, e.g. low-temperature grown (LT)-GaAs. As an emitter, the antenna is subjected to a DC voltage and irradiated with a femtosecond laser around the gap between the dipoles, as illustrated in Fig. 11.58a. Then the mono-cycle THz pulse $E(t)$ is emitted according to the simple formula

$$E(t) \propto \frac{\partial j_e}{\partial t} , \qquad (11.117)$$

where j_e is the surge current due to photocarriers created by the irradiation of the laser pulse. Over 30 THz generation has been reported by using 15-fs pulses. The alternative method is OR (Sect. 11.4.1) of ultrashort pulses; generation of ultra-broadband infrared pulse beyond 100 THz by using 10-fs pulses and GaSe crystals has also been demonstrated [11.64].

The antenna is also used as a receiver; photocarriers created by the pulse irradiation provide a transient current $j_d(t)$ which is proportional to the instantaneous THz electric field $E(\tau)$ as follows:

$$j_d(t) \propto \int E(\tau)N(t-\tau)\mathrm{d}\tau , \qquad (11.118)$$

where $N(t)$ is the number of photocarriers created by the laser pulse. If the pulse duration and the decay time of the $N(t)$ is negligibly short, $N(t) = N_0\delta(t)$, then

$$j_d(t) \propto E(t) . \qquad (11.119)$$

Thus the THz electric field can be reproduced by sweeping the time delay between the laser pulse and the THz
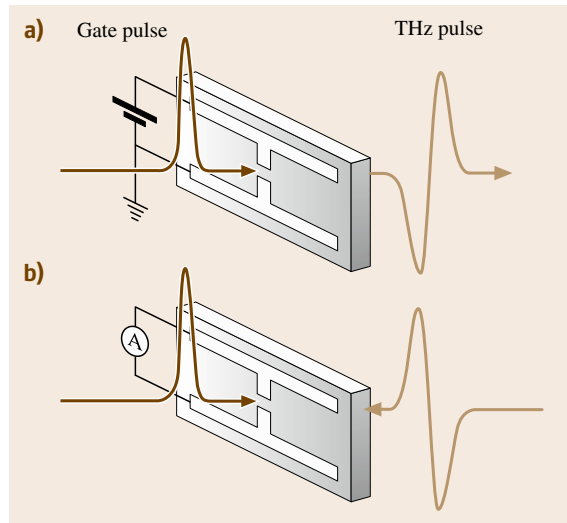
Fig. 11.58a,b Schematic illustration of (**a**) the generation and (**b**) the detection method for THz time-domian spectroscopy
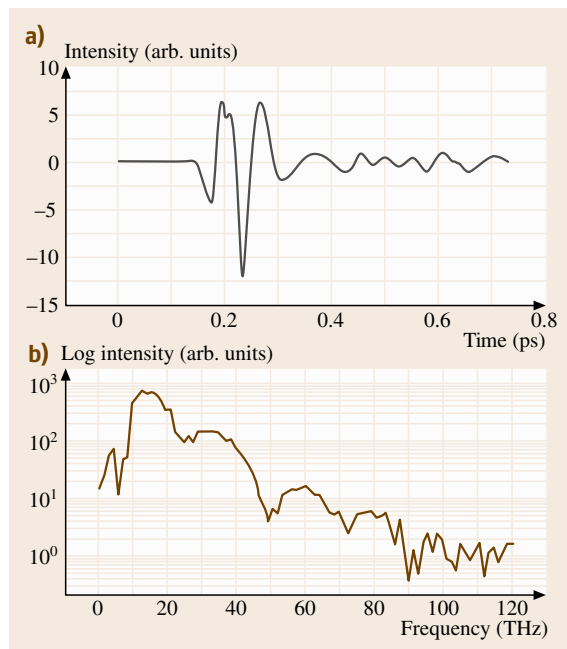
Fig. 11.59 (**a**) Temporal waveform of ultra-broadband THz radiation detected with a PC antenna. (**b**) Fourier-transformed electric-field spectrum of (**a**)

pulse. Figure 11.59a shows a typical example of temporal waveform of the ultra-broadband THz emission by OR with a 10-fs laser and a thin GaSe crystal detected
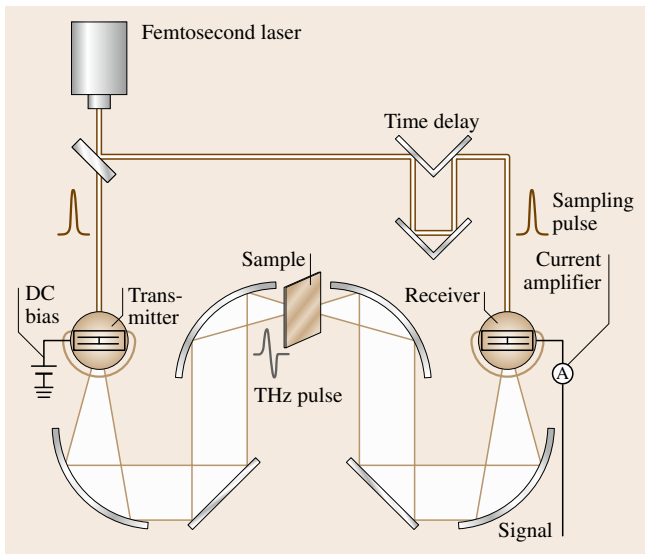
Fig. 11.60 Experimental set-up for THz TDS

with a PC antenna [11.65]. Its Fourier-transformed spectrum is also shown in Fig. 11.59b. The high-frequency region beyond 80 THz is detectable using a PC antenna. The alternative method is to use electrooptic sam-

pling, which achieves ultra-broad-band detection beyond 120 THz [11.66].

An experimental set-up is shown in Fig. 11.60. Parabolic mirrors are used for focusing light in the far- and mid-IR region.

The complex Fourier transformation of $E(t)$ is defined by

$$E(\omega) = \frac{1}{2\pi} \int E(t) \exp(-i\omega t)\, dt. \qquad (11.120)$$

In the transmission measurement, the complex refractive index $\boldsymbol{n}$ can be obtained using

$$\frac{E(\omega)}{E_0(\omega)} = \exp\left\{ -i[\boldsymbol{n}(\omega) - 1]\frac{L\omega}{c} \right\}, \qquad (11.121)$$

where L is the sample thickness and $E(\omega)$ and $E_0(\omega)$ are Fourier transformations of the transmitted and incident waveform, respectively. Thus the real and imaginary parts are determined simultaneously without complex analyses such as the Kramers–Kronig transformation or the ellipsometry introduced in Sect. 11.1.4.

THz waves penetrate dry materials such as paper, ceramics and plastics but are strongly absorbed in water. Recently *terahertz imaging* has been used for drug detection, luggage inspection and integrated circuit inspection [11.67].

11.5 Fiber Optics

Optical fiber technology has developed rapidly during the last 30 years under the demands of the telecommunication network. Today a variety of commercial and laboratory applications of fiber optics are going on because of the excellent properties of optical fiber, e.g. flexibility and compactness. This section summarizes the unique properties of fibers and their characterization methods.

In its simplest form an optical fiber consists of a central glass core surrounded by a cladding layer whose refractive index n_1 is lower than the core index n_0.

Figure 11.61 shows schematically the cross section and path of a ray propagating via total internal reflection in a step-index fiber. The critical angle for the total internal reflection at the interface is expressed as

$$\theta_c = \sin^{-1}\left(\frac{n_1}{n_0} \right)$$

The fiber numerical aperture (NA), which is defined as the sine of the half-angle of acceptance, is given by

$$\text{NA} = \sin(\theta_{\max}) = \sqrt{n_0^2 - n_1^2} \,.$$

Two parameters that characterize the step-index fiber are the normalized core–cladding index difference

$$\Delta = \frac{n_0 - n_1}{n_1}$$

and the so-called V parameter defined as

$$V = \frac{2\pi a}{\lambda} \sqrt{n_0^2 - n_1^2} \,,$$

where a is the radius of core and λ is the wavelength of light.

The V parameter determines the number of modes supported by the fiber. A step-index fiber supports a single mode if $V < 2.405$. Fibers with a value of V greater than this are multimodal. More sophisticated index profiles were developed to modify the mode profile and dispersion. Detailed analysis of fiber modes in various structures is described in the textbook [11.68].

A common material for optical fiber is silica glass synthesized by chemical vapor deposition. The refractive index difference between the core and cladding is introduced by selective doping during the fabrication process. Dopants such as GeO_2 and P_2O_5 increase the
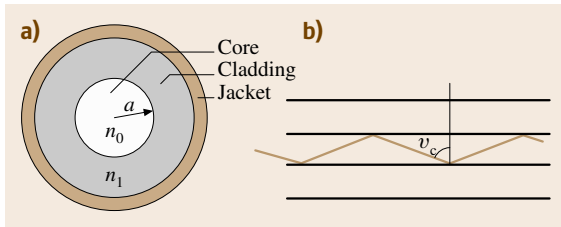
Fig. 11.61a,b Cross section of a step-index fiber (**a**) and the path of a ray propagating via total internal reflection (**b**)

refractive index of silica and are used for the core, while materials such as boron and fluorine decrease the refractive index of silica and are used for the cladding.

The fabrication process for optical fibers involves two stages: the formation of a preform and drawing into a fiber. A cylindrical preform with the desired index profile and relative core-cladding dimensions is fabricated through chemical vapor deposition. The preform is then drawn into a fiber using a precision-feed mechanism into a furnace. The fabrication methods for optical fibers are described in [11.69].

11.5.1 Fiber Dispersion and Attenuation

Chromatic dispersion and attenuation of the optical signal are the most important fiber parameters for telecommunications.

Optical Attenuation in Fibers

If P_i is the incident power introduced into a fiber of length L, the transmitted power P_t is expressed by

$$P_t = P_i \exp(-\alpha L) ,$$

where α is the conventional attenuation constant. Customarily, α is expressed in the unit of dB/km using the following definition.

$$\alpha_{dB} = -\frac{10}{L} \log\left(\frac{P_t}{P_i}\right) .$$

There are three principal attenuation mechanisms in fibers: absorption, scattering and radiative loss. Radiation losses are generally kept small enough by using thick cladding.

Figure 11.62 shows the measured loss spectrum of a typical low-loss silica fiber [11.69]. Silica suffers from absorption due to electronic transitions in the ultraviolet region below 170 nm and absorption due to vibrational transitions in the infrared beyond 2 μm, but is highly transparent in the visible and near-infrared. In this region the fundamental attenuation mechanism is
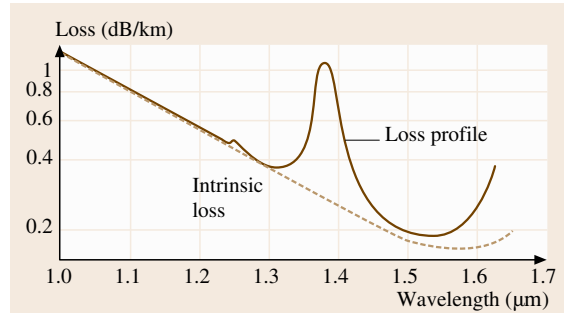
Fig. 11.62 Measured loss spectrum of a single-mode silica fiber. The *dashed curve* shows the contribution resulting from Rayleigh scattering (after [11.69])

Rayleigh scattering due to the irregular glass structure. Intrinsic losses in silica fiber due to Rayleigh scattering is estimated to be

$$\alpha_R = \frac{C_R}{\lambda^4} ,$$

where the constant C_R is in the range 0.7–0.9 dB/ km μm^4 depending on the constituents of the fiber core. Typical losses in modern fibers is around 0.2 dB/km near 1.55 μm. Conventional silica fiber has absorption peaks at 1.4, 2.2 and 2.7 μm due to OH vibration modes and these absorption peaks are sensitive to water contamination.

Attenuation Measurement

There are two general methods for the measurement of fiber loss; the cut-back method and optical time-domain reflectometry (OTDR). In any scheme special attention must be paid to uncertainty arising from the source-to-fiber coupling. The cut-back method is a destructive evaluation which neatly avoids the difficulty [11.70]. It operates in the following way.

- Couple the light from the source into a long length of fiber.
- Measure the light output with a large-area detector.
- Cut the fiber back by a known length and measure the change in the light output.

The change in the output is considered to arise from the attenuation in the cut fiber.

In the case of a single-mode fiber, the fiber may be cut back to a relatively short length (several meters) where the cladding modes are effectively removed. However, if the higher mode is near or just beyond the cut-off, we may need a sufficiently long length of
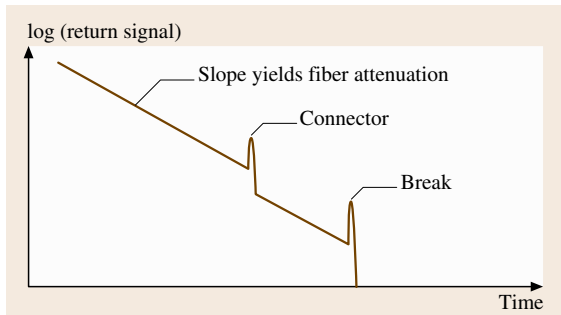
Fig. 11.63 Typical OTDR signal. OTDR can be used for attenuation measurement, splice and connector loss

fiber to strip off the unfavorable lossy modes [11.71]. In the case of multimode fiber the situation becomes more delicate because the attenuation depends on the modes, i.e. higher-order modes have higher losses. So, we should try to excite modes evenly and wait until the mode equilibrium is established through mode conversion. This may need a considerable length of fiber, typically ≈ 1 km.

Nondestructive loss measurement has now become possible with the technological advancement of low-loss single-mode splices or connectors, simply by assuring that the connector loss is much smaller than the fiber loss.

Optical time-domain reflectometry (OTDR) is another nondestructive evaluation method for attenuation. In this method the fiber is excited with a narrow laser pulse and a continuous backscattering signal from the fiber is recorded as a function of time. Assuming a linear and homogeneous backscattering process the decrease in backscattered light with time reflects the round-trip attenuation as a function of distance.

Figure 11.63 shows a typical OTDR signal. The linear slope yields the fiber attenuation and the sudden drop in intensity represents the splice loss; the narrow peak indicates a reflection. The OTDR method enables the evaluation of the loss distribution along the fiber including splice loss even in the deployed fiber. OTDR is also very sensitive to the excitation condition into the fiber, so control of the launch condition is the key for all attenuation measurement of fibers.

Chromatic Dispersion

The refractive index of every material depends on the optical frequency; this property is referred to as chromatic dispersion. In the spectral region far from absorption the index is well-approximated by the Sellmeier equation. For bulk fused silica $n(\lambda)$ is expressed

by the equation,

$$n(\omega)^2 = 1 + \sum_{j=1}^{m} \frac{B_j \omega_j^2}{\omega_j^2 - \omega^2} \,,$$

where ω_j is the resonance frequency and B_j is the strength of the jth resonance. For bulk fused silica, these parameters are found to be $B_1 = 0.6961663$, $B_2 = 0.4079426$ and $B_3 = 0.8974794$, $\lambda_1 = 0.0684043 \,\mu\text{m}$, $\lambda_2 = 0.1162414 \,\mu\text{m}$, and $\lambda_3 = 9.896161 \,\mu\text{m}$ [11.72], where $\lambda_j = 2\pi c/\omega_j$ and c is the speed of light.

Dispersion plays a critical role in the propagation of short optical pulses because the different spectral components propagate with different speeds, given by $c/n(\omega)$. This causes dispersion-induced pulse broadening, which is detrimental for optical communication systems. The effect of chromatic dispersion can be analyzed by expanding the propagation constant β in a Taylor series around the optical frequency ω_0 on which the pulse spectrum is centered.

$$\beta(\omega) = n(\omega)\frac{\omega}{c} = \beta_0 + \beta_1(\omega - \omega_0)$$
$$+ \frac{1}{2}\beta_2(\omega - \omega_0^2) + \cdots \,,$$

where

$$\beta_m = \left(\frac{\mathrm{d}^m \beta}{\mathrm{d}\omega^m} \right)_{\omega=\omega_0} \quad (m = 0, 1, 2, 3, \ldots) \,.$$

The parameter β_1 and β_2 are related to the refractive index n through the relations

$$\beta_1 = \frac{1}{v_g} = \frac{1}{c}\left(n + \omega \frac{\mathrm{d}n}{\mathrm{d}\omega} \right) \,,$$
$$\beta_2 = \frac{1}{c}\left(2\frac{\mathrm{d}n}{\mathrm{d}\omega} + \omega \frac{\mathrm{d}^2 n}{\mathrm{d}\omega^2} \right) \,,$$

where v_g is the group velocity. The envelope of the optical pulse moves at the group velocity. The parameter β_2, which is a measure of the dispersion of group velocity, is responsible for the pulse broadening. This phenomenon is known as group velocity dispersion (GVD). In bulk fused silica, the GVD parameter β_2 decreases with increasing wavelength, vanishes for wavelengths of about $1.27 \,\mu\text{m}$ and becomes negative for longer wavelengths. This wavelength is referred to as the zero-dispersion wavelength, denoted by λ_D.

The dispersion behavior of actual silica fiber deviates from the bulk fused silica case for the following two reasons. First, the fiber core usually has small
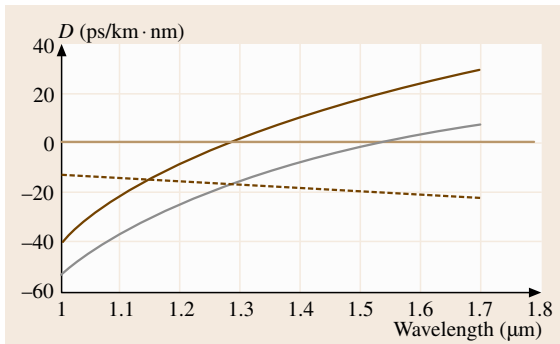
Fig. 11.64 Wavelength dependence of the dispersion parameter D for dispersion-shifted fiber (*brown line*). *Brown curve* and *dotted line* represent D for silica bulk material and wave-guide dispersion, respectively

amounts of dopants such as GeO_2 and P_2O_5. In this case, we should use the Sellmeier equation with parameters appropriate to the amount of doping [11.73]. Second, because of dielectric waveguiding, the effective mode index reflects the field distribution in the core and cladding and is slightly lower than the material index $n(\omega)$ of the core. The field distribution itself depends on ω, and this results in what is commonly termed waveguide dispersion [11.74]. Waveguide dispersion is relatively small except near the zero-dispersion wavelength λ_D, so the main effect of the waveguide contribution is to shift λ_D toward longer wavelengths; $\lambda_D = 1.31\,\mu\text{m}$ for standard single-mode fiber.

The dispersion parameter D (ps/km $\cdot$ nm) is commonly used in fiber optic literature in place of β_2. D is related to β_2 by the relation.

$$D = \frac{d\beta_1}{d\lambda} = -\frac{2\pi c}{\lambda^2}\beta_2 \approx \frac{\lambda}{c}\frac{d^2 n}{d\lambda^2}$$

An important aspect of waveguide dispersion is that the contribution to D depends on design parameters such as the core radius a and the core–cladding index difference Δ. As shown in Fig. 11.64 this feature was used to shift the zero-dispersion wavelength λ_D in the vicinity of 1.55 mm where the fiber loss is at its minimum [11.74]. Such dispersion-shifted fibers, called zero- and nonzero-dispersion shifted fibers, depending on whether $D = 0$ at $1.55\,\mu\text{m}$ or not, play an important role in optical communication network systems.

Dispersion Measurements
Optical pulse method is a simple time-domain measurement. Pulse delay through an optical fiber is directly measured as a function of wavelength [11.75]. This

system usually consists of a fast optical pulse generator with a tunable laser source and a fast waveform monitor system, which are common to instruments characterizing optical transmission lines. However, the accuracy is limited by optical pulse distortion due to dispersion and the time resolution of the waveform monitor.

Phase shift method is the prevailing method because higher time-domain resolution can be obtained with a relatively low frequency modulation (< 3 GHz) [11.76]. The measurement scheme is shown in Fig. 11.65.

A tunable light source like an external cavity laser is usually used as the light source. The light is modulated by a sinusoidal wave at a frequency of f_m with a $LiNbO_3$ Mach–Zender modulator. The optical signal propagated through a test fiber is converted to an electrical signal and then compared with the reference signal using a phase comparator. The phase difference $\phi(\lambda)$ is measured as a function of the wavelength λ. The group velocity delay $\tau(\lambda)$ (s/km) for an optical fiber of length L (km) is obtained by the equation

$$\tau(\lambda) = \frac{\phi(\lambda)}{f_m L},$$

where $\tau(\lambda)$ is supposed to be approximated by a three-term Sellmeier equation

$$\tau(\lambda) = A\lambda^2 + B + \frac{C}{\lambda^2}.$$

Usually, the A, B and C parameters are determined from the delay data and the GVD value is then obtained by differentiating the curve with respect to λ.
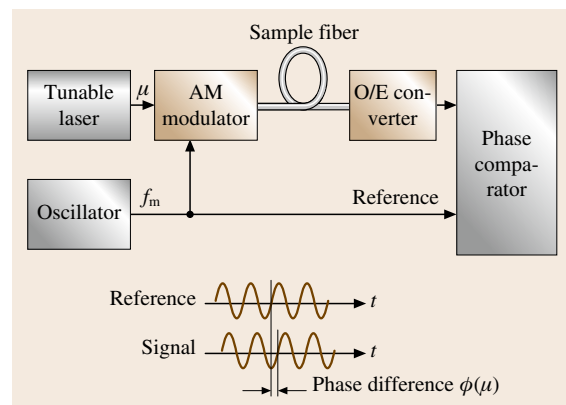
Fig. 11.65 Diagram for dispersion measurement by the phase-shift method
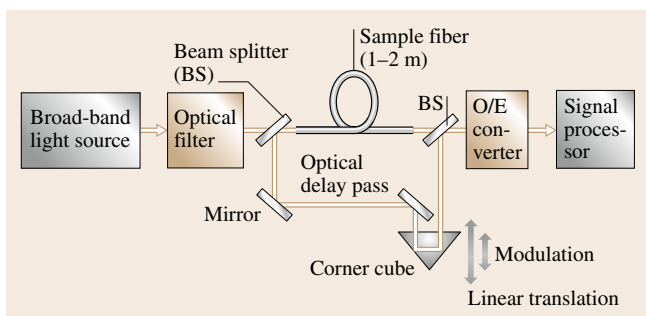
Fig. 11.66 Measurement scheme for the interference measurement method

Interference measurement method is appropriate for short fiber lengths, and allows a detailed and direct comparison of the optical phase shifts between a test fiber and a reference arm. This measurement scheme is illustrated in Fig. 11.66 [11.77].

A broadband light source like white light or an LED is used as the light source in order to reduce the coherence length. Typically, a tunable optical filter with a bandwidth of around 10 nm is introduced in front of the interferometer. A free-space delay line or optical fiber of which the GVD is well-known is utilized as the reference arm. By moving the modulated corner cube, the position d corresponding to the zero-pass interference peak is detected. The group velocity delay $\tau(\lambda)$ for the test fiber is expressed by

$$\tau(\lambda) = \frac{2(d - d_0)}{c} ,$$

where d_0 is the zero-pass difference position at the reference wavelength and c is the velocity of light. The GVD is also estimated by differentiating the smoothed $\tau(\lambda)$ curve with respect to λ.

11.5.2 Nonlinear Optical Properties

This subsection deals with the nonlinear optical properties of fiber. The low loss and long interaction length of optical fibers make nonlinear processes significant. Stimulated Raman and Brillouin scattering limits the power-handling ability of fibers. Four-wave mixing presents an important limit on the channel capacity in wavelength division multiplexing (WDM) systems. Soliton formation and nonlinear polarization evolution are also summarized.

The small cross section and long interaction length of optical fiber make nonlinear optical process significant even at modest power levels. Recent developments

in fiber amplifiers have increased the available power level drastically. Optical nonlinearities are usually detrimental to optical communication networks and put some limits on the power-handling ability of fibers in medical and industrial applications. On the other hand, these optical nonlinearities are utilized in the generation of ultra-short pulse, soliton-based signal transmission, and Raman amplifiers.

As SiO_2 is a symmetric molecule, the second-order nonlinear susceptibility $\chi^{(2)}$ vanishes for silica glasses. So, nonlinear effects in optical fibers originate from the third-order susceptibility $\chi^{(3)}$, which is responsible for phenomena such as third-harmonic generation, four-wave mixing and nonlinear refraction.

In the simplest form, the refractive index can be written as

$$n(\omega, I) = n(\omega) + n_2 I .$$

Self-phase modulation (SPM) is the most important phenomena among the various nonlinear effects arising from the intensity dependence of the refractive index. The self-induced phase shift experienced by an optical field during its propagation is

$$\phi = (n + n_2 I)k_0 L ,$$

where $k_0 = 2\pi/\lambda$ and L is the length of the fiber.

The measured n_2 value for bulk silica at $1.06\,\mu m$ is $2.7 \times 10^{-20}\,m^2/W$ [11.78]. Measured values for various silica optical fibers are found to be in the range $2.2 - 3.9 \times 10^{-20}\,m^2/W$ [11.79]. The scatter of the data may be partly ascribed to the difference of the doping in the core materials of the fibers.

Pulse Compression and Solitons

Figure 11.67 illustrates what happens to an optical pulse which propagates in a nonlinear optical medium. The local index change raises so-called self-phase modulation. Since n_2 is positive, the leading edge of the pulse produces a local increase in refractive index. This results in a red shift in the spontaneous frequency. On the other hand, the pulse experiences a blue shift on the trailing edge.

If the fiber has a normal dispersion at the central wavelength of the optical pulse, the red-shifted edge will advance and the blue-shifted trailing edge will retard, resulting in pulse spreading in addition to the normal chromatic dispersion. However, if fiber exhibits anomalous dispersion, the red-shifted edge will retard and the optical pulse will be compressed. Near the dispersion minimum, the optical pulse is stabilized and

propagates without changing shape at a critical shape. This optical pulse is called a soliton [11.80]. A soliton requires a certain power level in order to maintain the necessary index change. The record for soliton transmission is now well over 10 000 km, which was achieved by utilizing the gain section of a stimulated Raman amplifier or a rare-earth-doped fiber amplifier. In the laboratory, optical fiber nonlinearity is used in the mode-locked femtosecond laser [11.81, 82] and the generation of white continuum [11.83].

Third-harmonic generation and the four-wave mixing effect are based on the same $\chi^{(3)}$ nonlinearity but they are not efficient in optical fibers because of the difficulty in achieving the phase-matching condition. However, WDM signal transmission systems encounter serious cross-talk problems arising from four-wave mixing between the WDM channels near the zero-dispersion wavelength of 1.55 μm [11.85].

The nonlinear optical effects governed by the third-order susceptibility are elastic, so no energy is exchanged between the electromagnetic field and the medium. Another type of nonlinear effect results from stimulated inelastic scattering, in which the optical field transfers part of its energy to the nonlinear medium. Two such scattering process are important in optical fiber: 1) stimulated Raman scattering (SRS), and 2) stimulated Brillouin scattering (SBS).

The main difference between the two is the phonon participating in the process; optical phonons participate in SRS while acoustic phonons participate in SBS. In optical fiber SBS occurs only in the backward direction while SRS can occur in both directions. The equation governing the growth of the Raman-shifted mode is as follows

$$\frac{\mathrm{d}I_S}{\mathrm{d}z} = \frac{g_R}{a_{\mathrm{eff}}} I_P - \alpha I_S \,,$$

where I_S is the Stokes intensity, I_P is the pump intensity and a_{eff} is the effective area of the modes. g_R is Raman gain coefficient. The same equation holds for SBS by replacing g_R with the Brillouin gain coefficient g_B. The Raman gain spectrum in fused silica is shown in Fig. 11.68.

The Raman gain spectrum of silica fiber is broad, extending up to 30 THz [11.84] and the peak gain $g_R = 10^{-13}$ m/W occurs for a Stokes shift of ≈ 13 THz for a pump wavelength near 1.5 μm. In contrast to Raman scattering, Brillouin gain is extremely narrow with a bandwidth < 100 MHz and the Stokes shift is ≈ 1 GHz close to 1.5 μm.
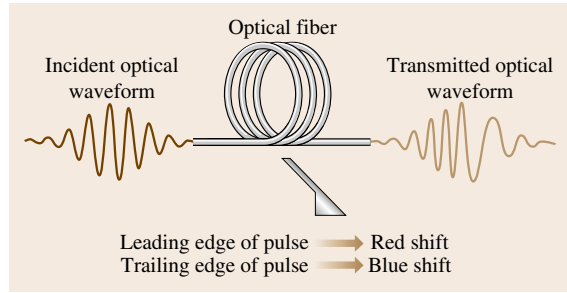
Fig. 11.67 Pulse evolution in a nonlinear medium
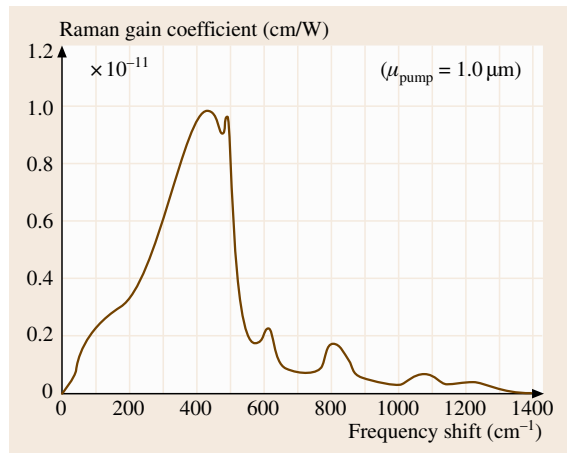
Fig. 11.68 Raman gain spectrum in fused silica (after [11.84])

SRS and SBS exhibit a threshold-like behavior against pump power. Significant conversion of pump energy to Stokes radiation occurs only when the pump intensity exceeds a certain threshold level. For SRS in a single mode fiber with $\alpha L \gg 1$, the threshold pump intensity is given by [11.86]

$$I_P^{\mathrm{th}} = 16\alpha \frac{a_{\mathrm{eff}}}{g_R} \,.$$

SRS can be observed at a power level of ≈ 1 W. Similarly, the threshold pump intensity for SBS is given by [11.86]

$$I_P^{\mathrm{th}} = 21\alpha \frac{a_{\mathrm{eff}}}{g_R} \,.$$

The Brillouin gain coefficient $g_B = 6 \times 10^{-11}$ m/W and is larger by three orders of magnitude compared with g_R. So, SBR threshold is ≈ 1 mW for CW narrow-bandwidth pumping.

Silica fibers with large effective cross section and short length have a significantly higher power-handling
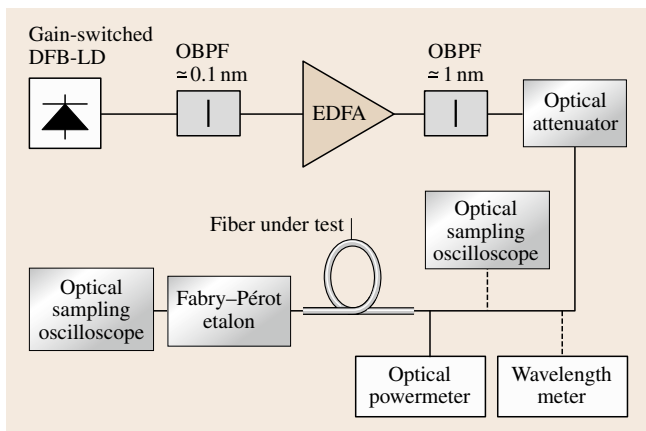
Fig. 11.69 Schematic diagram of the measurement of optical nonlinearity of fiber based on the self-phase modulation method

ability and the broad-spectrum operation helps to increase the power-handling ability of the fiber.

Measurement of Nonlinear Refractive Index n_2

The nonlinear refractive index is expressed by the equation,

$$n(\omega, E^2) = n(\omega) + n_2 E^2 \,,$$

In order to characterize the nonlinearity of the fiber, it is more practical to use the following equation.

$$n(\omega, P) = n(\omega) + \frac{n_2}{A_{\text{eff}}} P$$

where P is the power propagating in the fiber and A_{eff} is the effective area of fiber defined by the equation, [11.80]

$$A_{\text{eff}} = \frac{2\pi \left[\int_0^\infty |E(r)|^2 \, r \, \mathrm{d}r \right]}{\int_0^\infty |E(r)^4| r \, \mathrm{d}r} \,,$$

where $E(r)$ presents the field distribution in the fiber; A_{eff} is approximately related to the mode field diameter (MFD) by the following equation

$$A_{\text{eff}} \approx \pi \left(\frac{\text{MFD}}{2} \right)^2 \,.$$

For reliable evaluation of the nonlinearity of fiber, a variety of methods have been developed based on self-phase modulation [11.87–89], cross-phase modulation [11.90], four-wave mixing [11.91] and interferometry.

Figure 11.69 shows a measuring system based on self-phase modulation developed by *Namihira* et al. [11.87]. The output of a gain-switched DFB-LD with
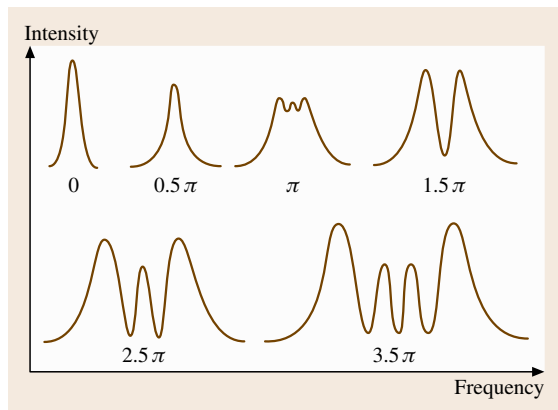
Fig. 11.70 Spectral evolution due to the self-phase modulation as a function of incident power (after [11.87])

a pulse width of 26.5 ps is filtered by a narrow-band filter with a bandwidth of 0.1 nm to get a nearly transformation-limited beam. The beam is amplified by an Er-doped fiber amplifier (EDFA), and is introduced into a test fiber through a variable optical attenuator. The optical spectra of the fiber output are measured by a Fabry–Pérot interferometer. The observed output spectra from the fiber for various input powers is shown in Fig. 11.70 [11.87]. The number of observed spectral peaks M is related to the maximum phase shift, Φ_{max} by the equation

$$\Phi_{\text{max}} = \left(M - \tfrac{1}{2} \right) \pi \,,$$

Φ_{max} is also the related to (n_2/A_{eff}) by the equation

$$\Phi_{\text{max}} = \left(\frac{2\pi}{\lambda} \right) \left(\frac{n_2}{A_{\text{eff}}} \right) L_{\text{eff}} P_0 \,,$$

where P_0 is the incident power into the test fiber and L_{eff} is the effective length of fiber and expressed by the equation,

$$L_{\text{eff}} = \frac{1 - \mathrm{e}^{-\alpha L}}{\alpha} \,,$$

where α is the absorption coefficient and L is the length of the test fiber. (n_2/A_{eff}) can be estimated from the slope of Φ_{max} against P_0.

11.5.3 Fiber Bragg Grating

The ohotosensitivity of silica fiber was discovered in 1978 by *Hill* et al. at the Communications Research Center in Canada [11.92]. Fiber Bragg grating (FBG) devices based on these phenomena allow the integration of sophisticated filtering and dispersion functions into

a fiber and have many applications in optical fiber communication and optical sensor systems. This subsection summarizes FBG technology and their properties. More information on FBGs can be found in the following references [11.93–95].

Photosensitivity

When ultraviolet light radiates an optical fiber, the refractive index is changed permanently; this effect is called photosensitivity. The change in refractive index is permanent if the fiber is annealed appropriately. These phenomena were first discovered in a fiber with a germanium-containing core, and have been observed in a variety of different fibers. However, optical fiber with germanium-containing core remains the most important material for FBG devices. 248 and 198 nm radiation from KrF and ArF lasers with a pulse width of ≈ 10 ns at a repetition rate of ≈ 100 pps are most commonly used. Typically fibers are exposed to laser light for a few minutes at irradiation levels in the range $100–1000$ mJ/cm^2. Under these conditions, the index change Δn of fibers with germanium-containing cores is in the rage between $10^{-5}–10^{-3}$. Irradiation at higher intensities introduces the onset of different kinds of photosensitive processes, leading to a physical damage. The index change can be enhanced by processing fibers prior to irradiation with hydrogen-loading [11.96] and flame-brushing [11.97] techniques. (Photoinduced index changes up to 100 times greater are obtained by hydrogen loading for a Ge-doped core fiber, and a ten times increase in the index change can be achieved using flame brushing.) The physical

Incident
ultraviolet
light beam

Grating
corrugations

Silica glass phase grating
(zero order suppressed)

Diffracted
beams

Fiber
core

−1st order

Zero order

+1st order
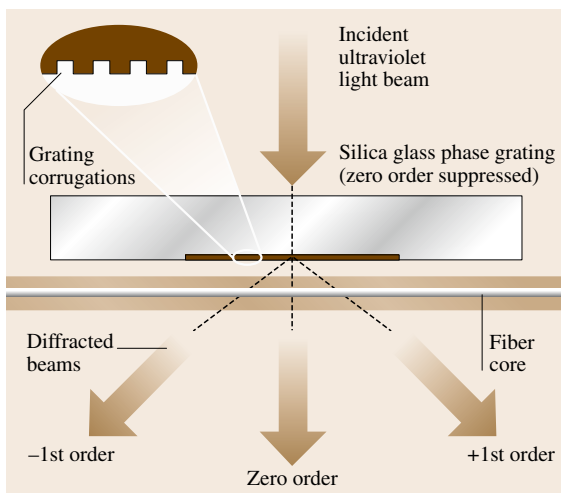
Fig. 11.71 FBG fabrication with phase mask technique

process underling photosensitivity is not completely understood, however it is believed to be related to the bleaching of the color centers in the ultraviolet spectral range.

Fabrication Techniques

Many techniques have been developed for the fabrication of FBG, e.g. the transverse holographic technique [11.98], the phase mask technique [11.99] and the point-by-point technique [11.100]. The phase mask technique is the most common because of its simple manufacturing process, high performance and great flexibility.

Figure 11.71 shows a schematic diagram of the phase mask technique for the manufacture of FBGs. The phase mask is made from a flat silica-glass slab with a one-dimensional periodic structure etched using photolithography techniques.

The phase mask is placed almost in contact with the optical fiber at a right angle to the corrugation and the ultraviolet light is incident normal to the phase mask. Most of the diffracted light is scattered in the $+1$ and -1 orders because the depth of the corrugation is designed to suppress diffraction into the zeroth order. If the period of the phase mask grating is Λ, the period of the photoimprinted FBG is $\Lambda/2$, which is independent of the wavelength of the irradiated ultraviolet. The phase mask technique greatly simplifies the manufacturing process and its low coherence requirement on the ultraviolet beam permits the use of a conventional excimer laser. The phase mask technique not only yields high-performance devices, but is very flexible, i. e. apodization and chirping techniques are easily introduced to control the spectral response characteristics of the FBGs [11.101].

Another approach to the manufacture of FDB gratings is the point-by-point technique, in which each index perturbation is written point by point. This technique is useful for making long-period FBG devices that are used for band-rejection filters and fiber-amplifier gain equalizers.

Properties of FBGs

Light propagating in an FBG is backscattered by Fresnel reflection from each successive index change. The back reflections add up coherently in the region of the Bragg wavelength, λ_B and cancel out in the other wavelength regions.

The reflectivity of strong FBGs can approach 100% at the Bragg wavelength, whereas the light in the other spectral region passes through the FBG with negligible

loss. The Bragg wavelength λ_B is given by

$$\lambda_B = 2N_{eff}\Lambda ,$$

where N_{eff} is the modal index of the fiber and Λ is the grating period.

The Bragg grating can be described theoretically by using coupled-mode equations [11.102]. Here important properties are summarized for the tightly bound single-mode propagation through a uniform grating. The grating is assumed to have a sinusoidal index profile with amplitude Δn. The reflectivity R of the grating at the Bragg wavelength is expressed by the simple equation, $R = \tanh^2(\kappa L)$ where $k = (\pi/\lambda)\Delta n$ is the coupling coefficient and L is the length of the grating. The reflectivity is determined by κL, and a grating with a κL greater than one is termed a strong grating whereas a weak grating has a κL less than one. Figure 11.72 shows the typical reflection spectra for weak and strong gratings.

The other important property of FBGs is the reflection bandwidth. In the case of weak coupling ($\kappa L < 1$), the $\Delta\lambda_{FWHM}$ is approximated by the spectral distance from the Bragg wavelength, λ_B to the neighboring dip wavelength, λ_D; $\Delta\lambda_{FWHM} \approx (\lambda_0 - \lambda_B) = \lambda_B^2/(2N_{eff}L)$. The bandwidth of a weak grating is inversely proportional to the grating length and can be very narrow for a long grating. On the other hand, in the case of strong coupling ($\kappa L > 1$), $\Delta\lambda_{FWHM}$ is approximated by the wavelength difference between the adjacent reflection dips across the Bragg wavelength, $\Delta\lambda_{FWHM} = 4\lambda_B^2\kappa/(\pi N_{eff})$. The bandwidth is directly proportional to the coupling coefficient κ.

The bandwidth of the FBG is limited by the attainable values of the index perturbation, Δn, of the photosensitivity, and several nanometers is the actual limit corresponding to $\Delta n \approx 0.001$ at wavelengths used for optical fiber telecommunications, 1.5 μm.

A chirped or aperiodic grating has been introduced in order to broaden the spectral response of FBGs.

The spectral response of a finite-length grating with a uniform index modulation has secondary maxima on either side of the main reflection peak, as shown in Fig. 11.72 [11.95]. This kind of response is detrimental to applications such as wavelength division multiplexing. However, if the index modulation profile Δn along the fiber length is apodized, these secondary peaks can be suppressed. Using the apodization technique, the side lobes of the FBG have been suppressed down to $30 \approx 40$ dB.

Another class of grating, termed the long-period grating, was proposed by *Vengsarkar* et al. [11.103]. Gratings with longer periods, ranging into the hundreds of micrometers, involves coupling of a guided mode to forward-propagating cladding modes; the cladding modes are attenuated rapidly due to the lossy cladding coating. FBGs with a long-period grating act as transmission filters with rather broad dips and are utilized as band-rejection filters and fiber amplifier gain equalizers [11.104].

Measurement of FBG Performance

Narrow-band filters with high dynamic range are the key components for dense WDM fiber optic network systems.

However, their characterization was not easy until ultra-high resolution optical spectral analyzers became available. Q8384 (Advantest LTd.) and AQ6328C (Ando Co.) with a folded-beam four-grating configuration have a 0.01-nm resolution and 60-dB dynamic range at 0.2 nm away from the central wavelength. By using such a high-performance spectrometer together with a fiber-coupled broadband light source, characterization of FBGs is no longer difficult.

Applications of FBGs

Many potential applications of FBGs in optical fiber communication and optical sensor systems are reviewed in the reference [11.102]. FBG devices have many excellent properties for fiber optic communication systems, i. e., narrow-band and high-dynamic-range fil-
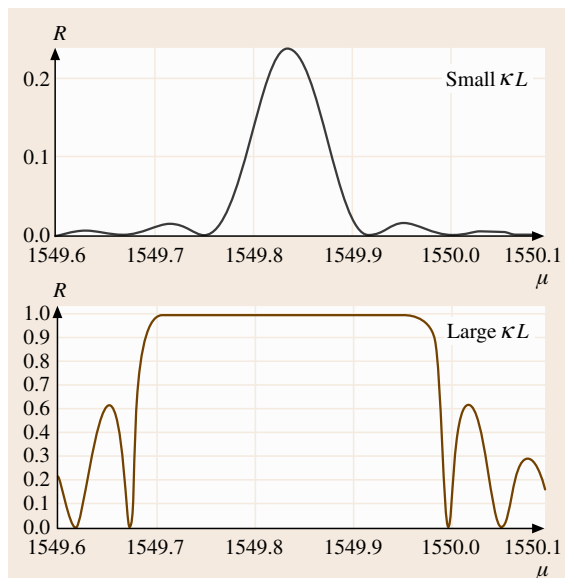
Fig. 11.72 Typical reflection spectra of weak and strong FDGs (after [11.95])

tering, low insertion loss, low back reflection and so on. So, FBG devices acquired a lot of applications in the fiber optic communication system in a short period, e.g., add–drop filtering devices, dispersion-compensation devices, gain-equalizing filters in fiber amplifiers, and wavelength locking of pump lasers.

Figure 11.73 shows some examples of FBG applications in optical fiber communication network systems. Figure 11.73a presents a schematic diagram of a multichannel dispersion compensator. FBG devices are inherently reflection filtering function whereas a transmission device is usually desired. A narrow-band transmission filtering function is commonly realized with the aid of an optical circulator. Figure 11.74b shows the wavelength locking of pump lasers for Er-doped optical amplifiers. Feedback of the weakly reflected light from FBG locks the lasing wavelength of diodes to λ_B. The temperature coefficient of the fractional change of Bragg wavelength, $\Delta\lambda_B/\lambda_B$ is $\approx 10^{-5}$ due to the very stable thermal properties of silica glass. This value is one order of magnitude lower than the temperature stability of the wavelength of DFB lasers, and is two orders of magnitude smaller than the gain peak shift of conventional laser diodes. So, wavelength locking of the pump laser stabilizes the properties of Er-doped fiber amplifiers against temperature shifts and aging effects.

A change of the in the value of L and N_{eff} causes a shift of the Bragg wavelength, and the fractional change, $\Delta\lambda_B/\lambda_B$ is given by the equation [11.106]

$$\frac{\Delta\lambda_B}{\lambda_B} = \frac{\Delta\Lambda}{\Lambda} + \frac{\Delta N_{\text{eff}}}{N_{\text{eff}}} ,$$

where $\Delta\Lambda/\Lambda$ and $\Delta N_{\text{eff}}/N_{\text{eff}}$ the fractional changes of the period and effective modal index, respectively. An axial change results in a shift of the Bragg wavelength given by the equation

$$\frac{1}{\lambda_B}\left(\frac{\Delta\lambda_B}{\varepsilon}\right) = \frac{1}{\Lambda}\frac{\Delta\Lambda}{\varepsilon} + \frac{1}{N_{\text{eff}}}\left(\frac{\Delta N_{\text{eff}}}{\varepsilon}\right) .$$

The first term on the right is unity by definition and the second term, which is approximately -0.27 for silica fiber, represents the change due to the photoelastic effect. So, the fractional change of the Bragg wavelength due to axial strain is 0.73ε. This property of FBGs can be used in strain sensors [11.106].

11.5.4 Fiber Amplifiers and Lasers

Fiber amplifiers are key components in the current dense wavelength-division multiplexed (DWDM) telecommunication system. Er-doped fiber amplifiers (EDFA),
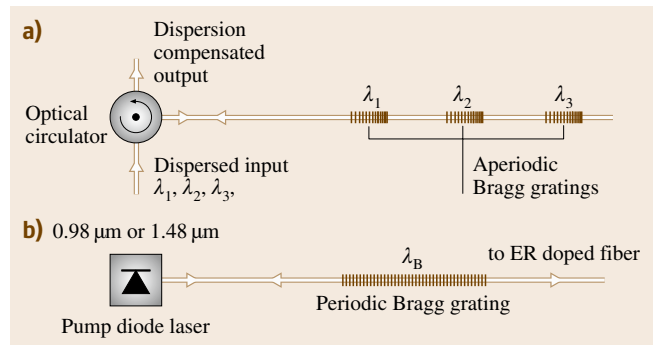
Fig. 11.73a,b Some applications of fiber Bragg gratings
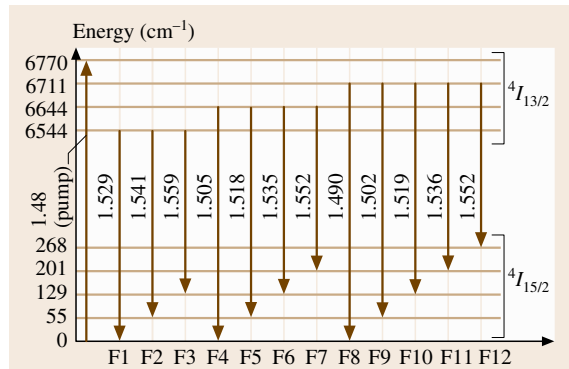
Fig. 11.74 Energy-level diagram for erbium. Optical gain occurs in the vicinity of 1.53 μm under pumping at a wavelength of 0.98 or 1.48 μm (after [11.105])

which have a stimulated emission band in the vicinity of 1.53 μm, are most widely used as repeaters in the optical network. Fiber amplifiers and lasers have many excellent properties, e.g. high efficiency, compactness, thermal and mechanical stability, and so are used in many scientific, medical and industrial applications.

This subsection summarizes Er-doped fiber amplifiers and briefly introduces some recent advancements in femtosecond fiber lasers and high-power fiber lasers with a double-cladding structure.

Er-doped Fiber Amplifiers (EDFAs)
Energy Levels of Er. Figure 11.74 shows an energy diagram for erbium. Gain in EDFAs occurs in the vicinity of 1.53 μm when an inversion population exists between the $^4I_{13/2}$ and $^4I_{15/2}$ states; this is realized by optical pumping at the wavelengths of 0.98 μm (pumping to $^4I_{11/2}$) or 1.48 μm (pumping to $^4I_{13/2}$) [11.105, 107].

When Er ions are incorporated into the fiber core, each ion level, $^{2S+1}I_J$ presents Stark splitting due to

the interaction between the ion and host matrix. Other mechanisms, thermal fluctuation and inhomogeneous environments in the glass matrix further broaden the emission spectrum. Figure 11.75 shows the absorption and emission spectra for erbium in silica with aluminum and phosphorous codoping [11.108]. The spectrum is constructed from the superposition of the transitions between the Stark levels and is sensitive to the host material. Considerable effort has been devoted to obtaining broadened shapes for the emission spectra for a broadband amplifier. Use of alumino-silicate glass (SiO_2–Al_2O_3) results in slight broadening and smoothing over the pure SiO_2. The use of fluoride-based glasses such as ZBLAN provides significant improvements on spectral width and smoothness [11.109, 110].

EDFA configuration. A general fiber amplifier configuration is shown in Fig. 11.76. A typical Er-doped
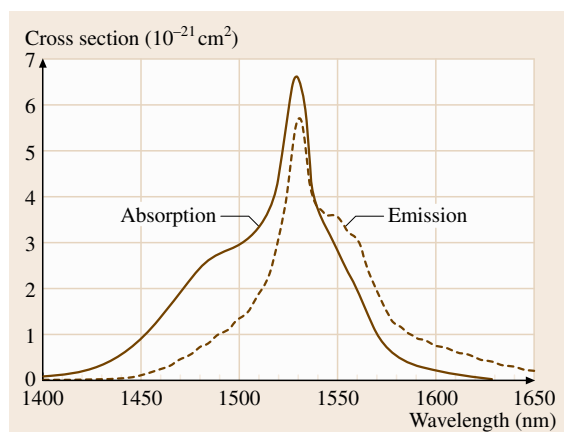
Fig. 11.75 Absorption and emission spectra for erbium in silica with aluminum and phosphorous codoping. Spectrum associated with the transition in Fig. 11.73 (after [11.108])

Fig. 11.76 Er-doped fiber amplifier configuration with bidirectional pumping

amplifier consists of an Er-doped fiber positioned between optical isolators. Pump light is introduced into the Er-doped fiber through a wavelength-selective coupler, which can be configured for either forward or backward pumping, or for bidirectional pumping. In either case, pump power is absorbed over the amplifier length, such that the population inversion varies with position along the fiber. To get the highest overall effect, the fiber length is chosen so that the length the fiber is transparent to the signal at the point of minimum pump power, i. e., the fiber end opposite to the pump laser for unidirectional pumping and at the midpoint for bidirectional pumping. Other factor like gain saturation and amplified spontaneous emission (ASE) may modifies the optimum length of fiber amplifier [11.111]. Optical isolators are usually positioned at the entrance and exit to avoid gain quenching, noise enhancement or possibly parasitic lasing due to the unfavorable backscattering or reflected light.

Operating regime. There are three operating regimes, which depend on the use intended for the amplifier [11.112]: 1) small-signal, 2) saturation and 3) deep saturation regimes. In the small-signal regime, a low input signal ($< 1 \mu W$) is amplified with negligible saturation. Small-signal gains of EDFAs range between 25 and 35 dB. The gain efficiency is defined as the ratio of the maximum small-signal gain to the input pomp power. Gain efficiencies of well-designed EDFA are ≈ 10 dB/mW for pumping at $0.98 \mu m$ and ≈ 5 dB/mW for pumping at $1.48 \mu m$. In the saturation regime, the output power is reduced significantly from the power expected in the small-signal regime. Input saturation power is defined as the input signal power required to reduce the amplifier gain by 3 dB. Alternatively, saturation output power is defined as the amplifier output when the gain is reduced by 3 dB. For the power amplifier applications, where the amplifiers operate in the deep saturation regime, the power conversion efficiency between pump and signal is important.

However, to achieve deep saturation the input signal must be high enough, so the more important situation is the saturation regime, where the choice of pumping configuration and pump power can substantially influence the performance [11.112].

Noise and gain flattening. Noise is a very important factor in telecommunication applications and is quantified using the noise figure. The noise figure of an EDFA is defined in a manner consistent with the IEEE standard definition for a general amplifier. For a shot-noise-limited input signal, the noise figure is defined
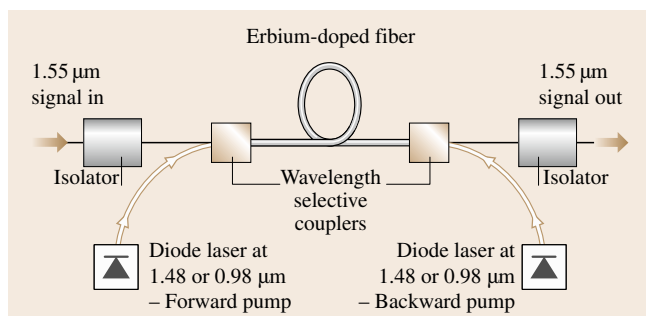
as the signal-to-noise ratio of the input divided by the signal-to-noise ratio of the output. The most serious noise source of EDFA is amplified spontaneous emission (ASE), which can be reduced by ensuring that the population inversion is as high as possible. With 0.98 μm pumping theoretically limited noise figures of about 3 dB have been obtained, while the best results for 1.48 μm pumping have been around 4 dB because of the difference in the pump scheme [11.113].

DWDM systems needs a flattened gain spectra for all wavelength channels. Gain-flattening techniques are classified into three categories. First, use of alumino-silicate glass or fluoride-based glass with smoother and broader gain spectra. Second, spectral filtering at the output of an amplifier or between the cascaded amplifiers. Third, hybrid amplifiers with different gain media in cascaded and parallel configurations. Flattened gain spectra of EDFA have been extended in the range 12 to 85 nm.

For more details of Er-doped amplifiers, excellent reviews and text books are available [11.111, 112, 115].

Other Fiber Amplifiers

EDFAs have excellent performances within the conventional gain band (1530–1560 nm) and recent efforts have resulted in the extension of EDFA gain into the longer wavelength range (1565–1625 nm). Other rare-earth dopants or dopant combinations have been used to produce fiber amplifiers that have gain at other wavelength region. These include praseodymium-doped fiber amplifiers, which have gain at 1300 nm and are pumped at 1020 nm [11.116]. Thulium-doped fibers have been developed for amplification at 1480 nm [11.117, 118] and 1900 nm [11.119]. Ytterbium-doped fibers amplify radiation in the wavelength range from 975–1150 nm with the pump wavelengths between 910 and 1064 nm. Erbium-ytterbium codoped fibers provide gain around 1550 nm with the pumping sources, similar to ytterbium-doped fibers [11.120]. Neodymium-doped fiber amplifiers works in the wavelength range 1064–1088 nm under pumping at 810 nm.

Raman amplifiers have also been developed by using the fiber transmission line as a gain media to increase the bandwidth and flexibility of the optical network. Raman amplifiers need multiple high-power pump sources at different wavelengths to realize broadband amplification [11.121].

Fiber Lasers

Fiber lasers are configured by replacing the isolators at both ends of fiber amplifiers by fiber Bragg gratings or making a closed loop with couplers. In the case of a ring laser one need a coupler for the output. Fiber lasers are inherently compact, lightweight and maintenance-free, and also do not require any water cooling. So, fiber lasers have already been deployed in some industrial applications.

Er fiber lasers can be pumped with telecom-compatible pump diodes and allow for the straightforward excitation of soliton pulses using standard optical fibers. Figure 11.77 shows a configuration of the passively mode-locked all-fiber laser, which is referred to as a figure-of-eight laser because of its layout [11.114]. Nonlinear all-optical switch including a nonlinear amplifying loop mirror allows self-starting mode-lock operation for femtosecond pulses. Current passive mode-locking lasers are usually based on the nonlinear polarization evolution in a slightly birefringent fiber because they require the least number of optical components [11.122]. Currently, mode-locked fiber lasers which generate pulses with width from 30 fs to 1 ns at repetition rates ranging from 1 MHz to 200 GHz have been developed in a variety of technologies. Details of these ultrafast lasers can be found in the textbook [11.123].

Conventional fiber lasers as well as EDFAs have simple structures with a single core for guiding both the signal and the pumped light, implying that single-mode pump diodes must be used.

The limited available power of single-mode diode-pumped sources has limited the output power to ≈ 1 W. Cladding pumping has been developed as a method to overcome this situation using the so-called double-clad fiber shown in Fig. 11.78. Double-clad fiber has a rare-earth-doped core for guiding the single-mode output beam, surrounded by a lower-index inner cladding. The inner cladding also forms the core for a secondary waveguide that guides the pumped light. The inner cladding is surrounded by an outer cladding of lower refractive index material to facilitate waveguiding.
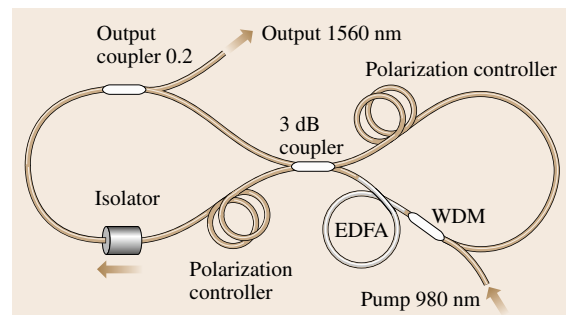
Fig. 11.77 Set-up of passively mode-locked figure-of-eight laser (after [11.114])
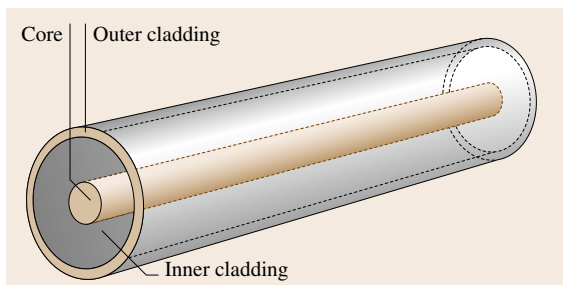
Fig. 11.78 Schematic drawing of a double-clad fiber

Cladding-pumped fiber lasers accommodate high-power multimode pump sources, but can still produce a single-mode output. In the last decade various pumping schemes, such as star-coupler pumping [11.124], V-groove pumping [11.125] and side-coupler pumping [11.126, 127], have been developed to increase the available count of multimode pump sources in addition to the simple end-pumping approach [11.128, 129]. Cladding-pump technology has drastically increased the output power of fiber lasers to well over 100 W even in single-mode operation and seems likely to surpass bulk lasers in many industrial application areas.

11.5.5 Miscellaneous Fibers

In addition to silica-glass-based fibers, many kinds of optical fibers have been developed for various applications, such as local area networks, laser power delivery and optical sensing. In this section, most viable and commercially available fibers are reviewed.

Infrared Fibers

Infrared fibers, defined as fiber optics transmitting radiation with wavelengths greater than $2\,\mu m$ are divided into three categories, i.e., glass, crystalline, and hollow waveguides. Figure 11.79 shows the optical loss for the most common infrared fibers [11.135]. In general, both the optical and mechanical properties of infrared lasers are inferior to those of silica-based fibers, and the use of infrared fibers is still limited to applications in laser power delivery, thermometry, and chemical sensing.

HMFG Fibers. Heavy-metal fluoride glass (HMFG), most commonly, ZrF_4–BaF_2–LaF_3–NaF (fluorozirconate, ZBLAN) and AlF_3–ZrF_4–BaF_2–CaF_2–YF_4 (fluoroaluminate) presents a low optical loss around $2.5\,\mu m$ [11.130]. The attenuation in HMFG fiber is predicted to be about ten times less than that for silica fibers based on extrapolations of the intrinsic losses resulting from Rayleigh scattering and multiphonon absorption [11.136]. ZBLAN is also a candidate host material for various fiber amplifiers because of the smoothed broadened spectra. However, their low durability against moisture attack and poor mechanical strength prevent their widespread use. The losses of fluoroaluminate fibers are not as low as for the ZBLAN, but fluoroaluminate fibers have the advantage of higher glass-transition temperatures and therefore are more promising for the power delivery of Er:YAG laser wavelength of $2.94\,\mu m$.

Germanate fibers. Heavy-metal-oxide glass fibers based on GeO_2 are an alternative candidate to HMFG fibers for $3\,\mu m$ laser power delivery because of a higher glass-transition temperature ($680\,°C$) and excellent durability [11.137]. These fibers have a higher damage threshold and can deliver laser powers over $20\,W$ from Er:YAG lasers.

Chalcogenide fibers. Chalcogenide glass fibers are classified into three categories: sulfide, selenide ,and tellulide. One or more chalcogen elements are mixed with one or more elements such as As, Ge, P, Sb, Ga to form a glass. Chalcogenide glasses are stable, durable, and insensitive to moisture. Generally, the glasses have a low softening temperature and a rather large value of dn/dT. This fact limits their laser power-handling capability, and the fibers are considered to be a promising candidate for evanescent-wave fiber sensors and in-
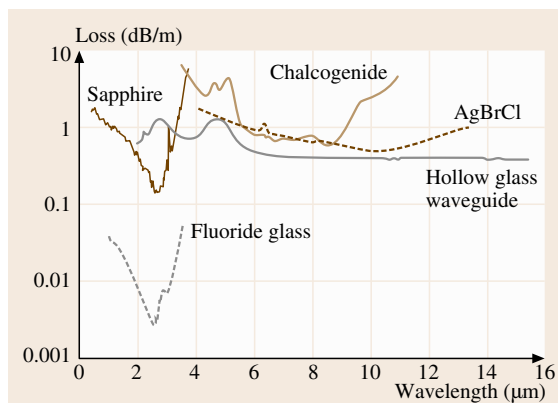
Fig. 11.79 Loss spectra for some common infrared fiber optics: ZBLAN fluoride glass [11.130], single-crystal sapphire [11.131], chalcogenide glass [11.132], polycrystalline AgBrCl [11.133], and a hollow-glass waveguide [11.134] (after [11.135])

frared fiber image bundles. The loss spectra for the most important chalcogenide fibers, AsGeSeTe [11.132] are shown in Fig. 11.79.

Crystalline fibers. Sapphire is an extremely hard, robust and insoluble material with an infrared transmission region from 0.5 to 3.2 μm and a melting point of over 2000 °C. These superior physical properties make sapphire the ideal infrared fiber candidate for applications at wavelengths less than 3.2 μm. The disadvantage of sapphire single-crystal fiber is fabrication difficulties. Fiber diameters range from 100 to 300 μm and lengths are generally less than 2 m. The loss spectra of sapphire fiber [11.131] are shown in Fig. 11.79. Fiber loss is less than 0.3 dB/m at the Er:YAG laser wavelength of 2.94 μm, and the fibers are used to deliver over 10 W of average power. Sapphire fiber can be used at temperatures up to 1400 °C without any change in transmission.

Halide crystals have excellent infrared transmission, especially in the longer wavelength region. However, only the silver and thallium halides have been successfully fabricated into fiber optics, using a hot extrusion technique. In the hot extrusion process, a single-crystal perform is placed in a heated chamber at a temperature equal to about half the melting point, and the fiber is extruded to a fiber shape through a diamond or tungsten carbide die. The fibers are usually 900−500 μm in diameter. The loss spectra of polycrystalline AgBrCl fiber [11.133] are shown in Fig. 11.79. The loss at 10.6 μm can be as low as 0.2 dB/m and the transmission band extends up to about 20 μm.

Hollow glass waveguides. Previously, hollow waveguides were formed using metallic and plastic tubing. Today, the most popular structure is the hollow glass waveguide (HGW). The advantage of glass tubing is that it is much smoother than either metal or plastic tubing. HGWs are fabricated using a conventional wet process first to deposit a layer of Ag film on the inside of silica glass tubing, and then a dielectric layer of AgI is formed over the metallic film by converting some of the Ag to AgI. The thickness of the AgI is optimized to give high reflectivity at a particular laser wavelength [11.138]. The spectral loss for an HGW with a 530 μm bore, which is optimized for a wavelength of 10 μm [11.134], is shown in Fig. 11.79. HGWs have been used successfully in infrared laser-power delivery and some sensor applications. CO_2 and Er:YAG laser power below about 80 W can be delivered without difficulty. Employment of water-cooling jackets fur-

ther increased the handlable laser power up to about 1 kW [11.139].

More detailed information on infrared fibers can be found in the literature [11.140].

Plastic optical fiber. Plastic optical fibers are commercially available for local-area networks, sensing use, and illumination. Conventional plastic optical fibers are multimode fibers with a large core diameter of about 1000 μm and are made of polymethyl methacrylate (PMMA). Figure 11.80 shows the transmission loss of the plastic optical fibers as a function of wavelength [11.141]. The transmission loss reaches a minimum value of about 100 dB/km around the spectral region between 500 and 600 nm. Usually, signal transmission lines of plastic optical fibers use 650 nm light-emitting diodes and the transmission distance is limited to 50 m because of the relatively high transmission loss (160 dB/km).

Recent development of perfluorinated plastic optical fibers significantly improved the transmission characteristics of plastic optical fibers in the spectral region from visible to 1300 nm because the perfluorinated polymer has no C–H bond in its chemical structure. The specific loss at a wavelength of 850 nm is 17 dB/km. Signal transmission at 2.5 Gb/s was conducted over 144 m perfluorinated graded-index plastic optical fiber with an 850 nm vertical-cavity surface-emitting laser (VCSEL) transceiver [11.142].

Photonic Crystal Fibers

The photonic band gap concept triggered the development of photonic crystal fibers [11.143, 144]. Since the first fabrication of photonic crystal fiber (PCF) in 1995 [11.145], a sequence of innovations has been
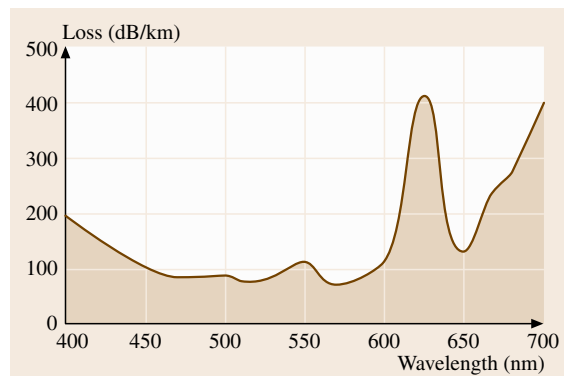
Fig. 11.80 Transmission loss in plastic optical fiber

achieved in fiber optics technology. The remarkable properties of PCF have overturned many of the key precepts of textbook fiber optics. The enormous potential offered by this new structure may make current fiber optic technology obsolete.

PCFs are optical waveguides in which a microstructured cladding confines light to the fiber core. Unlike conventional all-solid fibers, which guide light by the total internal reflection at the core–clad interface, the new structures provide great freedom to control the characteristics of the fibers.

PCFs are divided into two categories based on the principal mechanism by which light is confined to the core. One of these is a species of total reflection, and the other is a new physical effect – the photonic band gap. Those typical structures are shown in Fig. 11.81.

The first type of PCF usually has a silica core surrounded by the air hole, as shown in Fig. 11.81a. Optical confinement is achieved when the effective (area-averaged) refractive index is lower in the cladding region than in the core.

Figure 11.81b shows the structure of the photonic band gap and hollow-core PCF. The guiding mechanism relies on the coherent backscattering of light into the core. This effect, which is based on the photonic band gap (PBG), allows fiber to be made with hollow core.

PCF can be made by stacking tubes and rods of silica glass into a structure that is a macroscopic preform of the pattern of holes required in the final fiber. The typical dimension of this preform is 1 m long and 20 mm in diameter. The preform is then introduced into the furnace of a fiber-drawing tower.

Index-Guiding PCF
Large core. Light can be guided in PCFs by embedding a region of solid glass enclosed by an array of air holes. This approach has several important applications, and an excellent introduction is available in the review [11.146]. Index-guiding PCF provides new opportunities that stem from the special properties of the photonic crystal cladding, which are caused by the large refractive index contrast and the 2-D nature of the microstructure. These affect the dispersion, smallest attainable core size, the number of guided mode and the birefringence in a different way to conventional silica fiber.

For example, endlessly single-mode PCF can be made with a very large core area [11.147, 148]. In contrast with conventional fibers, single-mode operation is guaranteed in solid-core PCF whatever the overall size of structure – in particular for large core – provided that

the ratio of hole-diameter to spacing is small enough. Ultra-large mode area PCF may have applications in high-power transmission and high-power lasers and amplifiers [11.149].

Small core. In contrast, if the holes are enlarged and the overall scale of the structure reduced so that the solid core is $\approx 0.8\,\mu m$ in diameter (ultra-small mode), the zero-dispersion wavelength can be 560 nm in the green. This is quite different from the zero-dispersion wavelengths in conventional silica fibers. In fact, the group velocity dispersion can be radically affected by pure waveguide dispersion in fibers with small cores and large air holes in the cladding [11.150]. Another feature of fibers with ultra-small mode area is that the intensity of light attainable for a given launched power is very high, so nonlinear optical effects can be easily obtained. With a fiber with a small core and a zero-dispersion wavelength around 800 nm, femtosecond pulses from a Ti:sapphire laser was efficiently converted to a single-mode broadband optical continuum [11.151], which is already being used in frequency metrology [11.152], optical coherence tomography [11.153] and spectroscopy. Enormous birefringence that exceeds values attained in conventional fibers by an order of magnitude, have already been achieved in PCFs [11.154].

Hollow-Core Photonic Band Gap Fibers
In 1999, the first hollow-core photonic band gap fiber was drawn from a stack of thin-wall silica capillaries with an extra large hole in the center, which was formed by omitting seven capillaries from the stack [11.155]. The strong wavelength dependence of guiding indicated a photonic band gap effect: only certain wavelength
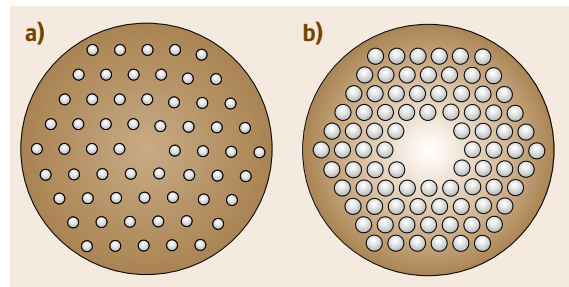
Fig. 11.81a,b Two different designs of PCF. **(a)** shows a single-mode fiber with a pure silica core surrounded by a reduced-index photonic-crystal cladding material, **(b)** is an air-guiding fiber in which the light is confined to a hollow core by the photonic-band-gap effect

ranges fall within the band gaps and are guided, while other light quickly leaks out of the hollow core.

The most important factor for any fiber technology is loss. Loss in conventional fibers has been reduced over the past 30 years and seems to be approaching the material limit. However, losses in hollow-core photonic band gap fibers might be reduced below the levels found in conventional fibers because the majority of the light travels in the hollow core, in which scattering and absorption could be very low. Confinement losses can be eliminated by forming a sufficiently thick cladding. However, increased scattering at the many surfaces is a potential problem. The lowest attenuation reported to date for hollow-core photonic band gap fiber is 1.7 dB/km [OFC-PD] [11.156], and is still an order of magnitude higher than that of conventional state-of-the art silica fibers, 0.15 dB/km [11.157]. The dramatic reduction of loss over the past few years suggests that it will be reduced still further. Dispersion is far lower than in solid-core fibers. Group velocity dispersion (GVD) in these fibers – a measure of their tendency to lengthen a short pulse during propagation – crosses zero within the low-loss window, and is anomalous over much of the wavelength band. This implies that these fibers could support short-pulse propagation as optical solitons. The Kerr nonlinearity of the hollow-core fiber was low because it was filled with gas, whereas the effects of Raman scattering were eliminated by filling the fiber with xenon. Hollow-core fibers exhibited a substantially higher damage threshold than conventional fibers [11.158], making them suitable for delivery of high-power beams for laser machining and welding. 200-fs 4-nJ pulses from a Ti:sapphire laser have been transmitted through 20 m of hollow-core fibers with a zero-GVD wavelength of 850 nm, and the autocorrelation width of the output pulse was broadened to roughly 3.5 times the input pulse, partly due to the modest spectral deformation [11.159]. Further improvement is expected by working away from the zero-GVD wavelength. Hollow-core fibers seem to have massive potential.

11.6 Evaluation Technologies for Optical Disk Memory Materials

Two types of rewritable optical disks are well-known today. One is a phase-change optical disk that utilizes the phenomenon of optical changes that accompany the reversible phase transitions between amorphous and crystalline states. Utilizing phase-change materials, various rewritable optical disks such as DVD-RAM, DVD-RW, CD-RW and blu-ray discs have been commercialized. The other is a magnetooptical (MO) disk that utilizes the polar Kerr effect. It is known that the polarization plane of linearly polarized light revolves slightly when it is reflected from a perpendicularly magnetized magnetic film. MO disks have also been commercialized as various office tools and as the Mini-Disc (MD) for audio use. In this section, the evaluation technologies for a phase-change material are first explained, and those for an MO material follow. For each case, evaluation technologies are mainly described from two points of view: the material property itself and the device property that uses the memory material. As described below, the the properties of the two materials are very different, while the second aspect is generally common. Strictly speaking, various drive technologies such as servo technology and optics etc. are necessary to carry out sufficiently precise evaluations. However, the essence of them will be understood by the descriptions here.

11.6.1 Evaluation Technologies for Phase–Change Materials

To evaluate phase-change memory materials, knowing their thermal and optical characteristics is essential. This is because i) the optical change is dominantly and directly determined by the change of optical properties of the phase-change films, and ii) the phase-change mechanism is typically a thermal process. It is also very important to examine the thermal and optical properties of additional layers such as transparent protection layers composed of dielectric materials and reflection layers composed of metallic materials. The typical layer structure of a phase-change optical disk is shown in Fig. 11.82. Accordingly, practical optical disk characteristics can be estimated by knowing the thermal and optical characteristics of all these films. However, the evaluation technology is limited to the phase-change materials themselves due to space restriction.

Research and Development History of Phase–Change Materials

Today, many phase-change optical disks have been put to practical use. Without exception, they have adopted chalcogenide films for their memory layers. Study of chalcogenide alloys started in Russia in the 1950s.

Fig. 11.82 Cross section of a typical layer structure of phase-change optical disk with four layers

Kolomiets et al. found that various chalcogenide alloys, such as Tl–Te and Tl–Se, could be easily vitrified and the obtained glassy substance showed semiconductor properties [11.160]. These new glass materials were named *dark glass* in contrast to the conventional transparent oxide glasses, and they were generically called chalcogenide glass semiconductor in the 1960s.

Ovshinsky's group first demonstrated the great potential of these glass materials as optical memories. In 1971, *Feinleib* et al. reported that a short laser pulse induced instant and reversible phase changes on a chalcogenide glass semiconductor thin film, representatively $Te_{81}Ge_{15}Sb_2S_2$ [11.161]. This result aroused large research and development (R&D) activities all over the world at the beginning of the 1980s, and various materials, especially Te-based eutectic alloys, were studied towards the beginning of the 1980s [11.162–165].

However, these Te-based eutectic compositions have not ultimately resulted in practical use, and R&D activities on phase-change optical memories declined in the mid-1980s. This is because conventional chalcogenide glass materials had several fatal problems, such as data rewriting speed and cyclability, for a rewritable optical memory.

Under these circumstances, *Yamada* et al. proposed the $GeTe - Sb_2Te_3$ pseudo-binary material system (hereinafter denoted by GeSbTe) based on a novel concept [11.166]. The largest difference between GeSbTe and the conventional materials is that GeSbTe is no longer a chalcogenide glass but just a chalcogenide while the conventional materials have characteristics suitable for the name of chalcogenide glasses [11.167]. GeSbTe has solved the fundamental problems and realized a very short crystallization time of several tens of nanoseconds, more than 100 000 cycles of data rewriting, and tens of years of estimated life. It can be said

that this material created a new era for the R&D of phase-change optical memories. The basic concept of GeSbTe has been succeeded by other materials such as AgInSbTe and $Ge(Sb_{75}Te_{25}) - Sb$ etc. Those are generically named $Sb - Te$ [11.168, 169]. The latest compositions being studied are Sb-based compositions including Te [11.170].

Principle of Phase–Change Recording

The phase-change principle is explained in Fig. 11.83, which shows the relation between the temperature and free energy of a substance. Molten substance crystallizes at the melting temperature (T_m) when it is gradually cooled down while maintaining thermal equilibrium. However, the molten substance sometimes does not crystallize even though it is cooled below T_m when the cooling speed is sufficiently large. This is a supercooled state and it is frozen into a noncrystalline solid called an amorphous state at a certain temperature (T_g) that is intrinsic to a substance. Conversely, the amorphous solid can be transformed into a crystalline solid by heating it above T_g for a period of time. The amorphous solid then becomes a supercooled liquid and crystallization occurs abruptly.

In order to achieve recording and erasing, it is necessary to undergo the above thermal process on a revolving optical disk. For this requirement, a well-focused laser beam is utilized. Figure 11.84 shows the heat profile of a phase-change recording film of an optical disk while the optical disk is passing through the laser beam. In the figure, two curves show the temperature at the center part of the track. When the laser power is strong enough to melt the phase-change film instantly (a), the temperature increases above T_m as the disk approaches

Fig. 11.83 Thermodynamical explanation of a phase-change process

Fig. 11.84a,b Schematic view of the thermal profile of a laser-exposed area on an optical disk while it passes through the laser spot

the laser beam, and decreases as the disk goes away from the laser beam. By designing the heat capacity of the recording film to be sufficiently small, and the thermal diffusion rate from the recording film to the adjacent films to be sufficiently large, the molten area can be transformed into an amorphous state. On the contrary, when the laser power is not high enough to elevate the film temperature over T_m but high enough to elevate it over T_g (b), it is seen from the figure that the period when the temperature is between T_g and T_m ($t1$) becomes rather longer than the case of (a). Thus, the exposed area is re-transformed into a crystalline state.

Fundamental Properties of Phase–Change Materials

For the recording film of a phase-change optical disk, optical and thermal properties are very important factors. The former is tightly related to the quality of the recording signal itself and the latter relates to the recording sensitivity or thermal reliability. At first, the technologies for obtaining the basic physical properties are described.

Melting Temperature T_m, Glass Transition Temperature T_g, and Crystallization Temperature T_x. It is widely known that the temperatures T_m, T_g, and T_x are measured using differential scanning calorimetry (DSC) or differential thermal analysis (DTA). It is generally said that measurement results by DSC have higher accuracy than with DTA. DTA is suitable for a measurement under rather high-temperature conditions. For a preparation of the specimens, phase-change films are deposited on

a glass substrate, scratched off and powdered. T_m and T_g are observed as endothermic peaks by these machines; however, it is difficult to observe T_g in the case of recent high-speed phase-change materials. It is said that T_g does not appear for those materials since T_g is higher than T_x. T_x is observed as an exothermic peak. Because T_x shows a distinct dependence on the heating rate, the activation energy can be obtained based on Kissinger's equation (11.122) as shown in Fig. 11.85.

$$\ln \frac{\alpha}{T_x^2} = \frac{\Delta E}{R} \frac{1}{T_x} + \text{const.} , \qquad (11.122)$$

where α, R, E and T_x are the heating rate, gas constant, activation energy and crystallization temperature, respectively.

Therefore, by plotting $\ln \alpha/T_x^2$ versus $1/T_x$, an activation energy E can be obtained from the slope of the graph [11.171, 172]. Each value of T_m, T_x, and E closely relates to recording sensitivity, thermal resistance of the amorphous state, and crystallization speed under high-temperature conditions.

There is another, optical method to measure T_x, which is shown in Fig. 11.86. In the case of a phase-change material, phase-change phenomenon naturally accompany distinct optical properties. Accordingly, crystallization temperatures can be measured by detecting the temperature at which the optical properties, such as transmittance and reflectivity, drastically change when elevating the temperature of the film sample at a constant heating rate. Optical changes can be detected for example using a He–Ne laser. The greatest advantage of the optical method is that a film sample can be used instead of a powdered sample. Though it is reported that T_x abruptly increases as the film thickness becomes thinner, practical T_x of an optical disk can be measured by this optical method. Additionally, it is very important that
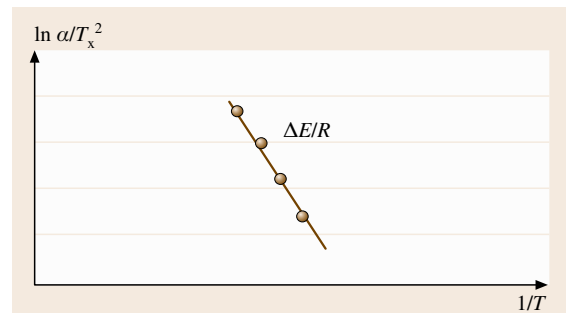
Fig. 11.85 Schematic of a Kissinger plot from which the activation energy E can be obtained as the gradient of the line
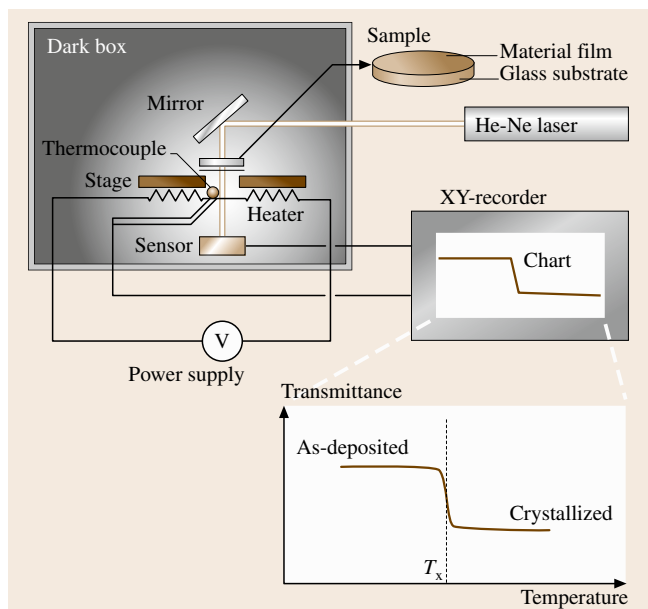
Fig. 11.86 Optical method for evaluating the crystallization temperature T_x of a phase-change thin film. The *upper* figure shows the set-up and the *bottom* shows the obtained chart

this method drastically saves time for a sample preparation.

Optical Constants. It is intrinsically important for phase-change optical materials to obtain their optical constants: n (refractive index) and k (extinction coefficient). Especially, obtaining them for wavelengths λ around $300-1000$ nm is very important since laser diodes exist in the range. With the constants both in the amorphous and crystalline states, we can simulate the optical characteristics when the materials are applied as the memory layer of optical disks. They are, for example, reflectivity, absorbance, transmittance and variations of these before and after recording. To obtain these optical constants, we can adopt a commercial ellipsometer. Since it is difficult to obtain a large laser-quenched amorphous film, an as-deposited film is usually substituted for an amorphous sample. A crystalline sample is prepared by annealing the as-deposited film in an Ar or N_2 gas atmosphere.

Optical constants can also be obtained by a calculation method. Firstly, optical reflectivity parameters (from both the film and substrate sides), transmittance and film thickness are experimentally measured using a spectrometer and a step-meter called a DEKTAK or α-step, respectively. Secondary, sets of optical parameters are calculated by assuming values for the optical

constants n and k based on the matrix method [11.173]. The measured and the calculated parameters are compared, and the assumed optical constants giving the smallest error are selected as the real values.

Crystallization Speed. Data-rewriting speed is as important a factor as recording capacity for memory devices. In the case of phase-change memory, data-rewriting speed is dominated by the crystallization speed. Since it is difficult to measure the crystallization speed directly, the evaluation of the crystallization speed is usually substituted by the required laser exposure duration that causes crystallization. The laser exposure duration can be calculated from the disk revolving speed v and the laser beam size d (laser wavelength and NA of the objective lens) on a real dynamic tester as d/v; however, a static tester is applied in order to simulate the response under a wider range of laser exposure conditions.

Figure 11.87 shows a representative set-up of a static tester and a coupon-size specimen [11.174]. On the static tester, laser exposure from a laser diode (LD) is carried out with varying laser power and exposure duration on the coupon specimen. For a detection of the exposure results, a sufficiently weakened laser beam is re-exposed and the variations are observed as the reflectivity changes. Here, it is very important that the specimen has a similar layer structure as the practical optical disks. Accordingly, dynamic properties such as crystallization time and amorphization sensitivity can be simulated on the static tester. For example, we can determine whether the materials are applicable to DVD-RAM by investigating whether their crystallization times are faster than 80 ns. The recording–erasing conditions of DVD-RAM are: revolving speed $v = 8.2$ m/s, laser beam size $d = 0.66\,\mu$m ($1/e$), calculated effective exposure duration of $d/v = 80$ ns. In the case of the $GeTe - Sb_2Te_3$ pseudo-binary system, one of the most well-known materials, the obtained crystallization time is as short as 30 ns, and it is known that this material system can be used as a memory layer for DVD-RAM [11.175].

Instrumental Analyses. For characterization of phase-change materials, various instrumental analyses are utilized. Firstly, averaged film compositions are examined using a x-ray micro analyzer (XMA), an electron-probe microanalyzer (EPMA) and inductively coupled plasma (ICP). XMA and EPMA can detect the contained elements in a microscopic area on a film sample, although the accuracy is not as high as for ICP. On the other hand, ICP can obtain very precise composition values. The weak points of ICP are that it is not suitable for detecting
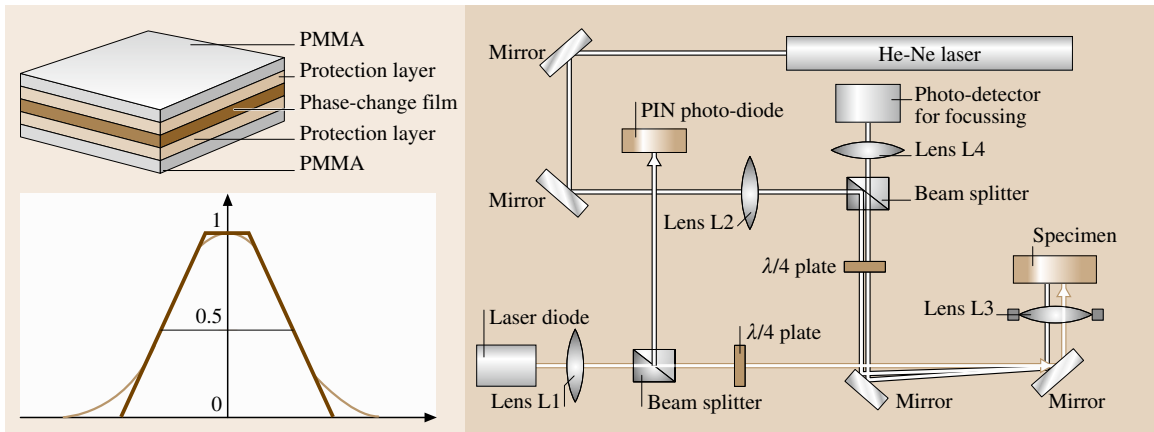
Fig. 11.87 Optical set-up and a specimen to evaluate phase-change process such as crystallization rate and crystallization–amorphization sensitivity etc.

light elements such as O and N and for detection on a limited area. In order to detect light elements, Rutherford back scattering (RBS) can be adopted.

When a depth profile of the film composition is necessary, Auger electron spectroscopy (AES) and secondary ion mass spectrometry (SIMS) are adopted. Quantitative evaluation is not possible for each method, but it is possible by comparison with reference samples whose compositions are known beforehand. To examine chemical bonding between each element, x-ray photoelectron spectroscopy (XPS) has conventionally been adopted. Recently, thermal desorption mass spectrometry (TDS) has also been developed.

For the observation of crystallization condition and shape of recording marks, transmission electron microscope (TEM) has been exclusively utilized; however, some new methods such as the scanning electron microscope (SEM) and surface potential microscope (SPOM) have become important in recent years. This is because the thickness of the memory film has become thinner and observation by TEM is becoming increasingly difficult.

To investigate the structures of memory materials, diffraction studies such as x-ray diffraction (XRD), electron diffraction (ED) and neutron diffraction (ND) are very effective. Precise structure can be obtained, for example, by applying the *Rietvelt* method to XRD results [11.176].

Dynamic Properties
of a Phase–Change Optical Disk

In this part, some dynamic properties of an optical disk will be explained. Though this handbook does not cover practical devices, it is very important for us to understand how the material characteristics relate to device performance under the practical conditions. Here, carrier-to-noise ratio (C/N), erasability, jitter, and bit error rate (BER) are explained as technologies for evaluating dynamic properties.

C/N and Erasability. C/N and erasability are the most basic items for evaluating the potential of phase-change optical disks. To measure the C/N of an optical disk, a monotone signal with a frequency f_1 is first recorded on an optical disk revolving at a constant linear velocity. Generally, f_1 corresponds to the minimum mark length (i.e., the highest recording density) to evaluate the resolution of the disk. Here, the exposed laser power is modulated between a peak power level P_p for amorphization and a bias power level for crystallization P_b (Fig. 11.88). The DC laser beam is shone on the recorded track at low power to read-out the recorded signal. The reflectivity of the optical disk dif-
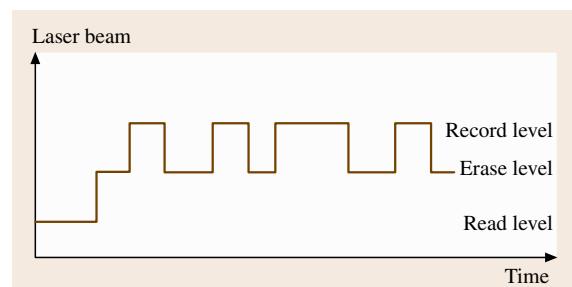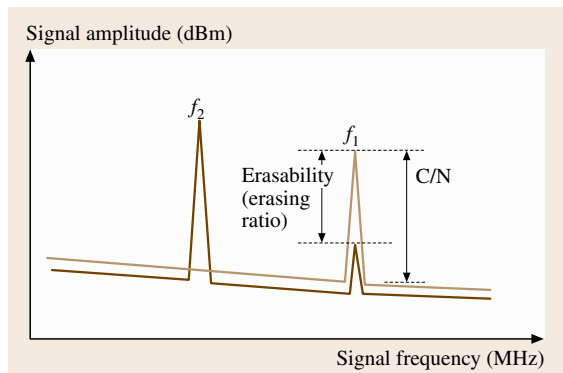

Fig. 11.88 Representative laser-modulation scheme for overwriting on a phase-change optical disk using only one laser beam

fers between the amorphous and crystalline portions; accordingly, the recorded signals are detected as the variation of the reflection light intensity from the optical disk. The C/N ratio is determined by the ratio of the averaged signal amplitude and the noise floor at the frequency f_1, as shown in Fig. 11.89. Usually, the above operations are carried out using a spectrum meter by stepping up the exposed laser powers, and the saturated value is determined as the C/N ratio of the optical disk. It is said that 45 dB is the usual minimum limit for a digital recording. The laser power to achieve saturation is determined by the recording power, as shown. To rewrite the data, another monotone signal with a frequency f_2 is overwritten on the recorded signal track, and the attenuation ratio of the signal amplitude of f_1 is determined to be the erasability. It is generally said that the erasability should be at least 20–26 dB to avoid influencing the quality of the overwritten signal.

The signal amplitude, noise level, and erasability are tightly related to the optical changes of the material, film quality such as surface flatness and grin size, and crystallization properties such as the crystallization rate, respectively.

Jitter and BER. In recent optical disks, signal marks with various lengths, for example from 1.5 to 4 T with a resolution of 0.5 T (where T is the clock period) are recorded as digital signals on an optical disk, and information is put at every distance from a certain mark-edge to the neighboring mark-edges. Figure 11.90 shows a schematic model of the digital recording signals. As can be seen from the figure, inhibition of the mark-edge deviation is important for increasing signal quality; an error occurs if the deviation becomes over half of the clock period T. To increase the record-

ing density, the mark length and space length has to be as short as possible. However, this is thermally restricted since the phase-change mechanism is a heat-mode process. This means that the desired thermal conductivity of phase-change films is lower than that of metals metals. Jitter is measured using a time-interval analyzer.

BER is the most important index to evaluate the disk performance for digital recording. It is measured by comparing the source signal and readout signal one by one. In the case of computer uses, an error rate of $10^{-3}–10^{-4}$ is the minimum level.

Reliability

Reliability is naturally one of the most important factors for industrial materials. In particular, the highest level of reliability is intrinsically required for memory devices. In the case of phase-change optical memory, reliability includes the thermal stability of the amorphous state and the chemical stability of the material itself. Both factors are usually evaluated through accelerated environmental tests based on Arrhenius's equation (11.123).

$$K = A \exp\left(-\frac{E}{RT}\right) \quad \text{or}$$

$$\ln(k) = -\frac{E}{R}\frac{1}{T} + \ln A , \tag{11.123}$$

where K, A, E, R and T are the reaction rate constant, frequency factor, activation energy, gas constant and environmental temperature, respectively.

The equation gives an estimation of the chemical reaction speed at a certain temperature. It is seen that the rate of chemical reaction becomes large as the temperature increases. The right-hand side of the equation means that the logarithm of K varies lin-

Fig. 11.89 Measurement scheme of C/N using spectrum analyzer
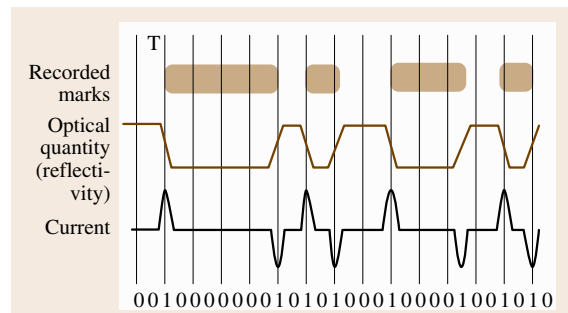
Fig. 11.90 Schematic of the mark-edge recording-reproducing method. Signal 1 is applied on positions where reflectivity drastically changes
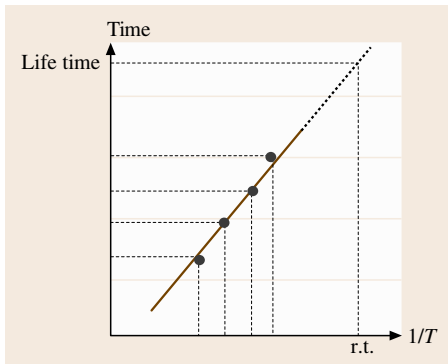
Fig. 11.91 Schematic of Arrhenius plot for obtaining an estimated life at room temperature (r.t.) based on the Arrhenius equation

early with $1/T$ on a logarithmic graph. Accordingly, it is possible to obtain the activation energy for the chemical reaction as the gradient of the straight line. The straight line is drawn based on the least-squares method by plotting the test results at various temperatures. By extrapolating the relation to room temperature, an estimated life under practical conditions can be obtained.

Figure 11.91 shows a schematic example of an Arrhenius plot. In the figure, the vertical axis shows the time for -3 dB of C/N. By extrapolating the straight line to 30 °C, the estimated life of this optical disk is determined to be more than 50 years. The vertical axis can be arbitrarily selected to BER, reflectivity, amplitude and noise level etc. as required. The acceleration condition can also be selected in a number of ways. In the case of optical disks, the acceleration test is usually carried out under high-humidity conditions such as 70 or 80% RH in order to evaluate moisture resistance.

11.6.2 Evaluation Technologies for MO Materials

To evaluate magnetooptical memory materials, the investigation of their magnetic characteristics is the most important. Of course, thermal and optical properties are not disregarded; however, broadly speaking, these parameters are only important in relation to the magnetic properties. Items that are common to the phase-change technologies are omitted here.

R&D History of MO Materials

Research into MO recording was started by *Williams* in 1957 [11.177]. He recorded a signal on an MnBi magnetic film using a magnetic pen and observed the recorded magnetic domain based on the MO effect. The following year, *Mayer* formed similar magnetic domains using a thermal pen. This fact became the origin of so-called thermal-magnetic recording [11.178]. There was a short break before *Chang* first reported thermal-magnetic recording using a laser beam in 1965. This became the prototype of present MO recordings [11.179]. From that point, various studies have been carried out to search for memory materials suitable for MO recording. Finally, in 1973, *Chaudhari* et al. found a good MO material based on the rare-earth transition-metal (RE-TM) system [11.180]. It is known that the RE-TM material system has the following superior characteristics

1. the film noise is intrinsically low since the film is used in its amorphous state,
2. the perpendicular magnetization is easily formed, and a large MO effect is obtained,
3. a plastic substrate can be adopted since it does not require thermal treatment, and
4. the recording properties can be freely optimized since it is a ferrimagnetic material.

Today, various RE-TM materials are formed combining from heavy-earth elements such as Ge, Tb and Dy and the transition-metal elements Co and Fe. These have been adopted for the memory layer of all the commercialized MO disks without exception. RE-TM materials are characterized by their magnetically continuous structure, as opposed to the gradual structure of usual magnetic materials used in their crystal state.

Evaluation and measurement methods for MO technology are described below, as relevant to their application to RE-TM materials for memory layers.

Principle of MO Recording

The principle of MO recording is explained using Fig. 11.92. Before recording, the direction of the perpendicular magnetization is aligned to one direction by globally applying an intense magnetic field. At this time, the film is instantly heated, which is usually achieved with a flash lamp. The MO film has a large coercive force and a very intense magnetic field is necessary to change the direction of the magnetic field at room temperature. However, the coercive force of a magnetic material is lowered when the film temperature is increased.

Utilizing this phenomenon, we use both a laser beam and an external magnetic field for recording. One

method is optical modulation. Here, the laser power is modulated according to the recording data under a constant magnetic field. Since the laser beam instantly heats the magnetic film to the Curie point, the heated areas change their magnetization direction. When erasing the data, DC laser exposure is applied to align the magnetization in the same direction. A second method is magnetic-field modulation. Here, a magnetic coil is used to make a modulation field while DC laser exposure is applied. In this case, the direction of the magnetization is changed according to the magnetic field formed by the magnetic coil. In this case, recording and erasing is carried out simultaneously and the erase process is not necessary.

For both cases, the Kerr effect is used to read the recorded data. When polarized light is incident on a polarized magnetized film, the polarization plane of the reflected light is slightly revolved from that of the incident light, and the revolution direction changes with the magnetization direction.

Fundamental Magnetic Properties

The most fundamental and important parameters for evaluating MO films are the dependence of the magnetization and magnetooptical effects on the magnetic field. Though the size of the magnetization itself is not a parameter that directly influences the record–reproduce characteristics, the value of the magnetization is indispensable for the analysis of the mechanism of magnetic reversal. On the other hand, the size of the magnetooptical effect, which is the reproducing mechanism itself, directly impacts on the record–reproduce characteristics.

Magnetization. There are various types of magnetometers, a device that measures magnetization directly. For example, i) those that observe the temporal variation of the magnetic flux produced by a magnetic body, ii) those which measure the force applied to a magnetic body placed in a magnetic field gradient, iii) those which measure the alternating force applied to a magnetic body placed in an alternating magnetic field, and iv) vibrating sample magnetometers (VSM), which measure the electromotive force produced in a detection coil placed beside a vibrating sample in a magnetic field. The last of these has become the standard method and almost all magnetic-film institutes provide this measurement equipment. Nowadays, various types are commercially available and the fundamental procedures for gathering data, analysis and the sweeping of the magnetic field are built into a microcomputer as a measuring program and measurements are automated.
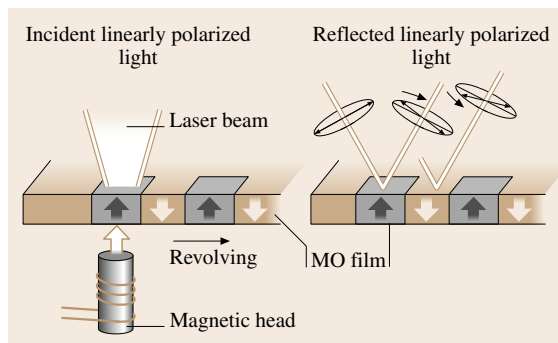

Fig. 11.92 Recording (*left*) and read (*right*) principle of MO disk

MO Effect and the Curie Point. As described above, the Kerr effect is a very important property for MO recording materials. For the evaluation of the magnetooptical effect, we measure the angle through which the polarization plane of linearly polarized light is turned on vertical incidence to a specimen in a magnetic field. In the practical polar Kerr magnetometer, a hysteresis loop is drawn by sweeping the magnetic field. Various types of this magnetometer have been commercialized, and the fundamental procedures of data gathering, analyses and the sweeping mode of the magnetic field are automatized. It is known that the magnetooptical effect depends strongly on the optical wavelength. For the evaluation of the wavelength dependence, equipment that can cover a wide wavelength range from the ultraviolet to the infrared has been developed and commercialized [11.181].

The Curie point is an important factor that is closely relating to the recording sensitivity of MO disks. This value can be obtained by measuring the thermal dependence of the magnetization and the Kerr rotation angle at temperatures varying from the ferromagnetic to the paramagnetic state. The measurements are carries out using the VSM and a Kerr magnetometer with a heating mechanism and thermal monitoring capability.

Perpendicular Magnetic Anisotropy. It is also important to measure a perpendicular magnetic anisotropy, K_u, in order to discuss the magnetic reversal phenomenon. K_u is calculated from the contortion value of a wire that supports the sample in the revolving magnetic field. The contortion is calibrated to the torque produced in the sample. The torque-meter is usually equipped with an VSM. The fundamental evaluation methods for the magnetic characteristics are overviewed above. However, in recent years, several new technolo-

gies have been proposed. These include, for example, laser-modulation overwrite technologies [11.182, 183] and magnetic super-resolution technologies [11.184–189] utilizing the mutual interaction between a number of magnetic films with deferent thermal properties. In order to evaluate the new technologies, the magnetic cohesion between layers become an important parameter in addition to the aforementioned material properties. An effective method is to compare the hysteresis curves among stacked layers and each layer separately, and observe the magnetic field change required for magnetic reversal [11.188].

Observation of Magnetic Domains. Polarized optical microscopes were used for the observation of magnetic domains until the 1980s, but since then the magnetoforce micrometer (MFM) has been used to meet this demand [11.190–197]. This is because the polarized microscope is not good at observing with at higher resolving powers. Additionally, the polarization plane becomes unaccepted as the reflectance of the p-polarized and s-polarized light starts to differ with increasing objective-lens curvature.

Dynamic Recording Properties

The same set-up as a commercial MO disk drive is applied for evaluating the recording–reproducing properties of MO materials. Here, C/N, jitter and BER are measured as for the aforementioned phase-change materials.

Reliability

In order to evaluate the lifetime of MO materials, a similar method as for phase-change materials is applicable. Accelerated environmental tests are performed at several temperatures around $60–90\,°C$, and the lifetime at room temperature can be estimated based on the Arrhenius plot. This method has frequently been used at the first stage of MO disk development, and has resulted in an ideal structure using SiN protective layers on both sides of MO layer. Almost all commercial MO disks have adopted a multilayer structure today. Of course, it is natural that this evaluation procedure should be performed when a new MO disk utilizing new materials is developed.

Another important item is the read-power tolerance. Firstly, this is because the magnetic domain size tends to be smaller in recent high-density MO disks. In addition, new super-resolution technologies such as domain-wall displacement detection (DWDD) [11.198] and the magnetic amplifying magnetooptical system (MAM-MOS [11.199]) require high temperatures (i. e., high read powers) to produce the super-resolution mechanism. It is generally known that the coercive force decreases as the magnetic domain size becomes smaller or as the temperature of the magnetic domain becomes higher. To measure the read stability, it is necessary to examine the relation between read laser power and read cycle number and experimentally determine the read power that does not produce degradation. It is said that tolerance to at least one million passes is necessary.

11.7 Optical Sensing

11.7.1 Distance Measurement

Distance is defined as *the length of the space between two points* and sometimes means simply *the full length*. The optical distance meter is mainly based on: 1) triangulation measurement, 2) pulse time-of-flight, or 3) amplitude modulation telemetry. The performance of these methods are summarized in Table 11.12.

Triangulation

Let us observe a target from two points that are d apart, as shown in Fig. 11.93. Then the distance L can be calculated as

$$L = \frac{d}{\tan\theta} \, , \tag{11.124}$$

where θ is the tilt angle. This method has been applied to measurements ranging from millimeters to hundreds of kilometers. Our vision system senses a distance from the body to the target by the same method, where d corresponds to a distance between the two eyeballs. The change of θ is detected by a strain gauge namely the *muscle spindle* that is mounted in the eyeball control muscles, as shown in Fig. 11.94.

Time–of–Flight Measurement

The round-trip transit time (Δt) for a very short high-power pulsed light from a device such as a Q-switched solid-state laser is measured. The distance L from the light source to the target is given by

$$L = \frac{c\Delta t}{2} \, , \tag{11.125}$$

Table 11.12 Comparison of the performance of triangulation measurements, pulse time-of-flight, and amplitude-modulation telemetry

Method	Typical light source	Typical range	Typical accuracy	Applications
Triangulation	Passive light, light source unnecessary	mm to hundreds of km	10^{-6}	Auto-focusing camera, survey
Time-of-flight	Q-switched laser, pulsed diode laser	mm to km	10^{-5}	Military range finding, satellite ranging
Amplitude modulation	He–Ne laser, diode laser	sub-mm to km	10^{-6}	Survey
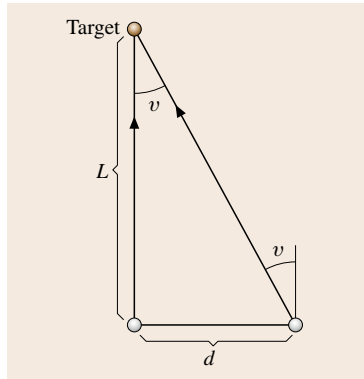
Fig. 11.93 Triangulation distance measurement

where c is the light speed in the measurement medium. In the actual measurement, the transit time (Δt) is measured with a time-base counter or a time-to-amplitude converter. A time resolution better than 6 ps is required to resolve 1 mm in length. A distance meter that can resolve 1 mm is achieved using a conventional time-base instrument and a pulse-driven diode laser [11.200]. Although the resolution of time-of-flight method is somewhat low, measurement is rapid. Therefore this method is usually applied to military range-finding in combination with a laser radar.
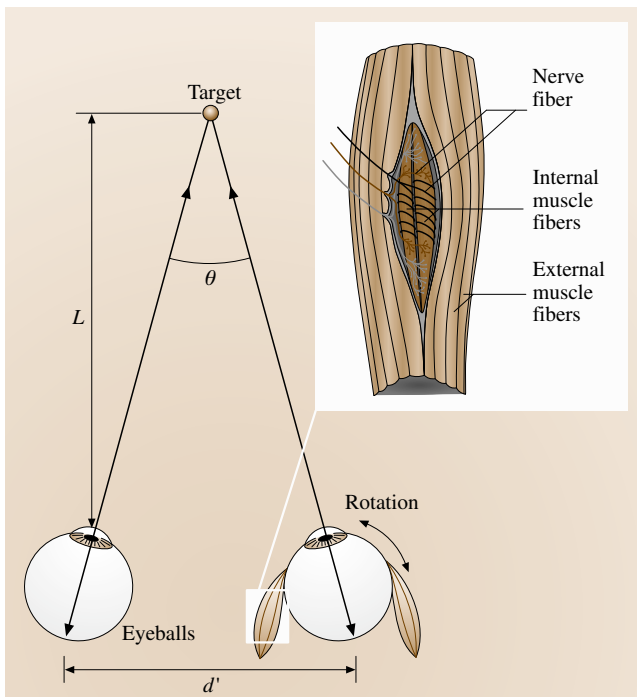
Amplitude Modulation

The amplitude of a stationary light source is sinusoidally modulated by modulation of the driving current with frequency of f (Hz). The wavelength of the modulation (Λ) is

$$\Lambda = \frac{c}{f} . \tag{11.126}$$

The distance L is given by

$$L = \frac{\Lambda}{2}\left(N + \frac{\phi}{2\pi}\right) , \tag{11.127}$$

where ϕ (rad) is the phase difference between the light source and the detected light (see Fig. 11.95), and N is an integer ($N = 0, 1, 2, 3, \ldots$). The value of L is simply determined by ϕ when Λ is smaller than $L/2$, but several possible values exist when Λ is larger than $L/2$. In that case, light with different modulation frequencies is additionally used to determine N. An optical laser distance meter using a variable frequency, a sinusoidally modulated He–Ne laser and a precision phasemeter enables measurement distances of as much as 50 km. A portable version with a diode laser and a photodiode as the light source and detector, respectively, can measure distances of up to a few kilometers with an error of 5 mm. Precise distance measurement requires high-frequency no-distortion sinusoidally modulated light. For this purpose, an intermode beat signal of 1 GHz

Fig. 11.94 Triangulation distance sensing by human eyes
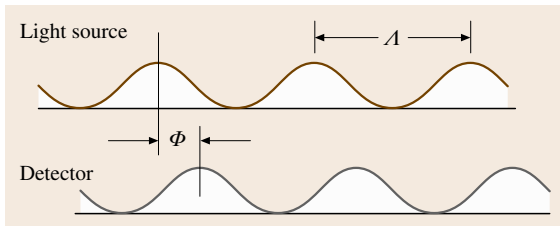
Fig. 11.95 Distance measurement by amplitude modulation

generated in a frequency stabilized two-mode He–Ne laser has been utilized [11.201].

11.7.2 Displacement Measurement

A displacement measurement means the measurement of the movement of a point from one position to another, and often requires very accurate length measurement. There are various types of optical instruments, i.e., microscope-based measurement, an optical lever in combination with a mechanical measurement, and triangulation-based methods. In consideration of the very accurate noncontact displacement measurement, a light interferometer is commonly used. A typical set-up called a Michelson interferometer is shown in Fig. 11.96a. Monochromatic light of wavelength λ from a light source such as a laser is collimated onto the beam splitter BS that reflects half of the light towards the flat mirror M and allows transmission of the other half toward the work piece W. Both beams are recombined at BS and transmitted to the screen, resulting in the formation of interference fringes. Fringes appear and disappear when the optical path length of the two beams Δ is an even and odd multiple of λ/2, respectively, as shown in Fig. 11.96b. There are several variations of the interferometer optics configuration such as the Fizeau interferometer, Twyman–Green interferometer, Kösters interferometer, Mach–Zehnder interferometer, and Dyson interferometer [11.202].

A simple combination of fiber optics and photodetector depicted in Fig. 11.97 can be applied effectively to displacement measurements from the submicrometer range to several tens of centimeters. Such equipment is commercially available, and its typical sensitivity and resolution are 13 nm/mV and tens of nanometers, respectively, up to 60 μm.

11.7.3 3–D Shape Measurement

For noncontact profile measurement, photographs using an electric imaging device such as a CCD camera are
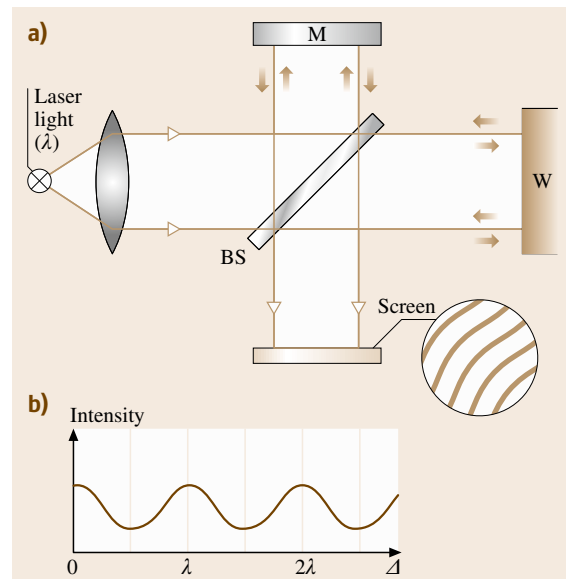
Fig. 11.96a,b Schematic of Michelson interferometer: (a) optics configuration and typical fringe profile on the screen, (b) change of fringe brightness with respect to the optical path length between the two beams
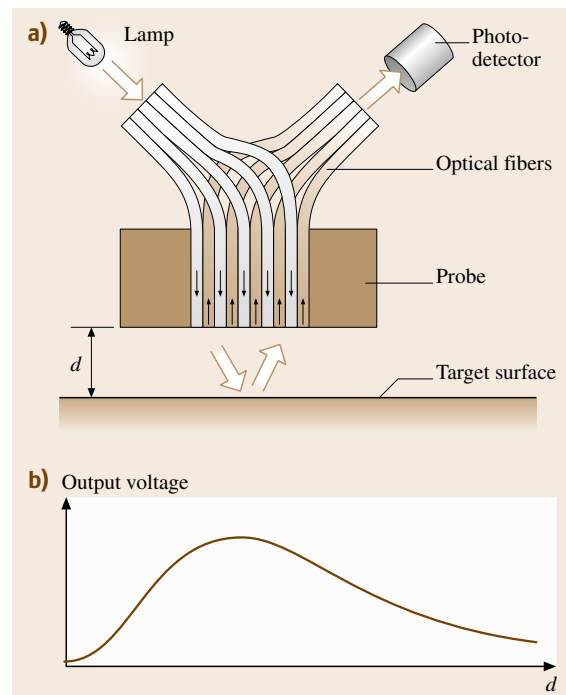
Fig. 11.97a,b Fiber-optic displacement transducer: (a) optics configuration, (b) typical output profile

Table 11.13 Comparison of the performance of typical 3-D measurement methods

Method	Features	Applications
Stereo-photograph	High accuracy, for large scale object, expensive	Map, large building, survey
Optical sectioning	Simple construction, enable from small size to large size object, changeable sensitivity	Car body, industrial parts
Moiré topography	Simple construction, high reliability, moderate sensitivity	Car body, human body
Holograph	High sensitivity, for small size object	Small parts

still dominant. The 3-D measurement can be done with the use of two cameras taking stereo images. Accurate 3-D measurement is made simply by combination of a light sheet and a CCD camera, as shown in Fig. 11.98. This method is one application of the triangulation measurement and is called optical sectioning. To reconstruct the 3-D profile, scanning of the light sheet and/or irradiation of a grating sheet light with an adequate binary (black and white) data treatment by the signal level discrimination are combined. A moiré topography and holographic technique are also widely applied. The features and typical applications of these methods are summarized in Table 11.13.

11.7.4 Flow Measurement

Flow visualization are based on two basic schemes: a) association of tracer particles and b) detection of changes in fluid optical properties caused by flow change.
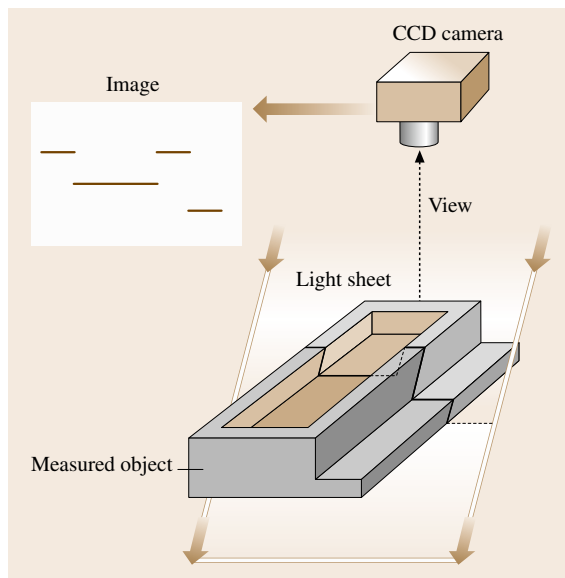
Fig. 11.98 Optical sectioning by light sheet and CCD camera

Tracer–Particle Image Velocimeter

The flow direction and the velocity of each tracer particle in the liquid can be informed by applying a repetitive stroboscopic light illumination for photographic measurement. Colored dyes and gas bubbles are the common tracers and this technique is known as tracer-particle image velocimetry. When the color of the tracer particle changes with temperature, both temperature and velocity mapping are completed simultaneously. For this purpose, a temperature-sensitive liquid crystal is used as the tracer.

Laser Doppler Velocimeter

For tracer-particle associated flow measurement, a laser Doppler velocimeter (LDV) based on the Doppler shift plays an important role. The frequency of light scattered by a moving object changes depending on the velocity of the object and the scattering geometry. Advantages of LDV are the very high-frequency response (to MHz range) and sensing of very small measurement volumes (smaller than $0.1\,\text{mm}^3$), while disadvantages are the point nature of the measurement, the requirement for tracer particles, and the high cost and complexity of the apparatus. The particles are not always necessary, because microscopic particles are normally contained in the measurement liquid, e.g., corpuscles in blood. However, gas flow often needs to be seeded. Figure 11.99a shows a popular dual-beam (or differential Doppler) configuration. Though the relationship between the velocity V of the particle moving and the frequency f of the electric signals is introduced by the Doppler shift, the interference fringe explanation depicted in Fig. 11.99b is rather useful in this case. The two crossing light beams form the fringe pattern with a fringe interval of

$$\delta = \frac{\lambda}{2\sin\left(\frac{\theta}{2}\right)}\,, \tag{11.128}$$

where λ is the wavelength of the light in the fluid and θ is the angle between the two converging beams. A moving particle crossing the dark and light fringe pattern produces a sinusoidally modulated electric signal with

a modulation frequency f given by

$$f = \frac{V}{\delta}$$
$$= \frac{2V \sin\left(\frac{\theta}{2}\right)}{\lambda} . \tag{11.129}$$

Flow Visualization

The density of the fluid varies with velocity, resulting in a variation in its refractive index. Shadowgraph and schlieren techniques employ this variation in the refractive index. In these methods, light and dark patterns related to the velocity are made by the bending of light rays as they pass through a region of varying density. Because the optical set-ups of these two methods are simple, they are widely utilized for qualitative studies. For quantitative measurement, the Mach–Zehnder interferometer shown in Fig. 11.100a is advantageous. The light and fringe patterns (Fig. 11.100b) are formed by the interference between the reference beam and the measured beam. The regular light/dark fringes are displayed even for no flow. The fringe profile partially distorts according to the change of the optical length caused by changes in the refractive properties of the fluid medium when appreciable flow occurs. The appearance of fringes on the screen can then be directly related to changes in density in the flow field. The features of these three methods are summarized in Table 11.14.

11.7.5 Temperature Measurement

Temperature measurement is based on the following three methods: 1) blackbody radiation, 2) temperature-dependent-color material, and 3) other spectroscopic methods.

Blackbody Radiation

Any substance at a temperature above 0 K emits radiation. The theory of this radiation is well explained using an ideal emitter called a blackbody. Figure 11.101 shows the change of the emission profile of the blackbody as a function of wavelength λ and temperature T (K). This profile follows the Planck distribution equation,

$$L_{\lambda,T} = \frac{C_1}{\lambda^5}\left(\frac{1}{e^{C_2/\lambda T} - 1}\right) , \tag{11.130}$$

where $L_{\lambda,T}$ is the emitted monochromatic blackbody power, and C_1 and C_2 are the Planck emission constants. As one can see, the wavelength corresponding to the maximum energy moves both toward higher energies and shorter wavelengths with increasing temperature.
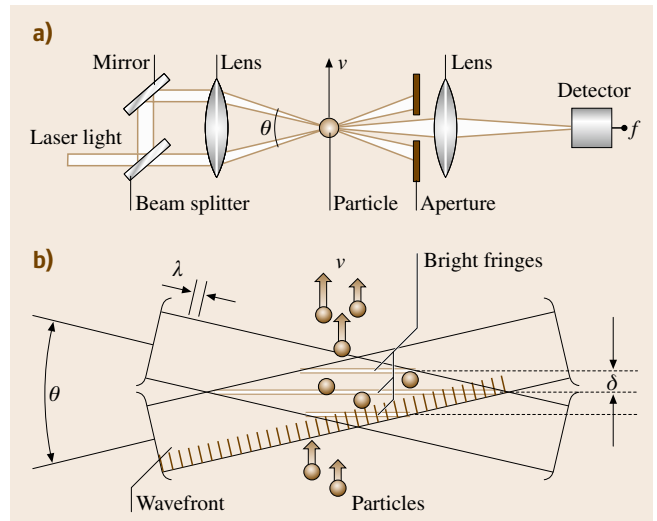

Fig. 11.99a,b Dual-beam laser Doppler velocimeter: (**a**) schematic of configuration, (**b**) interference fringes formed by the two beams
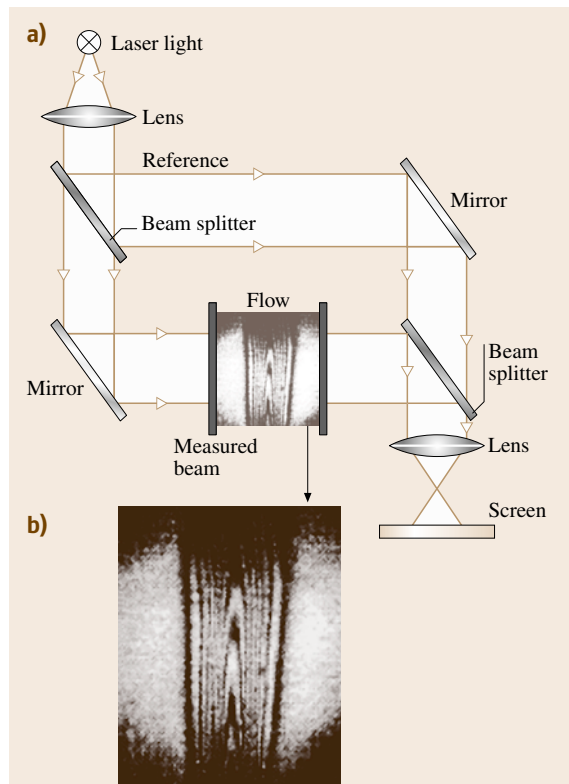

Fig. 11.100a,b Mach–Zehnder interferometer for flow visualization: (**a**) optics configuration, (**b**) example of the visualized flow (thanks to Prof. H. Kimoto, Osaka Univ.)

Table 11.14 Comparison of performance of shadowgraph, the schlieren technique and a Mach–Zehnder interferometer for flow visualization

Method	Light source	$\Delta I/I$ is proportional to
Shadowgraph	Continuous wavelenght light, CW laser	Gradient of $\mathrm{d}p/\mathrm{d}y$
Schlieren	Continuous wavelength light, CW laser	Gradient of p
Mach–Zehnder	Monochromatic light is neccessary, e.g., CW laser	Fluid density p

The total thermal radiation power E (W) emitted by a blackbody with unit surface area (1 m^2) at a temperature T is given by the integration of $L_{\lambda,T}$ over λ, resulting in

$$E = \sigma T^4 , \tag{11.131}$$

where σ is the Stefan–Boltzmann constant (5.6704×10^{-8} W/(K^{4}m^2)).

The wavelength at the maximum emitted power λ_{max} can be obtained by derivation of $L_{\lambda,T}$ by λ. The relationship between λ_{max} (μm) and T is given by Wien's law as

$$\lambda_{\mathrm{max}} T = 2897.6 \, \mu\mathrm{m}\,\mathrm{K} . \tag{11.132}$$

However, spectral profiles of the actual materials may vary from that of a blackbody (they may exhibit lower emission in some wavelength), and these are called graybodies. The temperature of the blackbody can thus be estimated by the measurement of either the total emitted thermal energy, the wavelength of maximum emitted power, or the spectral profile of the emission. Several methods are available to measure the emitted energy and/or spectral profiles with appropriate optical sensors.
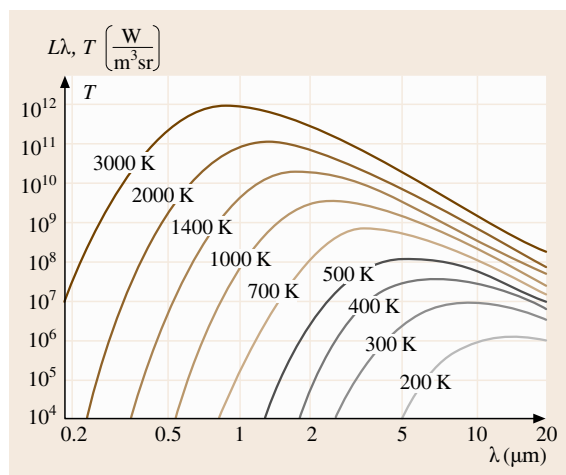
Fig. 11.101 Emission profile of a blackbody as a function of wavelength and temperature

These methods are called optical pyrometry. A typical scheme for the pyrometer is shown in Fig. 11.102, where the standard lamp is placed in the optical path of the incident radiation. By adjusting the lamp current, the color of the filament is made the same as that of the incident radiation. Because the temperature is calibrated via the lamp heating current, the temperature of the radiation can then be estimated from the lamp current.

Temperature–Dependent–Color Material

Microcapsules that envelope temperature-depend-color liquid crystals are prepared. Because the color of the capsule changes with temperature, the surrounding temperature can be determined by the color of the capsule. The merit of this method is that it allows the simultaneous determination of both the temperature and its distribution (see the tracer-particle image velocimeter). However, the measurable temperature range is fairly narrow, i.e., from room temperature to 50 °C. A laser-induced fluorescence (LIF) method extends the measurable temperature to 1000 °C [11.203]. In LIF, an appropriate fluorescent material whose fluorescence intensity and/or fluorescence lifetime change with temperature is used.

Coherent Anti–Stokes Raman Spectroscopy

The infrared light region reflects the state of the molecular vibration energy. Because the population of the molecular vibrational and rotational states depends on
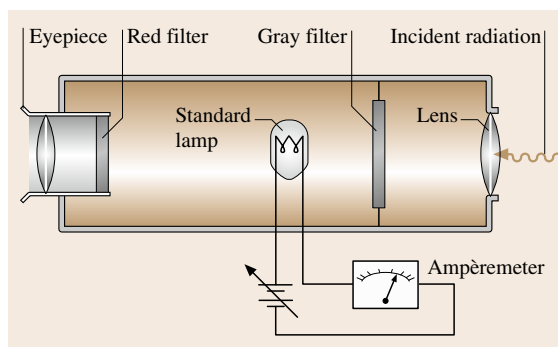
Fig. 11.102 Scheme for optical pyrometer

temperature, the temperature of a gas molecule can be determined directly by appropriate infrared spectroscopy. Among the various spectroscopic techniques, a coherent anti-Stokes Raman spectroscopy (CARS) is attractive and has been applied to gas temperature monitoring [11.204].

Another advantageous application of CARS is the identification of analytical molecules. For this purpose, a CARS microscope has been proposed [11.205].

11.7.6 Optical Sensing for the Human Body

The important features of the optical method are that it is rapid, noninvasive and safe. These features are useful for measurements in health care and for medical examination of the human body.

Body Temperature and Thermograph
Body temperature monitoring is the most essential examination in health care. It can typically be monitored within $0.1-0.3$ s using an infrared ear thermometer, which measures the infrared energy emitted from the eardrum. A short tube with a protective sleeve is inserted into the ear, and a shutter is opened to allow in radiation from the tympanic membrane.

A thermograph is a picture of the heat levels in the body. It is measured with an infrared imaging system that detects infrared radiation from the body's surface. Since some disorders such as breast cancer or soft-tissue injuries have a very high metabolism, they are slightly hotter than the surrounding normal tissues and can therefore be detected by the thermograph. The other technique is based on liquid crystal (LC) technology. It provides a color map of temperature. Spraying or painting the skin with LC materials displays temperature as different color bands.

Body Contours
Optical sectioning and moiré topography are widely employed to body shape measurement. In clinical applications, spinal faults and progress of their treatment is monitored by so-called moiré contourography, which highlights body contours [11.206]. The moiré contours are obtained by passing angled light through a grid onto the surface of the body.

Retina Examination
Optical coherent tomography (OCT) is a noncontact, noninvasive imaging technique used to obtain high-resolution cross-sectional images of optically transparent materials [11.207]. OCT achieves much greater longitudinal resolution (approximately $10\,\mu m$) than ultrasonic examination, and is thus clinically useful for local imaging of selected macular diseases including macular holes, macular edema, age-related macular degeneration, central serous chorioretinopathy, epiretinal membranes, schisis cavities associated with optic disc pits, and retinal inflammatory diseases. In addition, OCT has the capability of measuring the retinal nerve fiber layer thickness in glaucoma and other diseases of the optic nerve. LDV [11.208] (Sect. 11.7) and laser-speckle flowgraphy [11.209] are also applied for blood-flow determination in the retina.

Pulse Oximetry
Pulse oximetry is an optical method to monitor the hemoglobin (Hb) concentration of arterial blood that is saturated with oxygen [11.210]. The absorption profiles of oxy-Hb and deoxy-Hb show absorption peaks at around 920 and 750 nm, respectively. Therefore, the relative amount of oxy-Hb can be determined by measurement of light absorption in the near-infrared region. The pulse oximeter consists of an optical probe attached to the patient's finger or ear lobe which outputs an absorption signal corresponding to Hb and a computerized signal-processing unit. The unit displays the percentage of Hb saturated with oxygen together with an audible signal for each pulse beat. A reflection-type pulse oximeter that increases the flexibility of installation has been developed [11.211].

Brain Optical Topography
As described in the former section, the concentration of Hb in the artery can be determined optically. Since near-infrared light is transmitted through biological tissues including bones easily, local Hb concentration topography has been achieved optically to analyze functions of the brain [11.212]. To achieve brain topography, multiple pairs of light sources and a detector are placed around the head.

Skin Spectroscopy
Skin spectroscopy provides useful information for skin diagnosis. For example, the oxygen saturation of blood and melanin in the skin can be determined by the measurement of a skin spectral reflectance image and the application of component analysis [11.213]. LDV is also applied to skin diagnosis, for example, burn depth has been determined by a laser Doppler imager [11.214]. Second-harmonic generation (SHG) occurs at appreciably levels when collagen is irradiated with intense short-duration pulsed light if the polarization direction of the

incidence light wave is consistent with the collagen fiber orientation [11.215]. This feature has been applied effectively to the determination of collagen fiber orientation in the human dermis [11.216]. The characteristics of a terahertz electromagnetic wave (THz wave) are situated at the boundary between light and radio waves, and these features of THz waves has been applied to the detection of skin cancer and hydration level [11.217]. We recommend the articles on optics of the human skin published in 2004 for further study [11.218].

Glucose Monitoring

Noninvasive, in vivo optical glucose monitoring is one of the most important measurements to be achieved for human health care and diagnosis. However, the analytical probe light is strongly scattered by the skin and blood cells, resulting in a decrease in measurement reliability. This noninvasive measurement is successful at present only when applied to aqueous humor, which the probe light can reach through the cornea without unwanted scattering [11.219].

References

11.1   A.P. Thone: *Spectrophysics*, 2nd edn. (Chapman Hall, New York 1988)

11.2   J.D. Ingle Jr., S.R. Crouch: *Spectrochemical Analysis* (Prentice Hall, Piscataway 1988)

11.3   H.H. Willard, L.L. Merritt Jr., J.A. Dean, F.A. Settle Jr.: *Instrumental Methods of Analysis*, 7th edn. (Wadsworth Publishing, Belmont 1988)

11.4   G.W. Ewing: *Instrumental Methods of Chemical Analysis*, 4th edn. (McGraw-Hill, Tokyo 1975)

11.5   T. Iwata, T. Tanaka, T. Araki, T. Uchida: Externally-controlled nanosecond Xe discharge lamp equipped with a synchronous high-voltage power supply using an automobile ignition coil, Rev. Sci. Instrum. **73**(9), 3165–3169 (2002)

11.6   T. Iwata, T. Tanaka, T. Komatsu, T. Araki: An externally-controlled nanosecond-pulsed, Xe lamp using a high voltage semiconductor switch, Rev. Sci. Instrum. **71**, 4045–4049 (2000)

11.7   E. Miyazaki, S. Itami, T. Araki: Using a light-emitting diode as a high-speed, wavelength selective photodetector, Rev. Sci. Instrum. **69**, 3751–3754 (1998)

11.8   T. Araki, H. Misawa: LED-based nanosecond UV-light source for fluorescence lifetime measurements, Rev. Sci. Instrum. **66**, 5469–5472 (1995)

11.9   T. Araki, Y. Fujisawa, M. Hashimoto: An ultraviolet nanosecond light pulse generator using a light emitting diode for test of photodetector, Rev. Sci. Instrum. **68**, 1365–1368 (1997)

11.10 T. Iwata: Proposal for Fourier-transform phase-modulation fluorometer, Opt. Rev. **10**(1), 31–37 (2003)

11.11 T. Iwata, T. Takasu, T. Miyata, T. Araki: Combination of a gated photomultiplier tube and a phase sensitive detector for use in an intensive pulsed background situation, Opt. Rev. **9**, 18–24 (2002)

11.12 T. Iwata, T. Takasu, T. Araki: Simple photomultiplier-tube internal-gating method for use in sub-nanosecond time-resolved spectroscopy, Appl. Spectrosc. **57**, 1145–1150 (2003)

11.13 T. Miyata, T. Araki, T. Iwata: Correction of the intensity-dependent phase delay in a silicon avalanche photodiode by controlling its reverse bias voltage, IEEE J. Quantum Electron. **QE–39**, 919–923 (2003)

11.14 T. Miyata, T. Iwata, T. Araki: Construction of a pseudo-lock-in light detection system using a gain-enhanced gated silicon avalanche photodiode, Meas. Sci. Technol. **16**, 2453–2458 (2005)

11.15 P. Griffiths, J.A. de Haseth: *Fourier Transform Infrared Spectrometry* (Wiley, New York 1986)

11.16 J.M. Chalmers, P.R. Griffiths (Ed.): *Handbook of Vibrational Spectroscopy*, Vol.1 (Wiley, New York 2002)

11.17 M. Dressel, G. Grüner: *Electrodynamics of Solids* (Cambridge Univ. Press, Cambridge 2002)

11.18 M. Born, E. Wolf: *Principles of Optics: Electromagnetic Theory of Propagation, Interference and Diffraction of Light* (Cambridge Univ. Press, Cambridge 1999)

11.19 R.M.A. Azzama, N.M. Bashara: *Ellipsometry and Polarized Light* (North-Holland, Amsterdam 1977)

11.20 S. Uchida, T. Ido, H. Takagi, T. Arima, Y. Tokura, S. Tajima: Optical spectra of $La_{2-x}Sr_xCuO_4$: Effect of carrier doping on the electronic structure of the CuO_2 plane, Phys. Rev. B **43**, 7942–7954 (1991)

11.21 Y. Toyozawa: *Optical Processes in Solids* (Cambridge Univ. Press, Cambridge 2003)

11.22 M. Ashida, Y. Kawaguchi, R. Kato: Phonon sidebands of ν_{00} line in absorption and luminescence spectra of $NaNO_2$: Spatial dispersion of ν_{00} exciton, J. Phys. Soc. Jpn. **58**, 4620–4625 (1989)

11.23 Y. Kondo, T. Noto, S. Sato, M. Hirai, A. Nakamura: Hot luminescence and non-radiative transition of F centers in KCl and NaCl crystals, J. Lumin. **38**, 164–167 (1987)

11.24 I. Akimoto, M. Ashida, K. Kan'no: Luminescence from C_{60} single crystals in glassy phase under site-selective excitation, Chem. Phys. Lett. **292**, 561–566 (1999)

11.25 M. Cardona, G. Güntherrodt (Eds.): *Light Scattering in Solids I–VIII* (Springer, Berlin, Heidelberg 2000)

11.26 W. Hayes, R. Loudon: *Scattering of Light by Crystals* (Wiley, New York 1987)

11.27 E. Saitoh, S. Okamoto, K.T. Takahashi, K. Tobe, K. Yamamoto, T. Kimura, S. Ishihara, S. Maekawa, Y. Tokura: Observation of orbital waves as elementary excitations in a solid, Nature **410**, 180–183 (2001)

11.28 A. Kato, M. Ashida, R. Kato: Temperature dependence of resonant secondary emission in $NaNO_2$ crystals, J. Lumin. **66/67**, 264–267 (1996)

11.29 B.P. Zhang, T. Yasuda, W.X. Wang, Y. Segawa, K. Edamatsu, T. Itoh, H. Yaguchi, K. Onabe: A new approach to ZnCdSe quantum dots, Mater. Sci. Eng. B **51**, 127–131 (1998)

11.30 A.M. van Oijen, M. Ketelaars, J. Koehler, T.J. Aartsma, J. Schmidt: Unraveling the electronic structure of individual photosynthetic pigment-protein complexes, Science **285**, 400–402 (1999)

11.31 T. Fujimura, K. Edamatsu, T. Itoh, R. Shimada, A. Imada, T. Koda, N. Chiba, H. Muramatsu, T. Ataka: Scanning near-field optical images of ordered polystyrene particle layers in transmission and luminescence excitation modes, Opt. Lett. **22**, 489–491 (1997)

11.32 K. Matsuda, T. Saiki, S. Nomura, M. Mihara, Y. Aoyagi, S. Nair, T. Takagahara: Near-field optical mapping of exciton wave functions in a GaAs quantum dot, Phys. Rev. **91**, 177401 (2003)

11.33 H.C. Ong, A.S.K. Li, G.T. Du: Depth profiling of ZnO thin films by cathodoluminescence, Appl. Phys. Lett. **78**, 2667–2669 (2001)

11.34 K. Vanheusden, W.L. Warren, C.H. Seager, D.R. Tallant, J.A. Voigt, B.E. Gnade: Mechanisms behind green photoluminescence in ZnO phosphor powders, J. Appl. Phys. **79**, 7983–7990 (1996)

11.35 D.M. Bagnall, Y.F. Chen, Z. Zhu, T. Yao, S. Koyama, M.Y. Shen, T. Goto: Optically pumped lasing of ZnO at room temperature, Appl. Phys. Lett. **70**, 2230–2232 (1997)

11.36 K. Shinagawa: Faraday and Kerr effects in ferromagnets. In: *Magneto-Optics*, Vol. 128, ed. by S. Sugano, N. Kojima (Springer, Berlin, Heidelberg 2000) p. 137

11.37 M. Faraday: On the magnetization of light and the illumination of magnetic lines of force, Philos. Trans. R. Soc. **136**, 104–123 (1846)

11.38 J. Kerr: On rotation of the plane of polarization by reflection from the pole of a magnet, Philos. Mag. **3**, 321 (1877)

11.39 C. Gourdon, G. Lazard, V. Jeudy, C. Testelin, E.L. Ivchenko, G. Karczewski: Enhanced Faraday rotation in CdMnTe quantum wells embedded in an optical cavity, Solid State Commun. **123**, 299–304 (2002)

11.40 C. Gourdon, V. Jeudy, M. Menant, A.T. Le, E.L. Ivchenko, G. Karczewski: Magneto-optical imaging with diluted magnetic semiconductor quantum wells, Appl. Phys. Lett. **82**, 230–232 (2003)

11.41 M.R. Koblischka, R.J. Wijngaarden: Magneto-optical investigations of superconductors, Superconduct. Sci. Technol. **8**, 199–213 (1995)

11.42 P.E. Goa, H. Hauglin, M. Baziljevich, E. Il'yashenko, P.L. Gammel, T.H. Johansen: Real-time magneto-optical imaging of vortices in superconducting $NbSe_2$, Superconduct. Sci. Technol. **14**, 729–731 (2001)

11.43 M.A. Butler, S.J. Martin, R.J. Baughman: Frequency-dependent Faraday rotation in CdMnTe, Appl. Phys. Lett. **49**, 1053–1055 (1986)

11.44 D. Scalbert, J. Cernogora, C. Benoit à la Guillaume: Spin-lattice relaxation in paramagnetic CdMnTe, Solid State Commun. **66**, 571–574 (1988)

11.45 V. Jeudy, C. Gourdon, T. Okada: Impeded growth of magnetic flux bubbles in the intermediate state pattern of type I superconductors, Phys. Rev. Lett. **92**, 147001 (2004)

11.46 A. Cebers, C. Gourdon, V. Jeudy, T. Okada: Normal-state bubbles and lamellae in type-I superconductors, Phys. Rev. B **72**, 014513 (2005)

11.47 Y.R. Shen: *The Principles of Nonlinear Optics* (Wiley, New York 1984)

11.48 S.V. Popov, P.Y. Svirko, N.I. Zheludev: *Susceptibility Tensors for Nonlinear Optics* (Inst. Physics, London 1995)

11.49 D.L. Mills: *Nonlinear Optics Basic Concepts* (Springer, Berlin, Heidelberg 1998)

11.50 H. Kishida, M. Ono, K. Miura, H. Okamoto, M. Izumi, T. Manako, M. Kawasaki, Y. Taguchi, Y. Tokura, T. Tohyama, K. Tsutsui, S. Maekawa: Large third-order optical nonlinearity of Cu-O chains investigated by third-harmonic generation spectroscopy, Phys. Rev. Lett. **87**(4), 177401 (2001)

11.51 C. Rulliere (Ed.): *Femtosecond Laser Pulses* (Springer, Berlin, Heidelberg 2003)

11.52 M. Ashida, R. Kato: Resonant emission under excitation of isotopic level in $NaNO_2$, J. Phys. Soc. Jpn. **63**, 2808–2817 (1993)

11.53 A. Kato, M. Ashida, R. Kato: Time-resolved study of exciton thermalization in $NaNO_2$, J. Phys. Soc. Jpn. **66**, 2886–2892 (1997)

11.54 M. Ashida, H. Arai, O. Morikawa, R. Kato: Luminescence and superfluorescence-like emission from a thin layer of O_2^- centers in KBr crystal, J. Lumin. **72–74**, 624–625 (1997)

11.55 M. Kuwata, T. Kuga, H. Akiyama, T. Hirano, M. Matsuoka: Pulsed propagation of polariton luminescence, Phys. Rev. Lett. **61**, 1226–1228 (1988)

11.56 S. Kinoshita, H. Ozawa, Y. Kanematsu, I. Tanaka, N. Sugimoto, S. Fujiwara: Efficient optical Kerr shutter for femtosecond time-resolved luminescence spectroscopy, Rev. Sci. Instrum. **71**, 3317–3322 (2000)

11.57 T. Matsuoka, S. Saito, J. Takeda, S. Kurita, T. Suemoto: Overtone modulation and anti-phasing behavior of wave-packet amplitudes on the adi-

abatic potential surface of self-trapped excitons, Nonlinear Opt. **29**, 587–593 (2002)

11.58   M. Ashida, T. Ogasawara, N. Motoyama, H. Eisaki, S. Uchida, Y. Taguchi, Y. Tokura, H. Ghosh, A. Shukla, S. Mazumdar, M. Kuwata-Gonokami: Interband two-photon transition in Mott insulator as a new mechanism for ultrafast optical nonlinearity, Int. J. Mod. Phys. B **15**, 3628–3632 (2001)

11.59   M. Ashida, T. Ogasawara, Y. Tokura, S. Uchida, S. Mazumdar, M. Kuwata-Gonokami: One-dimensional cuprate as a nonlinear optical material for ultrafast all-optical switching, Appl. Phys. Lett. **78**, 2831–2833 (2001)

11.60   M. Sheik-Bahae, A.A. Said, T.-H. Wei, D.J. Hagan, E.W. Van Stryland: Sensitive measurement of optical nonlinearities using a single beam, IEEE J. Quantum Electron. **QE-26**, 760–769 (1990)

11.61   N. Peyghambarian, S.W. Koch, A. Mysyriwicz: *Introduction to Semiconductor Optics* (Prentice Hall, Piscataway 1993)

11.62   B. Ferguson, X.C. Zhang: Materials for terahertz science and technology, Nat. Mater. **1**, 26–33 (2002)

11.63   K. Sakai (Ed.): *Teraherz Optoelectronics* (Springer, Berlin, Heidelberg 2005)

11.64   R. Huber, F. Tauser, A. Brodschelm, M. Bichler, G. Abstreiter, A. Leitenstorfer: How many-particle interactions develop after ultrafast excitation of an electron–hole plasma, Nature **414**, 286–289 (2001)

11.65   M. Ashida: Ultra-broadband terahertz wave detection using photoconductive antenna, Jpn. J. Appl. Phys. **47**, 8221–8225 (2008)

11.66   C. Kübler, R. Huber, S. Tübel, A. Leitenstorfer: Ultrabroadband detection of multi-terahertz field transients with GaSe electro-optic sensors: Approaching the near infrared, Appl. Phys. Lett. **85**, 3360–3362 (2004)

11.67   K. Kawase: Terahertz imaging for drug detection and large-scale integrated circuit inspection, Opt. Photon. News **15**, 34–39 (2004)

11.68   J.A. Buck: *Fundamentals of Optical Fibers* (Wiley, New York 1995), Chap. 3

11.69   T. Li (Ed.): *Optical Fiber Communications: Fiber Fabrication*, Vol. 1 (Academic, San Diego 1985)

11.70   TIA-455-78: Spectral Attenuation Cutback Measurement for Single Mode Optical Fibers (Electronic Industries Association, Washington 2002)

11.71   TIA/EIA-455-50: Light Launch Conditions for Long-Length, Graded-Index Optical Fiber Spectral Attenuation measurements, Procedure B (Electronic Industries Association, Washington 2001)

11.72   I.H. Maliston: Interspecimen comparison of the refractive index of fused silica, J. Opt. Soc. Am. **55**, 1205–1209 (1965)

11.73   M.J. Adams: *An Introduction to Optical Waveguides* (Wiley, New York 1981), Chap. 7

11.74   B.J. Ainslie, C.R. Day: A review of single-mode fibers with modified dispersion characteristics, J. Lightwave Technol. **4**, 967–979 (1986)

11.75   L.G. Cohen, C. Lin: Pulse delay measurements in the zero material dispersion wavelength region for optical fibers, Appl. Opt. **16**, 3136–3139 (1977)

11.76   B. Costa, D. Mazzoni, M. Puleo, E. Vezzoni: Phase shift technique for the measurement of chromatic dispersion in optical fibers using LEDs, IEEE J. Quantum Electron. **QE-18**, 1509–1515 (1982)

11.77   M. Takeda, N. Shibata, S. Seikai: Interferometic method for chromatic dispersion measurement in a single-mode optical fiber, IEEE J. Quantum Electron. **QE-17**, 404–407 (1981)

11.78   D. Milam, M.J. Weber: Measurement of nonlinear refractive-index coefficients using time-resolved interferometry: Application to optical materials for high-power neodymium lasers, J. Appl. Phys. **47**, 2497–2501 (1976)

11.79   A. Fellegara, M. Artiglia, S.B. Andreasen, A. Melloni, F.P. Espunes, M. Martinelli: COST 241 intercomparison of nonlinear refractive index measurements in dispersion shifted optical fibres at $\lambda = 1550$ nm, Electron. Lett. **33**, 1168–1170 (1997)

11.80   G.P. Agrawal: *Nonlinear Fiber Optics* (Academic, New York 1989)

11.81   M.E. Fermann, A. Galvanauskas, G. Sucha, D. Harter: Fiber-lasers for ultrafast optics, Appl. Phys. B **65**, 259–275 (1997)

11.82   L.E. Nelson, D.J. Jones, K. Tamura, H.A. Haus, E.P. Ippen: Ultrashort-pulse fiber ring lasers, Appl. Phys. B **65**, 277–294 (1997)

11.83   J.K. Ranka, R.S. Windeler, A.J. Stentz: Visible continuum generation in air–silica microstructure optical fibers with anormalous dispersion at 800 nm, Opt. Lett. **25**, 25–27 (2000)

11.84   R.H. Stolen: Nonlinearity in fiber transmission, Proc. IEEE **68**, 1232–1236 (1980)

11.85   D. Marcuse, A.R. Chraplyvy, R.W. Tkach: Effect of fiber on long distance transmission, IEEE J. Lightwave Technol. **9**, 121–128 (1991)

11.86   R.G. Smith: Optical power handling capacity of low loss optical fibers as determined by stimulated Raman and Brillouin scattering, Appl. Opt. **11**, 2489–2494 (1972)

11.87   Y. Namihara, M. Miyata, N. Tanahashi: Nonlinear coefficient measurements for dispersion shifted fibres using self-phase modulation method at 1.55 µm, Electron. Lett. **30**, 1171–1172 (1994)

11.88   A. Boskovic, S.V. Chernikov, J.R. Taylor, L. Gruner-Nielsen, O.A. Levring: Direct continuous-wave measurement of n_2 in various types of telecommunication fiber at 1.55 µm, Opt. Lett. **21**, 1966–1968 (1996)

11.89   R.H. Stolen, C. Lin: Self-phase-modulation in silica fibers, Phys. Rev. **17**, 1448–1454 (1978)

11.90   T. Kato, Y. Suetsugu, M. Takagi, E. Sasaoka, M. Nishimura: Measurement of the nonlinear refractive index in optical fiber by the cross-phase-modulation method with depolarized pump light, Opt. Lett. **20**, 988–990 (1995)

11.91 L. Prigent, J.P. Hamaide: Measurement of fiber nonlinear Kerr coefficient by four-wave mixing, IEEE Photon. Technol. Lett. **5**, 1092–1095 (1993)

11.92 K.O. Hill, Y. Fujii, D.C. Johnson, B.S. Kawasaki: Photosensitivity in optical fiber waveguides: Application to reflection filter fabrication, Appl. Phys. Lett. **32**, 647–649 (1978)

11.93 K.O. Hills, B. Malo, F. Bilodeau, D.C. Johnson: Photosensitivity in optical fibers, Annu. Rev. Mater. Sci. **23**, 125–157 (1993)

11.94 I. Bennion, J.A.R. Williams, L. Zhang, K. Sugden, N. Doran: Tutorial review, UV-written in-fibre Bragg gratings, Opt. Quantum Electron. **28**, 93–135 (1996)

11.95 M. Bass, E.W. Van Stryland: *Fiber Optics Handbook, Fiber, Devices and Systems for Optical Communications* (McGraw-Hill, New York 2002), Chap. 9

11.96 P.J. Lemaire, R.M. Adkins, V. Mizrahi, W.A. Reed: High pressure H_2 loading as a technique for achieving ultrahigh UV photosensitivity in GeO_2 doped optical fibers, Electron. Lett. **29**, 1191–1193 (1993)

11.97 F. Bilodeau, B. Malo, J. Albert, D.C. Johnson, K.O. Hill, Y. Hibino, M. Abe, M. Kawachi: Photosensitization of optical fiber and silica-on-silicon/silica waveguides, Opt. Lett. **18**, 953–955 (1993)

11.98 G. Meltz, W.W. Morey, W.H. Glenn: Formation of Bragg gratings in optical fibers by a transverse holographic method, Opt. Lett. **14**, 823–825 (1989)

11.99 K.O. Hill, B. Malo, F. Bilodeau, D.C. Johnson, J. Albert: Bragg gratings fabricated in monomode photosensitive optical fiber by UV exposure through a phase mask, Appl. Phys. Lett. **62**, 1035–1037 (1993)

11.100 K.O. Hill, B. Malo, K.A. Vineberg, F. Bilodeau, D.C. Johnson, I. Skinner: Efficient mode conversion in telecommunication fiber using externally written gratings, Electron. Lett. **26**, 1270–1272 (1990)

11.101 B. Malo, S. Theriault, D.C. Johnson, F. Bilodeau, J. Albert, K.O. Hill: Apodised in-fibre Bragg grating reflectors photoimprinted using a phase mask, Electron. Lett. **31**, 223–225 (1995)

11.102 K.O. Hill, G. Metz: Fiber Bragg grating technology fundamentals and overview, J. Lightwave Technol. **15**, 1263–1276 (1997)

11.103 A.M. Vengsarkar, P.J. Remaire, J.B. Judkins, V. Bhatia, T. Erdogan, J.E. Sipe: Long-period fiber gratings as a band-rejection filters, J. Lightwave Technol. **14**, 58–65 (1996)

11.104 A.M. Vengsarkar, J.R. Pedrazzani, J.B. Judkins, P.J. Lemaire, N.S. Bergano, C.R. Davidson: Long-period fiber-grating-based gain equalizers, Opt. Lett. **21**, 336–338 (1996)

11.105 E. Desurvire: *Erbium-Doped Fiber Amplifiers, Principles and Applications* (Wiley-Interscience, New York 1994) p. 238

11.106 M. Bass, E.W. Van Stryland: *Fiber Optics Handbook, Fiber, Devices, and Systems for Optical Communications* (McGraw-Hill, New York 2002), Chap. 15

11.107 S. Sudo: Outline of optical fiber amplifiers. In: *Optical Fiber Amplifiers: Materials, Devices, and Applications*, ed. by S. Sudo (Artech House, Boston 1997) pp. 81–83

11.108 W.J. Miniscalco: Erbium-doped glasses for fiber amplifiers at 1500 nm, IEEE J. Lightwave Technol. **9**, 234–250 (1991)

11.109 T.J. Whitley, R. Wyatt, D. Szebesta, S. Davey, J.R. Williams: Quarter-Watt output at 1.3 μm from a praseodymium-doped fluoride fiber amplifier pumped with a diode-pumped Nd:YLF laser, IEEE Photon. Technol. Lett. **5**, 399–401 (1993)

11.110 T.J. Whitley: A review of recent system demonstrations incorporating 1.3 μm praseodymium-doped fluoride fibre amplifiers, IEEE J. Lightwave Technol. **13**, 744–760 (1995)

11.111 P.C. Becker, N.A. Olsson, J.R. Simpson, A.A. Olsson: *Erbium-Doped Fiber Amplifiers, Fundamentals and Technology* (Academic, San Diego 1999) pp. 139–140

11.112 E. Desurvire: *Erbium doped Fiber Amplifiers, Principles and Applications* (Wiley-Interscience, New York 1994) pp. 339–340

11.113 H.A. Haus: The noise figure of amplifiers, IEEE Photon. Technol. Lett. **10**, 1602–1606 (1998)

11.114 I.N. Duling: All-fiber ring soliton laser mode locked with a non-linear mirror, Opt. Lett. **16**, 539–541 (1991)

11.115 M. Bass, E.W. Van Stryland: *Fiber Optics Handbook* (McGraw-Hill, New York 2002), Chap. 5

11.116 S.T. Davey, P.W. France: Rare-earth-doped fluorozirconate glass for fiber devices, Br. Telecom Technol. J. **7**, 58 (1989)

11.117 F. Roy, D. Bayart, A. Le Sauze, P. Baniel: Noise and gain band management of thulium doped fiber amplifier with dual-wavelength pumping schemes, Photon. Technol. Lett. **13**, 788–790 (2001)

11.118 T. Karamatsu, Y. Yano, T. Ono: Laser-diode pumping (1.4 and 1.56 μm) of gain-shifted thulium-doped fiber amplifier, Electron. Lett. **36**, 1607–1609 (2000)

11.119 R.M. Percival, D. Szebesta, C.P. Seltzer, S.D. Perrin, S.T. Davey, M. Louka: A 1.6 μm pumped 1.9 μm thulium-doped fluoride fiber laser and amplifier of very high efficiency, IEEE J. Quantum Electron. **QE-31**, 498–493 (1995)

11.120 S. Sudo: Progress in Optical Fiber Amplifiers. In: *Current Trends in Optical Amplifiers and their Applications*, ed. by P.T. Lee (World Scientific, Teaneck 1996) pp. 19–21

11.121 S. Namiki, Y. Emori: Ultra-broadband Raman amplifiers pumped and gain equalized by wavelength-division-multiplexed high-power diode, IEEE J. Sel. Quantum Electron. **7**, 3–16 (2001)

11.122 M.E. Fermann: Nonlinear polarization evolution in passively modelocked fiber laser. In: *Compact Ul-*

trafast Pulse Sources, ed. by I.N. Duling (Cambridge Univ. Press, Cambridge 1995)

11.123 M.E. Fermann, A. Galvanauskas, G. Sucha: *Ultrafast Lasers: Technology and Applications* (Marcel Dekker, New York 2003)

11.124 D.J. DiGiovanni, A.J. Stentz: Tapered fiber bundles for coupling light into and out of cladding–pumped fiber lasers, US Patent 5864644 (1999)

11.125 L. Goldberg, P. Koplow, D.A.V. Kliner: Highly efficient4-W Yb-doped fiber amplifier pumped by a broad-stripe laser diode, Opt. Lett. **24**, 673–675 (1999)

11.126 V.P. Gapontsev, I. Samartsev: Coupling arrangement between a multi-mode light source and an optical fiber through an intermediate optical fiber length, US Patent 5999673 (1999)

11.127 N.S. Platonov, V.P. Gapontsev, O. Shkurihin, I. Zaitsev: 400 W low-noise single-mode CW ytterbium fiber laser with an integrated fiber delivery, Conf. Lasers Electro-Opt. (Optical Society of America, Washington 2003), postdeadline paper CThPDB9

11.128 V. Dominic, S. MacCormack, R. Waarts, S. Sanders, S. Bicknese, R. Dohle, E. Wolak, P.S. Yeh, E. Zucker: 110 W fibre laser, Electron. Lett. **35**, 1158–1160 (1999)

11.129 J. Nilsson, J.K. Sahu, W.A. Clarkson, R. Selvas: High power fiber lasers: New developments, Proc. SPIE **4974**, 50–59 (2003)

11.130 S.F. Carter, M.W. Moore, D. Szebesta, D. Ransom, P. France: Low loss fluoride fibre by reduced pressure casting, Electron. Lett. **26**, 2115–2117 (1990)

11.131 R. Nubling, J.A. Harrington: Optical properties of single–crystal sapphire fibers, Appl. Opt. **36**, 5934–5940 (1997)

11.132 J. Nishii, S. Morimoto, I. Inagawa, R. Iizuka, T. Yamashita, T. Yamagishi: Recent advances and trends in chalcogenide glass fiber technology, A review, J. Non-Cryst. Solids **140**, 199–208 (1992)

11.133 V. Artjushenko, V. Ionov, K.J. Kalaidjian, A.P. Kryukov, E.F. Kuzin, A.A. Lerman, A.S. Prokhorov, E.V. Stepanov, K. Bakhshpour, K.B. Moran, W. Neuberger: Infrared fibers: Power delivery and medical applications, Proc. SPIE **2396**, 25–36 (1995)

11.134 Y. Matsuura, T. Abel, J.A. Harrington: Optical properties of small-bore hollow glass waveguides, Appl. Opt. **34**, 6842–6847 (1995)

11.135 E.W. Van Stryland, M. Bass: *Fiber Optics Handbook* (McGraw-Hill, New York 2002), Chap. 14

11.136 P.W. France, S.F. Carter, M.W. Moore, C.R. Day: Progress on fluoride fibres for optical communications, Br. Telecom Technol. J. **5**, 28–44 (1987)

11.137 S. Kobayashi, N. Shibata, S. Shibata, T. Izawa: Characteristics of optical fibers in infrared wavelength region, Electr. Commun. Lab. Rev. **26**, 453–467 (1978)

11.138 T. Abel, J. Hirsch, J.A. Harrington: Hollow glass waveguides for broadband infrared transmission, Opt. Lett. **19**, 1034–1036 (1994)

11.139 R.K. Nubling, J.A. Harrington: Hollow-waveguide delivery systems for high-power, industrial CO_2 lasers, Appl. Opt. **35**, 372–380 (1996)

11.140 J. Sanghera, I. Aggarwal: *Infrared Fiber Optics* (CRC, Boca Raton 1998)

11.141 A. Weinert: *Plastic Optical Fibers: Principle, Components, Installation* (VCH, Weinheim 1999)

11.142 Y. Watanabe, C. Tanaka: Current status of perfluorinated GI-POF and 2.5 Gbps data transmission over it, Proc. OFC, Los Angeles (2003) pp. 12–13

11.143 E. Yablonovitch: Photonic band-gap structures, J. Opt. Soc. Am. B **10**, 283–295 (1993)

11.144 T.A. Birks, R.J. Robert, P.S.J. Russell: Full 2-D photonic band gaps in silica/air structures, Electron. Lett. **31**, 1941–1943 (1995)

11.145 J.C. Knight, T.A. Birks, D.M. Adkin, P.S.J. Russel: Pure silica single mode fiber with hexagonal photonic crystal cladding, Proc. OFC, San Jose (1996), PD3

11.146 P. Russel: Photonic crystal fibers, Science **299**, 385–362 (2003)

11.147 T.A. Birks, J.C. Knight, P.S.J. Russell: Endlessly single-mode photonic crystal fibers, Opt. Lett. **22**, 961–963 (1977)

11.148 J.C. Knight, T.A. Birks, P.S.J. Russell, D.M. Atkin: All-silica single-mode optical fiber with photonic crystal cladding, Opt. Lett. **21**, 1547–1549 (1996)

11.149 J. Limpert, T. Schreiber, S. Nolte, H. Zellmer, T. Tunnermann, R. Iliew, F. Lederer, J. Broeng, G. Vienne, A. Petersson, C. Jakobsen: High-power air-clad large-mode-area photonic crystal fiber laser, Opt. Express **11**, 818–823 (2003)

11.150 J.C. Knight, J. Arriaga, T.A. Birks, A. Ortigosa-Blanch, W.J. Wadsworth, P.S.J. Russell: Anomalous dispersion in photonic crystal fiber, IEEE Photon. Technol. Lett. **12**, 807–809 (2000)

11.151 J.K. Ranka, R.S. Windeler, A.J. Stentz: Visible continuum generation in air-silica microstructure optical fibers with anormalous dispersion at 800 nm, Opt. Lett. **25**, 25–27 (2000)

11.152 T. Udem, R. Holzwarth, T.W. Hänsch: Optical frequency metrology, Nature **416**, 233–237 (2002)

11.153 B. Povazy, K. Bizheva, A. Unterhuber, B. Hermann, H. Sattmann, A.E. Fercher, W. Drexler, A. Apolonski, W.J. Wadsworth, J.C. Knight, P.S.J. Russel, M. Vetterlein, E. Scherzer: Submicrometer axial resolution optical coherence tomography, Opt. Lett. **27**, 1800–1802 (2002)

11.154 A. Ortigosa-Blanch, J.C. Knight, W.J. Wadsworth, J. Arriaga, B.J. Mangan, T.A. Birks, P.S.J. Russel: Highly birefrigent photonic crystal fibers, Opt. Lett. **25**, 1325–1327 (2000)

11.155 R.F. Cregan, B.J. Mangan, J.C. Knight, T.A. Birks, P.S.J. Russell, P.J. Roberts, D.C. Allan: Single-mode photonic bandgap guidance of light in air, Science **285**, 1537–1539 (1999)

11.156 B.J. Mangan, L. Farr, A. Langford, P.J. Roberts, D.P. Williams, F. Cony, M. Lawman, M. Ma-

son, S. Coupland, R. Flea, H. Sabert, T.A. Birks, J.C. Knight, P.S.J. Russel: Low loss (1.7 dB/km) hollow core photonic bandgap fiber, Proc. Opt. Fiber Commun. Conf., Vol. 2 (Optical Society of America, Los Angeles 2004) p. 3, (post deadline paper)

11.157 K. Nakayama: Ultra-low loss (0.151 dB/km) fiber and its impact on submarine transmission system, Proc. OFC (Anaheim 2002), FA10-1

11.158 J.D. Shephard, J. Jones, D. Hand, G. Bouwmans, J. Knight, P. Russell, B. Mangan: High energy nanosecond laser pulses delivered single-mode through hollow-core PBG fibers, Opt. Express **12**, 717–723 (2004)

11.159 G. Bouwmans, F. Luan, J. Knight, P.S.J. Russell, L. Farr, B. Mangan, H. Sabert: Properties of a hollow-core photonic bandgap fiber at 850 nm wavelength, Opt. Express **13**, 1613–1620 (2003)

11.160 B.T. Kolomiets: Chalcogenide alloy vitreous semiconductor physiochemical, optical, electrical, photoelectric and glass crystal transition properties, Phys. Status Solidi (b) **7**, 359–372 (1964)

11.161 J. Feinleib, J. deNeufville, S.R. Ovshinsky: Rapid reversible light-induced crystallization of amorphous semiconductors, Appl. Phys. Lett. **18**, 254–257 (1971)

11.162 A.W. Smith: Injection laser writing on chalcogenide films, Appl. Opt. **13**, 795–798 (1974)

11.163 N. Yamada, S. Ohara, K. Nishiuchi, M. Nagashima, M. Takenaga, S. Nakamura: Erasable optical disc using TeO_x thin film, Proc. 3rd Int. Display Res. Conf., Japan Display, Kobe, ed. by F.J. Kahn, T. Yoshida (Society for Information Display and Institute of Television Engineers of Japan, 1983) pp. 46–48

11.164 M. Chen, K.A. Rubin, V. Marrello, U.G. Gerber, V.B. Jipson: Reversibility and stability of tellurium alloys for optical data storage applications, Appl. Phys. Lett. **46**, 734–736 (1985)

11.165 M. Terao, T. Nishida, Y. Miyauchi, T. Nakao, T. Kaku, S. Horigome, M. Ojima, Y. Tsunoda, Y. Sugita, Y. Ohta: Sn–Te–Se phase change recording film for optical disks, Proc. SPIE **529**, 46 (1985)

11.166 N. Yamada, E. Ohno, K. Nishiuchi, N. Akahira, M. Takao: Rapid-phase transitions of $GeTe-Sb_2Te_3$ pseudobinary amorphous thin films for an optical disk memory, J. Appl. Phys. **69**, 2849–2856 (1991)

11.167 N. Yamada: Erasable phase-change optical materials, MRS Bulletin **21**(9), 48–50 (1996)

11.168 H. Iwasaki, Y. Ide, M. Harigaya, Y. Kageyama, I. Fujimura: Completely erasable phase change optical disk, Jpn. J. Appl. Phys. **31**(2), 461–465 (1992)

11.169 M. Horie, N. Nobukuni, K. Kiyono, T. Ohno: High-speed rewritable DVD up to 20 m/s with nucleation-free eutectic phase-change material of $Ge(Sb_{70}Te_{30})+Sb$, Proc. SPIE **4090**, 135–143 (2001)

11.170 H. Tashiro, M. Harigaya, K. Ito, M. Shinkai, K. Tani, N. Yiwata, A. Watada, N. Toyoshima, K. Makita,

A. Kitano, K. Kato: Phase-change material for high-speed rewritable media, Proc. E*PCOS2003, Lugano, ed. by I. Satoh (2003), (online publication http://www.epcos.org/pdf_2003/Tashiro.pdf)

11.171 H.E. Kissinger: Variation of peak temperature with heating rate in different thermal analysis, J. Res. Nat. Bur. Stand. **57**, 217–221 (1956)

11.172 H.E. Kissinger: Reaction kinetics in differential thermal analysis, Anal. Chem. **29**(11), 1702–1706 (1957)

11.173 H. Kubota: *Hadou-kougaku* (Iwanami, Tokyo 1971), (in Japanese)

11.174 K. Nishiuchi, N. Yamada, N. Akahira, M. Takenaga: Laser diode beam exposure instrument for rapid quenching of thin-film materials, Rev. Sci. Instrum. **63**(6), 3425–3430 (1992)

11.175 I. Satoh, N. Yamada: DVD-RAM for all audio/video, PC, and network applications, Proc. SPIE **4085**, 283–290 (2001)

11.176 H.M. Rietveld: A profile refinement method for nuclear and magnetic structures, J. Appl. Crystallogr. **2**, 65–71 (1969)

11.177 H.J. Williams, R.C. Sherwood, F.G. Foster, E.M. Kelley: Magnetic writing on thin films of MnBi, J. Appl. Phys. **28**(10), 1181–1184 (1957)

11.178 L. Mayer: Curie-point writing on magnetic films, J. Appl. Phys. **29**(6), 1003 (1958)

11.179 J.T. Chang, J.F. Dillon Jr., U.F. Gianola: Magneto-optical variable memory based upon the properties of a transparent ferrimagnetic garnet at its compensation temperature, J. Appl. Phys. **36**, 1110–1111 (1965)

11.180 P. Chaudhari, J.J. Cuomo, R.J. Gambino: Amorphous metallic films for magneto-optic, Appl. Phys. Lett. **22**, 337–339 (1973)

11.181 W.P. Van Drent, T. Suzuki: A new ultra-violet magneto-optical spectroscopic instrument and its application to Co-based multilayers and thin films, IEEE Trans. Magn. **33**(5), 3223–3225 (1997)

11.182 J. Saito, M. Sato, H. Matsumoto, H. Akasaka: Direct overwrite by light power modulation on magneto-optical multi-layered media, Jpn. J. Appl. Phys. **26**(Suppl. 4), 155–159 (1987)

11.183 T. Fukami, Y. Kawano, T. Tokunaga, Y. Nakaki, K. Tsutsumi: Direct overwrite technology using exchange-coupled multilayer, J. Magn. Soc. Jpn. **15**(Suppl. 1), 293–298 (1987)

11.184 M. Kaneko, K. Aratani, M. Ohta: Multilayered magneto-optical disks for magnetically induced super resolution, Jpn. J. Appl. Phys. Ser. **6**, 203–210 (1991)

11.185 K. Aratani, A. Fukumoto, M. Ohta, M. Kaneko, K. Watanabe: Magnetically induced super resolution in a novel magneto-optical disk, Proc. SPIE **1499**, 209–215 (1991)

11.186 M. Ohta, A. Fukumoto, M. Kaneko: Read out mechanism of magnetically induced super resolution, J. Magn. Soc. Jpn. **15**(Suppl. 1), 319–322 (1991)

Part C | 11

11.187 A. Takahashi, M. Kaneko, H. Watanabe, Y. Uchihara, M. Moribe: 5 Gbit/inch^2 MO technology, J. Magn. Soc. Jpn. **22**(Suppl. 2), 67–70 (1998)

11.188 K. Shono: 3.5-inch MO disk using double-mask MSR Media, J. Magn. Soc. Jpn. **23**, 177–180 (1999)

11.189 M. Birukawa, K. Uchida, N. Miyatake: Reading a 0.2 μm mark using the MSR method, J. Magn. Soc. Jpn. **20**(Suppl. S1), 103–108 (1996)

11.190 E. Betzig, J.K. Trautman, R. Wolfe, E.M. Gyorgy, P.L. Finn, M.H. Kryder, C.-H. Chang: Near-field magneto-optics and high density data storage, Appl. Phys. Lett. **61**, 142–144 (1992)

11.191 V. Kottler, N. Essaidi, N. Ronarch, C. Chappert, Y. Chen: Dichroic imaging of magnetic domains with a scanning near-field optical microscope, J. Magn. Magn. Mater. **165**(1–3), 398–400 (1997)

11.192 S. Sato, T. Ishibashi, T. Yoshida, J. Yarnarnoto, A. Iijirna, Y. Mitsuoka, K. Nakajima: Observation of recorded marks of MO disk by scanning near-field magneto-optical microscope, J. Magn. Soc. Jpn. **23**(Suppl. 1), 201–204 (1999)

11.193 Y. Martin, D. Rugar, H.K. Wickramasinghe: High-resolution magnetic imaging of domains in TbFe by force microscopy, Appl. Phys. Lett. **52**, 244–246 (1988)

11.194 P. Grutter, D. Rugar, T.R. Alberechit, H.J. Mamin: Magnetic force microscopy-recent advantages and applications to magneto-optic recording, J. Magn. Soc. Jpn. **15**(Suppl. S1), 243–244 (1991)

11.195 H.W. van Kesteren, A.J. den Boef, W.B. Zeper, J.H.M. Spruit, B.A.J. Jacobs, P.F. Carcia: Scanning magnetic force microscopy on Co/Pt magneto-optical disks, J. Magn. Soc. Jpn. **15**(Suppl. S1), 247–250 (1991)

11.196 P. Giljer, J.M. Sivertsen, J.H. Judy, C.S. Bhatia, M.F. Doerner, T. Suzuki: Magnetic recording measurements of high coercivity longitudinal media using magnetic force microscopy (MFM), J. Appl. Phys. **79**(8), 5327–5329 (1996)

11.197 M. Birukawa, Y. Hino, K. Nishikiori, K. Uchida, T. Shiratori, T. Hiroki, Y. Miyaoka, Y. Hozumi: Two-inch-diameter magneto-optical disk system with 3 GB capacity and 24 Mbps data transfer rate using a red laser, Trans. Magn. Soc. Jpn. **2**, 273–278 (2002)

11.198 H. Awano, S. Ohnuki, H. Shirai, N. Ohta, A. Yamaguchi, S. Sumi, K. Torazawa: Magnetic domain expansion readout for amplification of an ultra high density magneto-optical recording signal, Appl. Phys. Lett. **69**, 4257–4259 (1996)

11.199 T. Shiratori, E. Fujii, Y. Miyaoka, Y. Hozumi: High-density magneto-optical recording with domain displacement detection, J. Magn. Soc. Jpn. **22**(Suppl. 2), 47–50 (1998)

11.200 T. Araki: Optical distance meter developed using a short pulse width laser diode, a fast avalanche photodiode, Rev. Sci. Instrum. **66**, 43–47 (1995)

11.201 T. Araki, S. Yokuyama, N. Suzuki: Simple optical distancemeter using an intermode-beat modulation of He–Ne laser and an electrical heterodyne technique, Rev. Sci. Instrum. **65**, 1883–1888 (1994)

11.202 M. Born, E. Wolf: *Principle of Optics*, 7th edn. (Cambridge Univ. Press, Cambridge 1997)

11.203 S. Alaruri, A. Brewington, M. Thomas, J. Miller: High-temperature remote thermometry using laser induced fluorescence decay lifetime measurements of Y_2O_3:Eu and YAG:Tb, IEEE Trans. Instrum. Meas. **42**, 735–739 (1993)

11.204 A.C. Eckbreth, G.M. Dobbs, J.H. Stufflebeam, P.A. Tellex: CARS temperature and species measurements in augmented jet engine exhausts, Appl. Opt. **23**, 1328–1339 (1984)

11.205 M. Hashimoto, T. Araki, S. Kawata: Molecular vibration imaging in the fingerprint region by use of coherent anti-Stokes Raman scattering microscopy with a collinear configuration, Opt. Lett. **25**, 1768–1770 (2000)

11.206 N. Brand, C. Gizoni: Moiré contourography and infrared thermography; Changes resulting from chiropractic adjustments, J. Manip. Physiol. Ther. **5**, 113–116 (1982)

11.207 D. Huang, E.A. Swanson, C.P. Lin, J.S. Schuman, W.G. Stinson, W. Chang, M.R. Hee, T. Flotte, K. Gregory, C.A. Puliafito, J.G. Fujimoto: Optical coherence tomography, Science **254**, 1178–1181 (1991)

11.208 Y. Aizu, T. Asakura: Coherent optical techniques for diagnostics of retinal blood flow, J. Biomed. Opt. **4**, 61–75 (1999)

11.209 N. Konishi, H. Fujii: Real-time visualization of retinal microcirculation by laser flowgraphy, Opt. Eng. **34**, 65–68 (1995)

11.210 J.G. Webster: *Design of Pulse Oximeter* (IOP, Bristol 1997)

11.211 K. Matsushima, K. Aoki, Y. Yamada, N. Kakuta: Fundamental study of reflection pulse oximetry, Opt. Rev. **10**, 482–487 (2003)

11.212 H. Koizumi, Y. Yamashita, A. Maki, T. Yamamoto, Y. Itoh, H. Itagaki, R. Kennan: Higher-order brain function analysis by trans-cranial dynamic near-infrared spectroscopy imaging, J. Biomed. Opt. **4**, 403–413 (1999)

11.213 M. Okuyama, N. Tsumura, Y. Miyake: Evaluating a multi-spectral imaging system for mapping pigments in human skin, Opt. Rev. **10**, 580–584 (2003)

11.214 S.A. Pape, C.A. Skouras, P.O. Byrne: An audit of the use of laser Doppler imaging (LDI) in the assessment of burns of intermediate depth, Burns **27**, 233–239 (2001)

11.215 S. Roth, I. Freund: Second harmonic generation in collagen, J. Chem. Phys. **70**, 1637–1643 (1979)

11.216 T. Yasui, Y. Tohno, T. Araki: Characterization of collagen orientation in human dermis by two-

dimensional second-harmonic-generation polarimetry, J. Biomed. Opt. **9**, 259–264 (2004)

11.217 R.M. Woodward, B.E. Cole, V.P. Wallace, R.J. Pye, D.D. Arnone, E.H. Linfield, M. Pepper: Terahertz pulse imaging in reflection geometry of human skin cancer and skin tissue, Phys. Med. Biol. **47**, 3853–3863 (2002)

11.218 J.S. Nelson: Special section on optics of human skin, J. Biomed. Opt. **9**, 247–420 (2004)

11.219 C. Chou, C. Han, W. Kuo, Y. Huang, C. Feng, J. Shyu: Noninvasive glucose monitoring in vivo with an optical heterodyne polarimeter, Appl. Opt. **37**, 3553–3557 (1998)

Part C | 11